RIMS-1770

Covariant Lyapunov Analysis of Navier-Stokes Turbulence

By

Masanobu INUBUSHI

January 2013

京都大学　数理解析研究所

RESEARCH INSTITUTE FOR MATHEMATICAL SCIENCES

KYOTO UNIVERSITY, Kyoto, Japan

Covariant Lyapunov Analysis of Navier-Stokes Turbulence

Masanobu Inubushi

Research Institute for Mathematical Sciences,
Kyoto University

—**Abstract**—

Turbulence is a 'disordered' state of fluid motion but shows robust and universal statistical properties including Kolmogorov -5/3 law and Prandtl logarithmic law, which we can observe in laboratory experiments, numerical experiments, and observations. It is important for a wide range of sciences and engineering to understand mechanisms of turbulence which produce such robust statistical properties. However, at present, our understanding is far from complete.

Turbulence can be interpreted as a chaotic dynamical system and this point of view is expected to provide a broader perspective to understand turbulence. In this thesis, we focus our attention on an orbital instability which is one of the important properties of chaos. Particularly, we employ *covariant Lyapunov analysis* recently developed by Ginelli *et al.* (2007), which gives Lyapunov vectors associated with Lyapunov exponents.

First of all, we study the orbital instability of chaotic Kolmogorov flows. Kolmogorov flow is a fluid flow on a two-dimensional torus governed by the incompressible Navier-Stokes equation and its bifurcation and stability have been under intense study (Okamoto, 1998). We study relations between *hyperbolic* property and physical property of the chaotic Kolmogorov flow. Hyperbolicity is one of the fundamental properties of dynamical systems related to the orbital instability. Recently, hyperbolicity of the chaotic Kolmogorov flow was studied by employing the covariant Lyapunov analysis, where the hyperbolic-nonhyperbolic transition was observed as the Reynolds number is increased (Inubushi *et al.*, 2012). Here, our interest lies in relations between the hyperbolic properties and physical properties of fluid motions. We study correlation decay of vorticity at several Reynolds numbers across the hyperbolic-nonhyperbolic transition point. We find that an oscillation in time-correlation function vanishes at the transition point. Furthermore, examining the energy dissipation rate and the angle between the stable and unstable manifolds θ, we show that the angle θ tends to be small when the energy dissipation rate is large in a statistical sense.

Next, we study the orbital instability of Couette turbulence. Couette turbulence is fluid turbulence between moving walls governed by the three-dimensional incompressible Navier-Stokes equation, often being studied with interests in the transition to turbulence and coherent structures in turbulence. Particularly we examine regeneration cycles which are important phenomenon observed in a wide variety of wall-turbulence including the Couette turbulence. The regeneration cycle is consisting of breakdown (in the first half period of the cycle) and reformation (in the last half period of the cy-

cle) of *streaks* which are well-known coherent structures. Here, a goal of this study is to characterize the regeneration cycle with the orbital instability by employing the covariant Lyapunov analysis. Firstly, we present the Lyapunov spectrum of the Couette turbulence, and we discuss the dimension of unstable manifold, the dimension of the attractor, and the Kolmogorov-Sinai entropy. To see the orbital instability of the regeneration cycle in more detail, we study the local Lyapunov exponents and the associated Lyapunov modes. With these quantities, we find that (1) at the breakdown of the streaks, the Lyapunov modes indicate a *sinuous* instability which makes the streaks meander, (2) when the streamwise vorticity is highly localized, the local Lyapunov exponents appear to attain their maxima in the regeneration cycle, and (3) the local Lyapunov exponents decrease rapidly and become negative after the localization of the streamwise vorticity. These results suggest that the 'most unstable' instability during the regeneration cycle is the instability associated with the strong localization of the streamwise vorticity rather than the sinuous instability. Also, instabilities are found only in a very early stage of the cycle and after that there are no exponential instability at all. Finally, we reconsider the regeneration cycle from the viewpoint of the orbital instability. There, we argue the physical mechanisms of the streak meandering (breakdown) and the localization of the streamwise vorticity, which can be characterized by the Lyapunov modes. Then, examining the evolution equation of the modal energy, we discuss the mechanism of the streak reformation which closes the cycle. We find that the streaks are reformed by interactions with mean flows and furthermore the energy is injected into a 'streak mode' from the mean flows almost *constantly* throughout the regeneration cycle. There, a natural question arises : what controls the development of the streaks (i.e. the regeneration cycle)? Finding an answer to the question, we study the energy flows in the system during the regeneration cycle in detail and detect an interaction between the streak mode and a 'meandering mode' that controls the regeneration cycle.

Contents

1 Introduction **1**

2 Relations between hyperbolic properties and physical properties of chaotic Kolmogorov flow **11**

2.1 Introduciton 11
2.2 Kolmogorov flow system and numerical method 12
2.3 Chaotic behavior of Kolmogorov flow 14
2.4 Covariant Lyapunov analysis of chaotic Kolmogorov flow . . . 16
2.5 Relations between hyperbolic properties and physical properties of chaotic Kolmogorov flow 20
2.5.1 Hyperbolicity and correlation fuction 20
2.5.2 Angle between stable and unstable manifolds and enstrophy 24
2.6 Discussions and Conclutions 25

3 Orbital instability of the regeneration cycle in minimal Couette turbulence **27**

3.1 Introduciton 27
3.2 Couette flow system and numerical method 31
3.2.1 Problem setting 31
3.2.2 Equation of motion 31
3.2.3 Numerical method 34
3.3 Turbulent behavior of minimal Couette flow 36
3.4 Orbital instability of the regeneration cycle in minimal Couette turbulence 39
3.5 Regeneration cycle from a viewpoint of orbital instability . . . 47
3.5.1 Phase (i); How do the streaks mender and the streamwise vortices appear? 47
3.5.2 Phase (ii); What regenerates the streaks? 50

3.5.3 Energy flows in the regeneration cycle; Which interaction does control the cycle? 54
3.6 Discussions and Conclusions 57

4 Conclusions and future issues **64**

A Appendix : Kolmogorov flow problem **68**
A.1 Pomeau-Manneville scenario in chaotic Kolmogorov flow . . . 68

B Appendix : Couette flow problem **71**
B.1 Formulation of Couette flow problem 71
B.1.1 Decomposition of velocity field and pressure field . . . 71
B.1.2 Equations of mean flow and fluctuating flow 73
B.1.3 Mean pressure gradient and volume flux 74
B.1.4 Boundary conditions 76
B.1.5 Derivation of horizontal mean flow equation 78
B.1.6 Derivation of momentum equation 80
B.2 Supplemental data 80
B.3 Description of the stage I in the phase (i) 86
B.4 Energy cascade in regeneration cycle 86
B.5 Derivation of evolution equation of modal energy 91
B.5.1 Derivation 91
B.5.2 Approximation of mean flow interaction term 96
B.5.3 Evolution equation of streak modal energy 96
B.6 Physical interpretation of streak reformation 99
B.6.1 Relation to lift-up mechanism 101
B.7 Derivation of evolution equation of modal enstrophy 102

Chapter 1

Introduction

Turbulence as a chaotic dynamical system.— Is dynamical system theory useful to understand turbulence? Turbulence is a 'disordered' state of fluid motion but shows robust and universal statistical properties including Kolmogorov -5/3 law in energy spectra of isotropic homogeneous turbulence and the Prandtl logarithmic law in mean velocity profiles of wall turbulence. We can observe such statistical properties in laboratory experiments, numerical experiments, and observations. These properties appear to be independent of the details of the system such as the way of excitation of turbulence and the boundary condition [1, 2]. It is important to understand turbulence mechanisms of producing such robust statistical properties for a wide range of sciences and engineering field. However, at present, our understanding is far from complete.

Dynamical system theory gives general concepts to study asymptotic states of a dynamical system, and gives tools to quantify the degree of 'disorder' of the states [3, 4]. From this point of view, the theory is expected to provide a broader perspective to understand turbulence, where we consider turbulence as a state point on a chaotic attractor in a phase space and gain new insights into turbulence by using such concepts and tools as bifurcations, periodic orbits, Lyapunov exponents and so on [5]. At the same time, understanding of the turbulence at this viewpoint may provide an important bridge between fluid system and high-dimensional dynamical systems in other fields.

One of the pioneer works on turbulence from a mathematical standpoint was done by Ruelle and Takens [6]. They considered definition of turbulence by discussing bifurcations of a (quasi-)periodic orbit and showed[1]that

[1]See Proposition (9.2) in [6].

a chaotic attractor appears by adding an arbitrary small perturbation to a quasi-periodic system[2]. Then, they proposed an idea that turbulence can be described in terms of a chaotic attractor rather than a quasi-periodic attractor with a large number of (rationally independent) frequencies as proposed by Landau [10][3]. This idea has been verified both experimentally and numerically in many studies. For instance, Gollub and Swinney [12] examined bifurcations in a rotating fluid in detail by employing power spectra, and demonstrated that the onset of turbulence is consistent not with the Landau picture but with Ruelle and Takens picture. Nowadays, most of the researchers have reached a consensus, following Ruelle and Takens idea, and there are many studies on turbulence considering it as a chaotic attractor[4].

Chaos is often characterized by the following concepts: *denseness of unstable periodic orbits* (*UPOs*) and *orbital instability* (cf. Devaney's definition of chaos[5]). Considering turbulence as chaos, invariant solutions including UPOs and orbital instability of the Navier-Stoles equation are important, and they have been studied numerically with an increase in computing power.

Invariant solutions within turbulence.— A number of the invariant solutions of the Navier-Stoles equation, numerically discovered recently, such as steady solutions, traveling wave solutions, and periodic solutions, are useful for understanding bifurcations of solutions, global structures of the phase space, and statistical properties of turbulence. Okamoto [17] studied bifurcations of *Kolmogorov flow* (see chapter 5 in [18] and chapter 2 in this thesis) and considered singular-limit flows in association with turbulence. Schneider

[2]In addition to this scenario (*Ruelle-Takens scenario*), we now know that there are some scenarios leading to chaotic attractor (route to chaos) : *Feigenbaum scenario* through period doubling and *Pomeau-Manneville scenario* through intermittency. See Eckmann [7] and Ott [8] for details. Inubushi *et al.* [9] studied Kolmogorov flow and found that chaotic fluid motion appears with Pomeau-Manneville scenario, in particular *Type-I intermittency* (see appendix A.1).

[3]See [11] for a description of view of turbulence at that time.

[4]In this thesis, we refer to *fluid* turbulence as 'turbulence', although sometimes the term 'turbulence' is used to describe disordered state found in general dynamical systems, including coupled map lattices, Kuramoto-Sivashinsky equation, complex Ginzburg-Landau equation, and so on [13].

[5]Roughly speaking, dynamical system f on an invariant set V is called to be *chaotic in Devaney's sense* if (1) f is *transitive*, (2) periodic points of f are dense in V, and (3) f has sensitive dependence on initial condition (see p.50 in [14]). However, now it is known that these conditions are not isolated, i.e. the condition (3) is followed by the conditions (1) and (2) [15]. Here we refer to the condition (3) as orbital instability. See §2.3 in Oono [16] for the definition of chaos from an interesting perspective.

et al. [19] found spatially localized solutions in *Couette flow* (see chapter 3) and argued a 'snakes-and-ladders' structure in their bifurcation diagram. On global structures in the phase space, invariant solutions play important roles in understanding of transition to shear turbulence, where a stable manifold of an invariant solution ('lower branch solution' or a 'gentle' UPO) is considered as a separatrix between basin of attraction of laminar flow and that of turbulent flow (see Itano and Toh [21], Waleffe [20], and Kawahara [22]). Halcrow *et al.* [23] showed several heteroclinic connections between these invariant solutions and discussed changes of coherent structures along the heteroclinic connections. In a relation with statistical properties of turbulence, a concept and a method of a cycle expansion are significant, by which we can calculate statistical quantities of turbulence in principle if the attractor of the turbulence is *hyperbolic* (see chapter 2) and we have some knowledge of the attractor (e.g. Floquet exponents of UPOs embedded in the attractor. see Cvitanovic [24]). Although the cycle expansion provides the statistical quantities by an *infinite* weighted sum of information of UPOs, Kawahara and Kida [25] found that statistical quantities such as a mean velocity profile and root mean square velocity profiles can be well approximated by a *single* UPO with low period embedded in Couette turbulence[6]. van Veen and Kawahara [26] recently computed homoclinic orbit to a time-periodic edge state (the gentle UPO) in Couette turbulence. They showed that the homoclinic orbit is related to *bursting events* in both spatiotemporal and statistical senses. Kato and Yamada [27] found a UPO in a shell model[7] of three-dimensional turbulence (GOY model[8]), which reproduces not only the Kolmogorov -5/3 law but also interimttency observed in turbulence, and suggested that averaged properties on the attractor can be described by the UPO as far as lower-order quantities are concerned. These findings on the invariant solutions make us realize fundamental questions and offer intriguing hints for understanding of turbulence.

Orbital instability.— In contrast to invariant solutions of the Navier-Stokes equation, which is actively investigated as seen above and reviewed by Kawahara [29], chaotic properties of the Navier-Stokes turbulence itself (e.g.

[6]Why can a single UPO with low period give an good approximation to the statistical properties of the turbulence? Saiki and Yamada [28] argued this fundamental and intriguing question by studying the statistical properties of more than 1000 UPOs and those of chaotic orbits in low-dimensional dynamical systems.

[7]They referred to this UPO as 'intermittency solution' [27].

[8]Gledzer-Ohkitani-Yamada model.

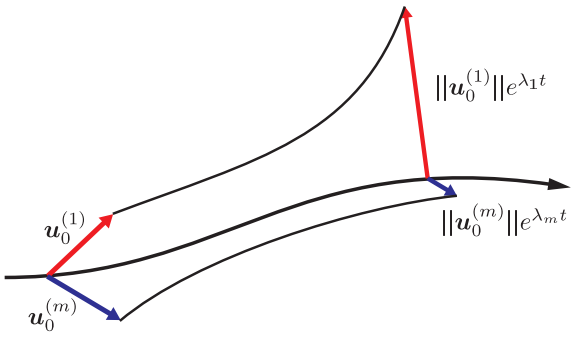

Fig. 1.1: Illustration of an orbit in a phase space. Red ($\boldsymbol{u}_0^{(1)}$) and blue ($\boldsymbol{u}_0^{(m)}$) arrows denote Lyapunov vectors associated with the Lyapunov exponents $\lambda_1(>0)$ and $\lambda_m(<0)$ respectively. $\boldsymbol{u}_0^{(1)}$ indicates unstable direction and $\boldsymbol{u}_0^{(m)}$ indicates stable direction along the orbit.

the properties of the orbital instability) appear to be attracting less interest in spite of their importance. One of the fundamental quantities characterizing the orbital instability is *Lyapunov* (or *characteristic*) *exponents* and their associated vectors (*Lyapunov vectors*). Considering a dynamical system defined by a map $\boldsymbol{f} : \mathbb{R}^m \to \mathbb{R}^m$ (equipped with some norm $||\cdot||$), we write time evolution of a state point in a phase space $\boldsymbol{x}_n \in \mathbb{R}^m$ as $\boldsymbol{x}_{n+1} = \boldsymbol{f}(\boldsymbol{x}_n)$. An infinitesimal perturbation vectors (tangent vectors) $\boldsymbol{u}_n^{(j)}$ $(j = 1, 2, \cdots, m)$ added to the state point $\boldsymbol{x}_n$ evolves, obeying the linearized equation:

$$\boldsymbol{u}_n^{(j)} = D\boldsymbol{f}_{\boldsymbol{x}_{n-1}} \boldsymbol{u}_{n-1}^{(j)}, \tag{1.1}$$

where $D\boldsymbol{f}_{\boldsymbol{x}_n}$ is a $m \times m$ Jacobian matrix. By using the chain rule of differentiation, we write

$$\boldsymbol{u}_n^{(j)} = D\boldsymbol{f}_{\boldsymbol{x}_{n-1}} \boldsymbol{u}_{n-1}^{(j)} = D\boldsymbol{f}_{\boldsymbol{x}_{n-1}}\, D\boldsymbol{f}_{\boldsymbol{x}_{n-2}} \cdots D\boldsymbol{f}_{\boldsymbol{x}_0} \boldsymbol{u}_0^{(j)} = D\boldsymbol{f}^n \boldsymbol{u}_0^{(j)}. \tag{1.2}$$

where $\boldsymbol{u}_0^{(j)}$ denotes an initial perturbation vector at an initial point $\boldsymbol{x}_0$. Then j-th Lyapunov exponent λ_j $(\lambda_1 \geq \lambda_2 \geq \cdots \geq \lambda_m)$ is defined as

$$\pm\lambda_j = \lim_{n \to \pm\infty} \frac{1}{|n|} \ln ||D\boldsymbol{f}^n \boldsymbol{u}_0^{(j)}||, \tag{1.3}$$

and the associated j-th Lyapunov vector at $\boldsymbol{x}_n$ is defined as $\boldsymbol{u}_n^{(j)}$. The set of Lyapunov exponents $\{\lambda_1, \lambda_2, \cdots, \lambda_m\}$ are referred to as Lyapunov spectrum.

In physical systems, such as a system describing turbulence, the Lyapunov exponents are considered to be independent of the choice of the initial point[9] $\boldsymbol{x}_0$. The Lyapunov exponent λ_j quantifies an exponential growth (or decay) rate of the norm of the perturbation added to the orbit, and correspondingly, the Lyapunov vector points to the direction of the perturbation vector (see Fig.1.1). Once we obtain the Lyapunov exponents λ_j $(j = 1, 2, \cdots, m)$, we can calculate also attractor dimension D_L (*Lyapunov dimension*) through Kaplan-Yorke formula : $D_L = K + \frac{1}{|\lambda_{K+1}|}\sum_{j=1}^{K}\lambda_j$ where K is the largest integer such that $\sum_{j=1}^{K}\lambda_j \geq 0$ and *Kolmogorov-Sinai* (or *metric*) *entropy* h_{KS} through Pesin identity : $h_{KS} = \sum_{\lambda_j>0}\lambda_j$ [5, 8]. To Study the instability of the dynamics in more detail, *local* (or *finite-time*) Lyapunov exponents are sometimes useful, which is defined as $\tilde{\lambda}_j(k,s) = \frac{1}{|k|}\ln||D\boldsymbol{f}^k\boldsymbol{u}_s^{(j)}||$. The local Lyapunov exponents $\tilde{\lambda}_j(k,s)$ depend on state point $\boldsymbol{x}_s$ and 'local mean time' k, which captures local orbital instabilities (see chapter 3). A numerical algorithm to compute Lyapunov exponents was first proposed by Shimada and Nagashima [30], who employed Gram-Schmidt orthogonalization of the tangent vectors. The orthogonalized tangent vectors obtained by the algorithm are referred to as *Gram-Schmidt vectors*. Note that the Gram-Schmidt vectors differ from Lyapunov vectors in general except the Lyapunov vector associated with the largest Lyapunov exponent λ_1.

Characterization of turbulene with orbital instability.— Using this algorithm for GOY model, Yamada and Ohkitani [32] obtained an asymptotic scaling law of the Lyapunov spectrum by using the Kolmogorov scaling theory. Karimi and Paul [33] characterized Rayleigh-Bénard convection with the Lyapunov vector associated with the largest Lyapunov exponent. They demonstrated statistically that a transition from 'boundary-dominated' dynamics to 'bulk-dominated' dynamics occurs when the system size is increased. Keefe *et al.* [34] calculated the Lyapunov spectrum of turbulent Poiseuille flow at Reynolds number $Re = 3200$ and found that the dimension of the attractor is 'dauntingly high', estimating the attractor dimension $D_L \simeq 780$ by using Lyapunov spectra. Recently, Nikitin [35] studied the

[9]Given some ergodic invariant measure ρ, the limit (1.3) exists for ρ-almost all $\boldsymbol{x}_0$ in a great generality (multiplicative ergodic theorem). See §9 in Ruelle [5] for more precise statements. Recently, Ott and Yorke [31] constructed two dynamical systems on $\mathbb{R}^2$ and showed that in these dynamical systems the Lyapunov exponent does not exist when we choose $\boldsymbol{x}_0$ in the basin that is not on the attractor. However, as mentioned in their paper, the flows defined by these dynamical systems are not generic in the space of smooth flows on $\mathbb{R}^2$ and far from physical systems.

largest Lyapunov exponent λ_1 of turbulent flows in a circular tube and in a plane channel over a range of Reynolds number $4000 \leq Re \leq 10700$ ($140 \leq Re_\tau \leq 320$) and showed that the largest Lyapunov exponent normalized by the 'wall time scale'[10] appears to be a constant value independent of the Reynolds number and the type of the wall turbulence. While these findings on the statistical quantities are important for understanding of the chaotic properties of the turbulence, it is also expected to use the Lyapunov analysis to elucidate the dynamics of turbulence (e.g. *regeneration cycle* of wall turbulence. See chapter 3). However it remains out of reach.

Covariant Lyapunov analysis.— As well as Lyapunov exponents, Lyapunov vectors may possess essential information of turbulent dynamics since they point to unstable directions of an orbit which indicate instability mechanisms to generate the turbulence. Although the conventional Lyapunov analysis employing numerical algorithms based on the method of the Shimada and Nagashima [30] gives the proper Lyapunov exponents, it only gives the Gram-Schmidt vectors instead of the Lyapunov vectors. It is difficult to find the physical meaning of the Gram-Schmidt vectors, since these vectors (i) depend on a definition of an inner product and (ii) are different from those in the backward time evolution (i.e. they are not invariant under time reversal). Both of these properties (i) and (ii) are not consistent with the definition of the Lyapunov vectors. On the other hand, in a finite dimensional smooth dynamical system, the Lyapunov vectors are the tangent vectors which do not depend on the definition of the inner product and give the same Lyapunov exponents except for their signs in the forward or backward time evolution. The Lyapunov vectors are bases of the local stable and unstable tangent spaces according to the signs of the Lyapunov exponents. Recently Ginelli *et al.* [36] proposed an algorithm, which is called *covariant* Lyapunov analysis, to obtain the Lyapunov vectors. The covariant Lyapunov analysis employs the conventional Lyapunov analysis as a first part of the algorithm, where the Gram-Schmidt vectors are computed in the forward time evolution. We then compute the tangent space dynamics confined to suitable subspaces in backward time evolution by using the stored Gram-Schmidt vectors. In the backward time evolution, the vectors in the subspaces converge generically to the Lyapunov vectors after sufficiently long time. Besides the covariant Lyapunov analysis, Wolfe et al. [37] proposed another computational method to calculate the Lyapunov vectors, what is called *characteristic* Lyapunov

[10]The time scale t_τ which is determined by the near-wall physics (i.e. defined by the 'wall friction' velocity u_τ and length l_τ as $t_\tau = l_\tau/u_\tau$). See chapter 3 for more details.

vectors[11]. These vectors, which have been applied to some chaotic systems such as coupled-map lattices [38], are also independent of the inner product and covariant under the tangent space dynamics (for the detailed comparison between these methods, see Kuptsov et al. [39]).

Thanks for the development of these numerical algorithms, the Lyapunov vectors have been used to study both conservative and dissipative dynamical systems. Yang and Radons [40] calculated the Lyapunov vectors of coupled maps lattice. They examined hydrodynamic Lyapunov modes (HLMs)[12] , what they call, in relation to non-equilibrium statistical mechanics, which supports their hypothesis : a certain *hyperbolic* property[13] is crucial for observing the HLMs. Employing the covariant Lyapunov vectors, Yang *et al.* [42] found an approach to study inertial manifolds which are finite-dimensional manifolds attracting trajectories exponentially [43]. While the inertial manifold is considered to be an important concept, it has been difficult to construct the inertial manifold of the partial differential equation in a concrete way. Yang *et al.* [42] divided Lyapunov vectors into 'physical' and 'isolated' modes in the case of the Kuramoto-Sivashinsky equation and complex Ginzburg-Landau equation and then speculated that there is some relation between the number of the physical mode and the dimension of the inertial manifold. These findings have a great importance since the existence of the inertial manifold and its dimension would justify numerical simulations of the dissipative partial differential equations with finite resolution[14].

Hyperbolicity and relation to physical property.— As mentioned above, Lyapunov vectors are tangent to stable and unstable manifolds of an invariant set, and we can study *hyperbolicity* of the invariant set by the Lyapunov vectors. Hyperbolicity is one of the fundamental properties of dynamical systems. A dynamical system is called to be hyperbolic if the tangent space of the phase space can be decomposed into stable and unstable sub-

[11]Ginelli *et al.* [36] called the covariant Lyapunov vectors by simply 'the Lyapunov vectors'. In this thesis, we refer to the covariant (or characteristic) Lyapunov vector as simply 'Lyapunov vector' in distinction from Gram-Schmidt vector.

[12]Hydrodynamic Lyapunov modes are long-wavelength Lyapunov modes associated with near-zero Lyapunov exponents, which is expected to give a novel insight into a many-body problem. See Yang and Radons [40] for details.

[13]The hyperbolic property they studied in [40] is 'partial domination of the Oseledec splitting' with respect to subspaces associated with near-zero Lyapunov exponents.

[14]Futhermore, Yang and Radons [44] proposed a method to compute the dimension and to study the geometry of the inertial manifolds of spatially extended dissipative dynamical systems by using Gram-Schmidt vectors.

spaces, i.e., the stable and unstable manifolds intersect at nonzero angles. When a dynamical system possesses the hyperbolic property, its theoretical analysis is easier in general compared with nonhyperbolic cases. Also, hyperbolicity is deeply connected to the structural stability of the dynamical systems [45]. Measurement of the angle between the local stable and the local unstable manifolds along the solution orbit shows whether the attractor is hyperbolic or not, and how far the hyperbolic attractor is from the nonhyperbolic state. (sometimes referred to as *degree of hyperbolicity*). Although there are some algorithms to compute global stable and unstable manifolds of steady solutions or periodic solutions and these algorithms have been applied to the solutions of fluid system [46, 47], it is still difficult to compute the stable and unstable manifolds of chaotic solutions. Saiki and Kobayashi [48] calculated angles between stable and unstable manifolds of Lorenz attractor by using the covariant Lyapunov analysis and identified a hyperbolic parameter region[15]. Also, by the covariant Lyapunov analysis, Kuptsov *et al.* [50] identified the hyperbolic parameter regions of the coupled Ginzburg-Landau equations. They found that the system becomes nonhyperbolic at the same parameter value where the third Lyapunov exponent becomes positive, and furthermore, argued that the system exhibits an extensive spatiotemporal chaos after the hyperbolic-nonhyperbolic transition. Artuso *et al.* [51] showed that a fixed point of some two-dimensional area-preserving map loses its hyperbolicity at certain control parameter values, which is associated with changes of the asymptotic decay rate of time correlation: when the system is hyperbolic the time correlation decays exponentially, and when the system is nonhyperbolic the time correlation decays algebraically. These findings are interesting in the way that they suggest that the change of the hyperbolic property has a physical interpretation as well. Considering these findings, It is natural to ask if the hyperbolic properties of physical systems such as fluids governed by the Navier-Stokes equation are related to their physical propertes. One of the goals of this thesis is to obtain the answer to this question.

What we study in this thesis.— In this thesis, we study orbital instability of turbulence through the covariant Lyapunov analysis. Here we focus our attention on the orbital instability of the chaotic Kolmogorov flow and the Couette turbulence. Kolmogorov flow is a fluid flow on the two-dimensional

[15]Recently they also studied manifold structures of UPOs embedded in the Lorenz attractor, and found that the angles between stable and unstable manifolds of them are related to appearance of periodic windows in a bifurcation diagram [49].

torus governed by the Navier-Stokes equation and its bifurcation and stability have been under intense study as it has been considered as a simplest example which contains essential elements of the Navier-Stokes flows. Couette turbulence is fluid turbulence between moving walls governed by the three-dimensional Navier-Stokes equation, and is sometimes referred to as a 'canonical example' of the wall-turbulence, often being studied with interests in the transition to turbulence and coherent structures in turbulence.

Recently, hyperbolicity of the chaotic Kolmogorov flow was studied by employing the covariant Lyapunov analysis, where the hyperbolic-nonhyperbolic transition was observed (§IV of [52]). In §2 of this thesis, we review the result of hyperbolic-nonhyperbolic transition appearing in the chaotic Kolmogorov flows. Here, our interest lies in relations between the hyperbolic properties and such physical properties of fluid motions as time correlation of the vorticity and the energy dissipation rate. First, we study the correlation decay of the vorticity at several Reynolds numbers across the hyperbolic-nonhyperbolic transition point. We find that the hyperbolic-nonhyperbolic transition is reflected in the qualitative change of the long-time correlation functions : before the transition the time-correlation function decays exponentially with oscillation and after the transition it decays purely exponential (i.e. the oscillation in time-correlation function vanishes at the transition point). Furthermore, examining the energy dissipation rate and the angle between the stable and unstable manifolds θ, we report that the angle θ tends to be small when the energy dissipation rate is large in a statistical sense.

In §3, we study the orbital instability of the Couette turbulence. Particularly we examine regeneration cycles observed in a wide variety of wall-turbulence including the Couette turbulence. The regeneration cycle is an important phenomenon consisting of breakdown (in the first half period of the cycle) and reformation (in the last half period of the cycle) of *streaks* which are well-known coherent structures (see §3 for a detailed description). The goal of this chapter is to characterize the regeneration cycle with the orbital instability by employing the covariant Lyapunov analysis.

First in §3, we present the Lyapunov spectrum of the Couette turbulence. From the Lyapunov spectrum, we obtain the dimension of the unstable manifold, the dimension of the attractor, and the Kolmogorov-Sinai entropy. Then we compare these information on the chaotic attractor with results reported in previous studies on the Floquet exponents of UPOs embedded in the turbulent attractor [69, 70], the normalized maximum Lyapunov exponent of the wall turbulence at the high Reynolds number [35], the attractor dimension of the Poiseuille turbulence [34], and the dimension of the dynamical system

models of the regeneration cycle [62].

Next, to see the orbital instability of the regeneration cycle in more detail, we study the local Lyapunov exponents and the associated Lyapunov modes. With these quantities, we find that (1) at the breakdown of the streaks, the Lyapunov modes indicate a *sinuous* instability which makes the streaks meander, (2) when the streamwise vorticity is highly localized, the local Lyapunov exponents appear to attain their maxima in the regeneration cycle, and (3) the local Lyapunov exponents decrease rapidly and become negative after the localization of the streamwise vorticity (i.e. they appear to be positive only in a very early stage of the cycle). These results suggest that the 'most unstable' instability during the regeneration cycle is the instability associated with strong localization of the streamwise vorticity rather than the sinuous instability. Also, instabilities are found only in a very early stage of the cycle and after that there are no exponential instability at all.

In the final part of §3, we reconsider the regeneration cycle from the viewpoint of the orbital instability. There, we argue the physical mechanisms of the streak meandering (breakdown) and the localization of the streamwise vorticity, which can be characterized by the Lyapunov modes. Particularly, we conclude that the localization of the streamwise vorticity is caused by the vortex stretching and propose a detailed mechanisms of it. Then, examining the evolution equation of the modal energy, we discuss the mechanism of the streak reformation which closes the cycle. We find that the streaks are reformed by interactions with mean flows and furthermore the energy is injected into the 'streak mode' from the mean flows almost *constantly* throughout the regeneration cycle. In other words, the interactions with mean flows reform the streaks throughout the cycle steadily. There, a natural question arises : what controls the development of the streaks (i.e. the regeneration cycle)? Finding an answer to the question, we study the energy flows in the system during the regeneration cycle in detail and detect the interaction between the streak mode and a 'meandering mode' that controls the regeneration cycle. The regeneration cycle in the wall turbulence is important not only for science but also for engineering, thus there are a great deal of research on the regeneration cycle. However, as far as we know, the orbital instability picture of the regeneration cycle described above has been never proposed.

Finally, in §4 we summarize the whole thesis and discuss future issues.

Chapter 2

Relations between hyperbolic properties and physical properties of chaotic Kolmogorov flow

2.1 Introduciton

Hyperbolicity is one of fundamental properties of dynamical system as mentioned in §1. Despite the importance of hyperbolic property, there are few examples of concrete dynamical systems whose hyperbolic properties are known in a rigorous manner. At present, we know the some exact results of hyperbolic properties of low-dimensional dynamical systems at best such as real Hénon family studied by Arai [53]. However recently, the covariant Lyapunov analysis gave us a new way to estimate hyperbolicity of even high-dimensional dynamical systems (Ginelli *et al.* [36]).

Fluid turbulence is often viewed as a typical example of chaos appearing in high-dimensional dynamical systems and hence hyperbolic property of turbulence can be important in understanding of it from the viewpoint of dynamical system. As a first step to obtain knowledge of the hyperbolic property of turbulence, Inubushi *et al.* [52] studied the degree of hyperbolicity of the Kolmogorov flows. This fluid system was proposed by Kolmogorov to study the stability and bifurcation of the solutions of the Navier-Stokes equation [17] and the route to chaos [54]. As shown in Fig.2.1, the Lyapunov exponents increase with the Reynolds number and the Kolmogorov flows be-

come chaotic ($\lambda_1 > 0$)[1] at the Reynolds number[2] $R/R_{cr} \simeq 18.2$, under which the fluid motion is quasi-periodic ($\lambda_1 = \lambda_2 = 0$) (see §III in [52] and §2.3 for details). Employing the covariant Lyapunov analysis, Inubushi *et al.* showed probability density functions of the angle between the local stable and unstable manifolds along the solution orbit and they found hyperbolic-nonhyperbolic transition at a certain Reynolds number (see §IV in [52] and §2.4).

The hyperbolic-nonhyperbolic transition may be expected to influence long-time statistical property of the flow. In order to study the physical properties of chaotic Kolmogorov flows, we here focus our attention on two physical quantities; the time-correlation of the vorticity and the enstrophy (the energy dissipation rate). This chapter is organized as follows. In §2.2, we describe Kolmogorov flow system and numerical method. Then in §2.3, we summarize briefly chaotic solution of Kolmogorov flows whose behavior is studied in later sections. We show the main result in this chapter in §2.4: relations between the hyperbolic properties and the physical properties of the system. §2.4.1 and §2.4.2 are devoted respectively to descriptions of relations between the degree of hyperbolicity and time correlation functions and relations between the angle θ and enstrophy. Finally, we summarize and discuss the obtained results in §2.5.

2.2 Kolmogorov flow system and numerical method

Kolmogorov flows are fluid flows governed by the two-dimensional incompressible Navier-Stokes equation and the vorticity equation which we solve numerically is

$$\partial_t \zeta + \boldsymbol{u} \cdot \nabla \zeta = \frac{1}{R}\Big(\Delta \zeta - n^3 \cos ny\Big), \tag{2.1}$$

where $\boldsymbol{u} = \boldsymbol{u}(x, y, t) = (u, v)$ is the velocity, $\zeta = \zeta(x, y, t) = \partial_x v - \partial_y u$ the vorticity, R the Reynolds number, n the wave number of the external forcing. Because of this simple form of external forcing, Kolmogorov flow has two kinds of symmetries ; if $\zeta(x, y)$ is a solution of the vorticity equation (2.1),

[1] In the Kolmogorov flow system, Pomeau-Manneville scenario leads to chaotic attractor with Type-I intermittency. See appendix A.1 and Inubushi *et al.* [9]

[2] R_{cr} is critical Reynolds number of "trivial solution". See later sections for details.

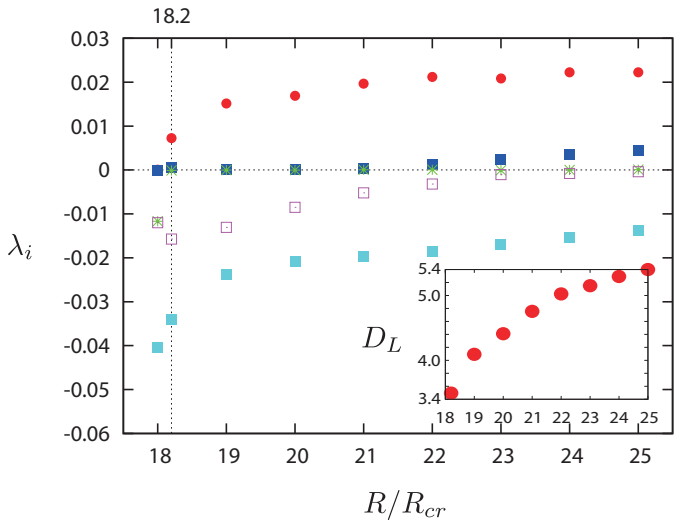

Fig. 2.1: Lyapunov exponents λ_i $(i = 1, 2, \cdots 5, \lambda_1 \geq \lambda_2 \geq \cdots \geq \lambda_5)$, the horizontal axis is Reynolds number R/R_{cr} $(18.0 \leq R/R_{cr} \leq 25.0)$. Inset ; Lyapunov dimension D_L. It is found that $3.5 \lesssim D_L \lesssim 5.5$ in this range of the Reynolds number

then $G^j\zeta(x,y)$ $(j = 1, 2, \cdots, 2n-1$, $G^j = \underbrace{G \circ \cdots \circ G}_{\text{j}})$ and $T_\alpha\zeta(x,y)$ $(\alpha \in [0, 2\pi))$ are also a solution, where

$$G\zeta(x,y) = -\zeta(-x, y - \tfrac{\pi}{n}) \tag{2.2}$$

$$T_\alpha\zeta(x,y) = \zeta(x - \alpha, y). \tag{2.3}$$

Roughly speaking, G represents a discrete "shift" by π/n in y direction and T_α represents a continuous "shift" by α in x direction.

The governing equation (1) possesses a steady solution $\zeta = -n\cos ny$ (so-called the trivial solution) and we denote by $R_{cr}(= n\sqrt{2})$ the critical Reynolds number beyond which the trivial solution becomes linearly unstable in the domain $x \in [0, 2\pi)$ (periodic) and $y \in (-\infty, \infty)$. Iudovich showed that for the forcing wavenumber $n = 1$, the trivial solution is globally and asymptotically stable [55]. Here we focus our attention on the chaotic solution of the Kolmogorov flows, in the case of the forcing wavenumber $n = 2$.

Direct numerical simulations of the vorticity equation (1) are performed by means of the standard 2/3 dealiased spectral method on the periodic domain $\mathbb{T}^2 = [0, 2\pi) \times [0, 2\pi)$ where the number of the grid points is 24×24,

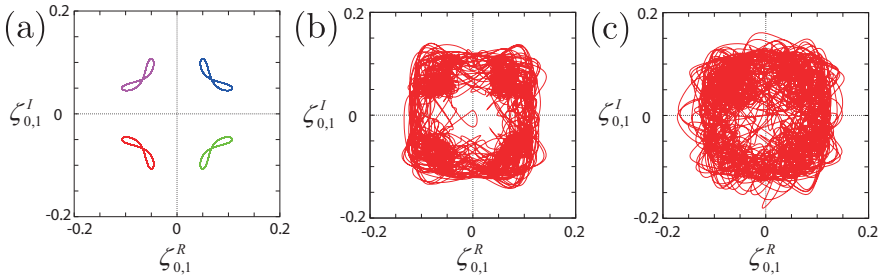

Fig. 2.2: The projection of the solution orbit onto $(\zeta^R_{0,1}, \zeta^I_{0,1})$ plane at (a) $R/R_{cr} = 18.0$, (b) $R/R_{cr} = 20.0$, (c) $R/R_{cr} = 24.0$ $(1.0 \times 10^4 \leq t \leq 3.0 \times 10^4)$. Only at (a) $R/R_{cr} = 18.0$, there are four solution orbits arising from four different initial conditions.

and truncated wave numbers were 7×7 as

$$\zeta(x, y, t) = \sum_{\substack{k=-K, \\ l=-L}}^{K,L} \zeta_{k,l}(t) e^{i(kx+ly)} \tag{2.4}$$

where $K = L = 7$. A state of the Kolmogorov flows is represented by a set of the Fourier coefficients

$$\begin{gathered}(\zeta^R_{-K,-L}(t), \zeta^I_{-K,-L}(t), \cdots, \zeta^R_{K,L}(t), \zeta^I_{K,L}(t)) \in \mathbb{R}^{N'} \\ (N' = 2(2K+1)(2L+1)),\end{gathered} \tag{2.5}$$

where $\zeta^R_{k,l}(t)$ and $\zeta^I_{k,l}(t)$ $(-K \leq k \leq K, -L \leq l \leq L)$ are respectively the real and imaginary parts of the complex Fourier coefficients $\zeta_{k,l}(t)$ satisfying the Hermitian symmetry, $\zeta_{k,l}(t) = \zeta^*_{-k-l}(t)$ where $*$ denotes the complex conjugate. In addition, ζ_{00} vanishes, and therefore the dimension of the phase space (degrees of freedom) of the truncated system is $N = (2K+1)(2L+1) - 1 = 224$. We used the library for spectral transform ISPACK [66], its Fortran90 wrapper library SPMODEL library [67] and the subroutine of LAPACK. For time integration, we used the 4th order Runge-Kutta method with the time step $\Delta t = 5.0 \times 10^{-3}$. For drawing the figures, the products of the Dennou Ruby project [68] and gnuplot were used.

2.3 Chaotic behavior of Kolmogorov flow

In this section, we summarize briefly the chaotic solution of Kolmogorov flows making use of the Lyapunov analysis. The time integration of the

vorticity equation (2.1) shows that the flows are quasi-periodic at $R/R_{cr} \lesssim 18.2$ and chaotic at $R/R_{cr} \gtrsim 18.2$. To clarify the instability of the flows, we calculate the Lyapunov exponents λ_i ($i = 1, 2, \cdots 5, \lambda_1 \geq \lambda_2 \geq \cdots \geq \lambda_5$) of Kolmogorov flow at different Reynolds numbers (Fig.2.1). Also, to illustrate the solution orbit in the phase space, in Fig.2.2 we show a projection of the solution orbit in the phase space onto $(\zeta^R_{0,1}, \zeta^I_{0,1})$ plane at R/R_{cr} = (a) 18.0, (b) 20.0, (c) 24.0 ($1.0 \times 10^4 \leq t \leq 3.0 \times 10^4$). We use four different initial conditions $\zeta^{(j)}_{k,l} (j = 0, 1, 2, 3)$

$$\zeta^{(j)}_{k,l} = \begin{cases} 0 & (k = l = 0), \\ \zeta^{(j)}_{01}\delta_{0,k}\delta_{1,l} + (1+i)\frac{10^{-3}}{k^2+l^2} & (\text{otherwise}), \end{cases} \tag{2.6}$$

where $\zeta^{(j)}_{0,1} = 0.2(1+i)\ e^{\frac{\pi}{2}ij}$ at $R/R_{cr} = 18.0$.

At $R/R_{cr} = 18.0$, there are four stable quasi-periodic solutions ($\lambda_1 = \lambda_2 = 0 > \lambda_i (i = 3, 4, \cdots N)$ Fig.2.2 (a)) due to the symmetry (2) of the system : G rotates the phase of Fourier component $\zeta_{0,1}$ by $\pi/2$ [rad], i.e. $G\zeta_{0,1} = i\zeta_{0,1}$. The quasi-periodic solution is composed of two plus/minus rapidly oscillating vortices (the period of oscillating motion $T_1 \simeq 35$) slowly traveling to x direction (the period of traveling motion $T_2 \simeq 1241$), which is confirmed by a power spectrum (see Fig.2.11). The two zero Lyapunov exponents $\lambda_1 = \lambda_2 = 0$ (Fig.2.1) are due to the property of the autonomous system and the translational symmetry in x direction of this system corresponding to T_α in the equation (2.3).

The Lyapunov exponents increase monotonically with Reynolds number (Fig.2.1). And at $R/R_{cr} \gtrsim 18.2$, the quasi-periodic solutions become unstable ($\lambda_1 > 0$) and merge into a large chaotic attractor composed of the four (unstable) quasi-periodic solutions and their connecting orbits (Fig.2.2 (b)). This route to chaos observed in the Kolmogorov flow can be characterized by so-called Type-I intermittency (see appendix A.1) [9]. The chaotic solution then wanders around the unstable quasi-periodic solutions and "jumps" between them intermittently. The energy ($E = \frac{1}{2}||\boldsymbol{u}||^2_{L^2}$) and the energy dissipation rate ($\varepsilon = 2Q/R$ where $Q = \frac{1}{2}||\zeta||^2_{L^2}$ is the enstrophy) also undergo intermittent bursts simultaneously with the "jumps" (Fig.2.3). The time series of the energy E and the energy dissipation rate ε are quite similar, bursting almost simultaneously. The energy injected by the external forcing dissipates so quickly, which implies the absence of the inertial subrange and the energy cascade in wavenumber space, in contrast with fully developed turbulence. Actually, the flow fields is in a state of not spatiotemporal but temporal chaos, consisting of two plus/minus large vortices oscillating chaotically in time. The

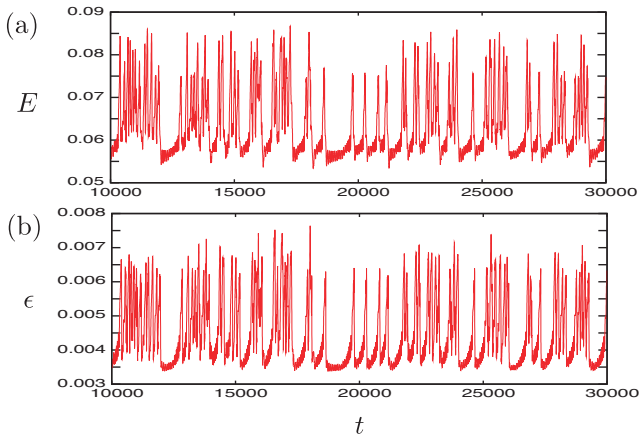

Fig. 2.3: Time series of the energy E and the energy dissipation rate ε at $R/R_{cr} = 20.0$ ($1.0 \times 10^4 \leq t \leq 3.0 \times 10^4$).

Lyapunov dimension $D_L = K + \frac{1}{|\lambda_{K+1}|}\sum_{i=1}^{K}\lambda_i$ ($K = \max\{m|\sum_{j=1}^{m}\lambda_j \geq 0\}$) (inset of Fig.2.1) is found to be rather small ($3.5 \lesssim D_L \lesssim 5.5$) in harmony with the observation of the temporal chaos. At $R/R_{cr} \simeq 23.0$, the 2nd positive Lyapunov exponent emerges, and at higher Reynolds number the solution orbit appears less trapped by the unstable quasi-periodic solutions (Fig.2.2 (c) at $R/R_{cr} = 24.0$).

2.4 Covariant Lyapunov analysis of chaotic Kolmogorov flow

In this section, we review the covariant Lyapunov analysis of chaotic Kolmogorov flow, in particular the study on degree of hyperbolicity[3].

Localization of the Lyapunov vector in physical space and wavenumber space is often related to characteristic physical properties of a chaotic behavior. In the "spiral defect" chaos in Rayleigh-Benard convection, the spatially localized pattern of the first Lyapunov vector is associated with the creation and annihilation of the defects [56], while in a shell model of turbulence (GOY model), an asymptotic scaling law of the Lyapunov spectrum can be obtained by using the localization property of Lyapunov vectors in wave number space

[3]Published in Inubushi *et al.* [52].

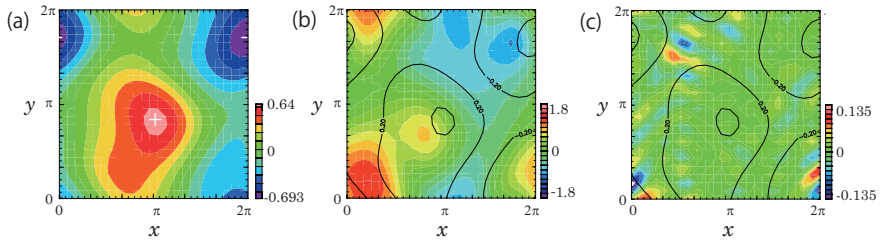

Fig. 2.4: Stream functions at $t = 1.0 \times 10^4$ of (a) solution, Lyapunov vectors corresponding to (b) λ_1 and (c) λ_{200} at $R/R_{cr} = 20.0$. The contours in (b),(c) shows the stream function of the solution.

and Kolmogorov scaling theory [32].

Now we can calculate the whole of the Lyapunov vectors by the covariant Lyapunov analysis for the chaotic Kolmogorov flows. Fig.2.4 (a) is the snapshot of the stream function of the chaotic solution as stated above and Fig.2.4 (b) and (c) are the stream functions of the Lyapunov vectors corresponding respectively to the Lyapunov exponent λ_1 and λ_{200} at $t = 1.0 \times 10^4$, $R/R_{cr} = 20.0$. The norm of the perturbation by the Lyapunov vector in Fig.2.4 (b) grows nearly exponentially ($\lambda_1 > 0$), while that in Fig.2.4 (c) decays nearly exponentially ($\lambda_{200} < 0$). The spatial scale of the first Lyapunov vector is nearly the same as the solution, and that of the 200th Lyapunov vector is smaller. This implies that the Lyapunov vectors corresponding to λ_1 (λ_{200}) is composed of low (high) wavenumber Fourier modes. Then we define the time averaged energy spectra $E(j,n) = \overline{E(j,n,t)}$ of the j-th Lyapunov vector $\boldsymbol{q}^{(j)}$ where the overline denotes time average $\bar{\cdot} = \frac{1}{T}\int_0^T \cdot\, dt$, $n = 1, 2, ..., \sqrt{K^2 + L^2}$ the total Fourier wavenumber, and

$$E(j,n,t) = \frac{1}{2\Delta_n} \sum_{n^2 \le k^2 + l^2 < (n+1)^2} \left(|\hat{u}^{(j)}_{k,l}(t)|^2 + |\hat{v}^{(j)}_{k,l}(t)|^2 \right).$$

Here $(\hat{u}^{(j)}_{k,l}, \hat{v}^{(j)}_{k,l})$ is the complex Fourier coefficient of the velocity $\boldsymbol{u}^{(j)} = (u^{(j)}(x,y), v^{(j)}(x,y))$ of the j-th Lyapunov vector $\boldsymbol{q}^{(j)}$ and $\Delta_n = \pi\{(n+1)^2 - n^2\}$. We use $T = 16.0 \times 10^4$ for the time average and the Lyapunov vector $\boldsymbol{q}^{(j)}$ is normalized with respect to the energy norm as $\frac{1}{2}||\boldsymbol{u}^{(j)}||^2_{L^2} = \sum_n E(j,n,t)\Delta_n = 1$. Fig.2.5 (a) shows $\log_{10} E(j,n)$ at $R/R_{cr} = 20.0$, where we confirmed that the qualitative properties do not depend on the Reynolds

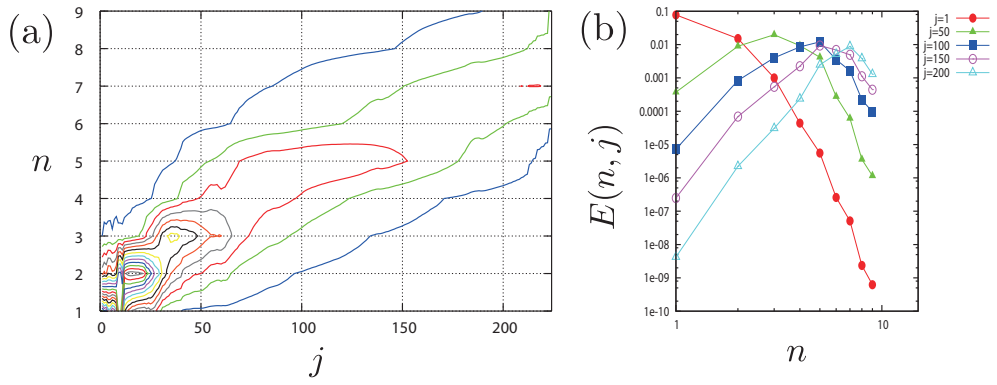

Fig. 2.5: (color online) (a) Energy spectra of Lyapunov vectors. The horizontal axis is the Lyapunov indices j, the vertical axis is Fourier wavenumber n and the contour is the energy spectra $\log_{10} E(j,n)$ at $R/R_{cr} = 20.0$. (b) the cross section of (a) fixed Lyapunov indices ($j = 1, 50, 100, 150, 200$).

number ($20.0 \leq R/R_{cr} \leq 24.0$). The energy spectra $E(j,n)$ for fixed Lyapunov index $j = 1, 50, 100, 150, 200$ are also shown in Fig.2.5 (b). It is found that the peak of energy spectrum shifts toward higher wavenumber with the increase of Lyapunov index. This is consistent with the dominance of small structures in Fig.2.4(c). This localization of Lyapunov vectors at high wavenumbers is in accidence with the correspondence between the Lyapunov exponents and the viscous dissipation, $\lambda \sim -\frac{1}{R}k^2$, where k is the localized wavenumber of the Lyapunov vector [32].

In order to evaluate the hyperbolicity of the chaotic motion, we calculate the probability density functions of the angle θ between the local stable and unstable manifolds along the solution orbit. Fig.2.6 is the closeup around zero angle ($0[\mathrm{rad}] \leq \theta \leq 0.1[\mathrm{rad}]$) of the PDF $P(\theta)$ at $R/R_{cr} = 20.0, 21.0, 22.0, 23.0, 24.0$ from top to bottom with error bars (see APPENDIX B in [52] for details).

We find that at the small Reynolds number ($R/R_{cr} \simeq 20.0$) the distribution of the angle vanishes at zero angle ($P(0) = 0$), which indicates that the attractor is hyperbolic. However, as the Reynolds number is increased, the angles θ has more chance to take smaller values and the distribution extends toward the zero angle. And at a certain Reynolds number ($R/R_{cr} \simeq 23.0$) the distribution of the angles is observed to reach the zero angle ($P(0) > 0$), which implies that the attractor becomes non-hyperbolic. It should be remarked that $R/R_{cr} \simeq 23.0$ is near the Reynolds number where the 2nd

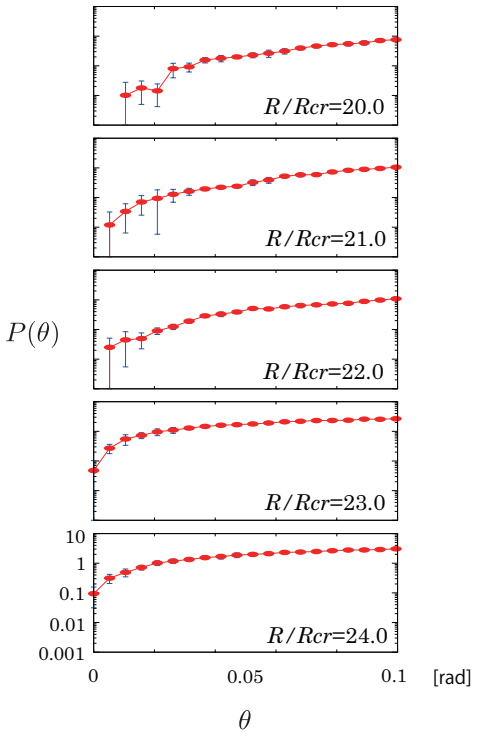

Fig. 2.6: (color online) Close-up ($0[\text{rad}] \leq \theta \leq 0.1[\text{rad}]$) of the PDF $P(\theta)$ at $R/R_{cr} = 20.0, 21.0, 22.0, 23.0, 24.0$ from top to bottom (linear-log plot) with error bars (see APPENDIX B in [52] for details).

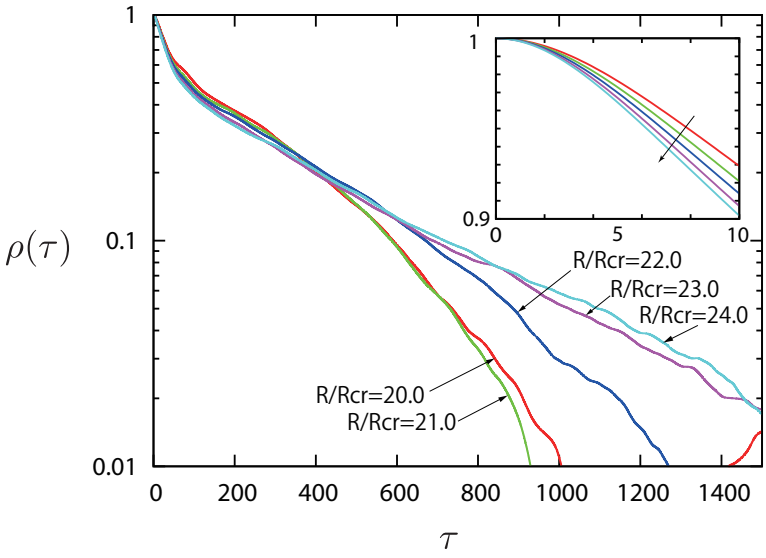

Fig. 2.7: The time-correlation function $\rho(\tau)$ (linear-log plot). Inset is an close-up of the time-correlation function in $0 \leq \tau \leq 10$ (the arrow indicates increase of the Reynolds number).

Lyapunov exponent become positive (Fig.2.1).

2.5 Relations between hyperbolic properties and physical properties of chaotic Kolmogorov flow

We expect that the hyperbolic-nonhyperbolic transition affects long-time statistical property of the flow, as mentioned in §2.1. In this section, the main part of this chapter, we focus our attention on two physical quantities; the time-correlation of the vorticity and the enstrophy (the energy dissipation rate).

2.5.1 Hyperbolicity and correlation fuction

The time-correlation function of the vorticity $\zeta(t) = \zeta(x', y', t)$ is defined as

$$\tilde{\rho}(\tau) = \overline{\zeta(t)\zeta(t-\tau)} - \overline{\zeta}^2. \tag{2.7}$$

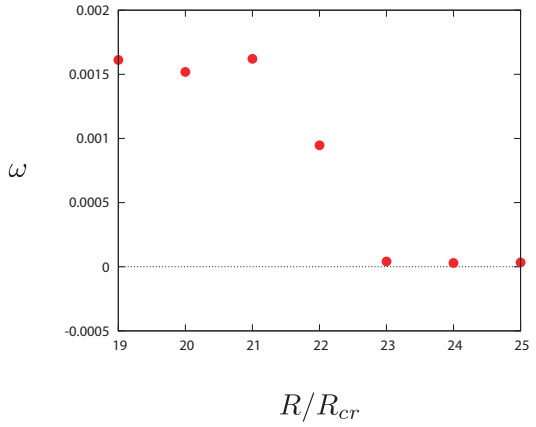

Fig. 2.8: Dependence of the fitting parameter ω on the Reynolds number ($19.0 \leq R/R_{cr} \leq 25.0$)

Fig.2.7 shows the normalized time-correlation function $\rho(\tau) = \langle\tilde{\rho}(\tau)\rangle/\langle\tilde{\rho}(0)\rangle$ at $(x', y') = (\pi/4, \pi/4)$ where $\langle\cdot\rangle$ denotes ensemble average over M different initial conditions. In the inset of the figure a close-up of the correlation function $\rho(\tau)$ in the short-time range ($0 \leq \tau \leq 10$) is presented. Each initial condition is the trivial solution with a random perturbation as

$$\zeta_{k,l}^{(i)} = \begin{cases} 0 & (k = l = 0) \\ -\frac{n}{2}\delta_{k,0}(\delta_{l,n} + \delta_{l,-n}) + P^{(i)} & (\text{otherwise}), \end{cases}$$

where $P^{(i)} = r^{(i)}(1+i)\frac{10^{-3}}{k^2+l^2}$ and $r^{(i)}(r = 1, 2, \cdots M)$ is uniform random numbers in an interval $[0, 1)$. We use $T = 2.0 \times 10^5$ and $M = 30$ and confirmed that the qualitative properties of correlation do not depend on the T, M and the observation point (x', y').

In a short-time range ($0 \leq \tau \leq 10$), chaotic Kolmogorov flows exhibit an algebraic decay ($\rho(\tau) \sim 1 - c\tau^2, c \simeq 0.0012$) of the time-correlation function independently of the Reynolds number. However, in long-time range ($\tau \gtrsim 100$) the decay of the time-correlation changes at $R/R_{cr} \simeq 22.0$; the time-correlation function at $R/R_{cr} = 20.0, 21.0$ decays super-exponentially, and changes its sign, while the time-correlation function at $R/Rcr = 23.0, 24.0$ has an exponential tail $\rho(\tau) \sim e^{-\tau/T}$.

We employ the least-square method to fit the time-correlation function with $\rho(\tau) = ae^{-\tau/T}\cos\omega\tau$ via three fitting parameters (a, T, ω) in long-time

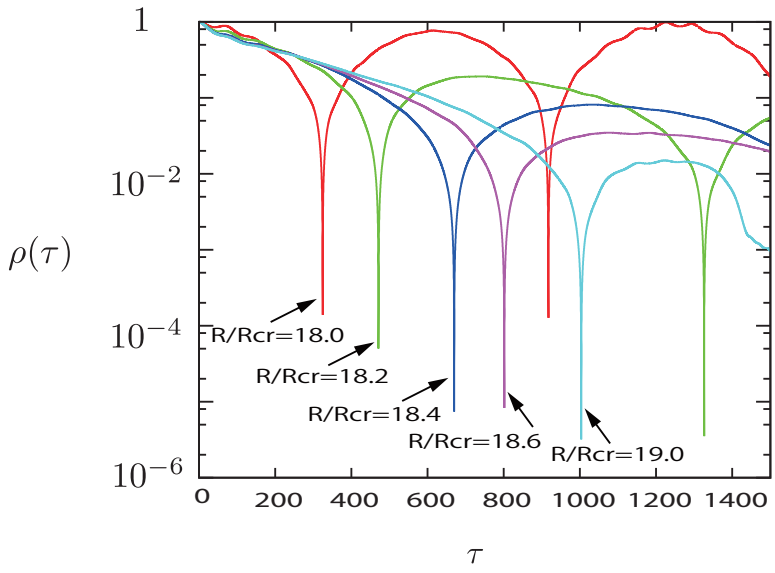

Fig. 2.9: The time-correlation function $\rho(\tau)$ (linear-log plot) at different Reynolds numbers $R/R_{cr} = 18.0$ (quasi-periodic solution) and $R/R_{cr} = 18.2, \cdots, 19.0$ (chaotic solution). The correlation function at $R/R_{cr} = 18.0$ oscillates and does not decay to zero as $\tau \to \infty$ because of the (quasi-)periodicity of the solution.

region ($100 \leq \tau \leq 900$). While the fitting parameters a and T are found to be almost independent of the Reynolds number (these change the value by 20% at most, see Fig.2.10, the fitting parameter ω depends strongly on the Reynolds number, as shown in Fig.2.8. Apparently, the value of the fitting parameter ω shows a clear transition from finite ($\omega \simeq 0.0015$) to 0 at $R/R_{cr} \simeq 22.0$. The qualitative change of the time-correlation of vorticity occurs at $R/R_{cr} \simeq 22.0$ close to that of the hyperbolic-nonhyperbolic transition and of the emergence of the 2nd positive Lyapunov exponent, suggesting that the asymptotic exponential decay of the time-correlation reflects the transition to nonhyperbolicity and/or the increase of the instability of the flow.

Oscillation of the correlation function.—We found that the long-time correlation function of the vorticity loses its oscillating part (i.e. $\omega \to 0$) at the Reynolds number close to the hyperbolic-nonhyperbolic transition point and to the Reynolds number where the 2nd positive Lyapunov exponent emerge. Here we study the origin of this oscillating part of the correlation

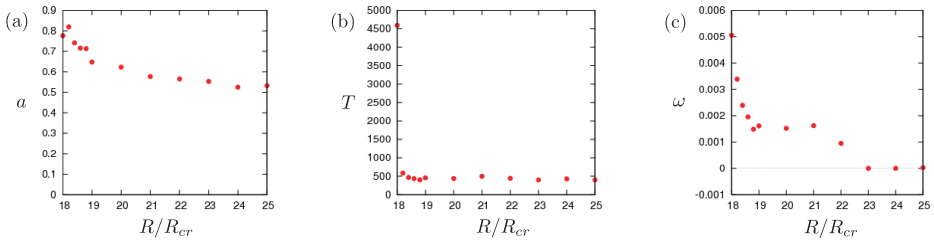

Fig. 2.10: Dependence of the fitting parameters (a, T, ω) on the Renolds numbers for (a) a, (b) T, (c) ω, where the asymptotic time-correlation functions are fit via the function form $\rho(\tau) = ae^{-\tau/T}\cos\omega\tau$.

function. Fig.2.9 shows the correlation functions at different Reynolds numbers $R/R_{cr} = 18.0, 18.2, \cdots, 19.0$. The quasi-periodic solutions are stable at $R/R_{cr} = 18.0$ and unstable at $R/R_{cr} \geq 18.2$. Correspondingly, the correlation function at $R/R_{cr} = 18.0$ oscillates and does not decay as $\tau \to \infty$. And at $R/R_{cr} \geq 18.2$, the correlation function also oscillates but decays to zero as $\tau \to \infty$, which is observed until $R/R_{cr} \sim 22.0$. This implies that this oscillation observed in the correlation functions comes from the quasi-periodic solutions. As a check of this scenario, we employ the least-square method to fit the time-correlation function with $\rho(\tau) = ae^{-\tau/T}\cos\omega\tau$. Fig.2.10 shows the dependence of fitting parameters (a, T, ω) on the Reynolds numbers. Apparently, in Fig.2.10 (a), the value of the fitting parameters a changes continuously with the increasing Reynolds numbers, which are reflected by the continuous change of the correlation functions. In Fig.2.10 (b), the value of the fitting parameters T change continuously with the Reynolds numbers except at $R/R_{cr} \sim 18.0$. Since the quasi-periodic solutions are stable at $R/R_{cr} = 18.0$, the value of the parameter T drastically changes from a large value at $R/R_{cr} = 18.0$ to smaller values at $R/R_{cr} \geq 18.2$ where the quasi-periodic solution is unstable. In Fig.2.10 (c), the value of the fitting parameters ω continuously decreases from $\omega^* \simeq 0.005$ to zero. At $R/R_{cr} = 18.0$, the angular velocities of the solution are respectively $\omega_1 = 0.18$ and $\omega_2 = 0.0051$ (Fig.2.11), the latter of which agrees with ω^* found in Fig.2.10 (c). The angular velocity ω_1 is not observed in Fig.2.10 (c) , probably because of its small amplitude.

These observations are summarized as follows; at $R/R_{cr} \sim 18.0$, $\rho(\tau) \sim a\cos\omega_1\tau + b\cos\omega_2\tau$ (quasi-periodic solution), at $18.0 \lesssim R/R_{cr} \lesssim 22.0$, $\rho(\tau) \sim ae^{-\tau/T}\cos\omega\tau$ (chaotic solution) and at $R/R_{cr} \gtrsim 22.0$, $\rho(\tau) \sim ae^{-\tau/T}$ (chaotic solution).

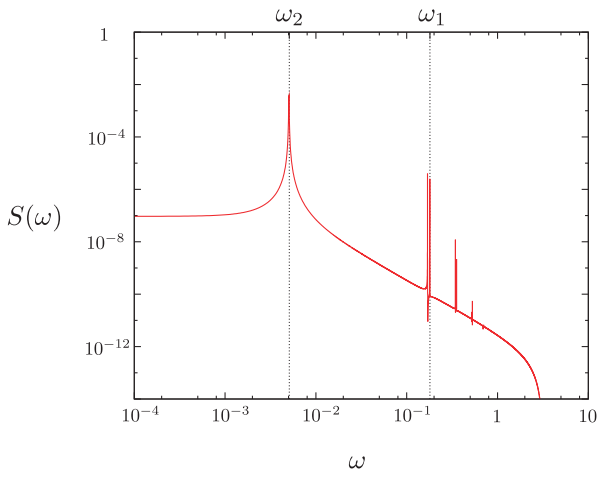

Fig. 2.11: Power spectrum $S(\omega)$ of the real part of the Fourier component $\zeta^R_{1,0}$ of the quasi-periodic solution at $R/R_{cr} = 18.0$. The vertical lines indicate $\omega_1 = 0.18$ and $\omega_2 = 0.0051$.

The correlation function loses its oscillating part at $R/R_{cr} \simeq 22.0$, which is close to the Reynolds number where the 2nd positive Lyapunov exponent emerge. While the oscillation of the correlation function comes from the quasi-periodic solutions, the appearance of "unstable mode" (corresponding to 2nd positive Lyapunov exponent) of the chaotic attractor may break the oscillating part of the correlation. This is a possible connection between the appearance of 2nd positive Lyapunov exponent and the change of the correlation function.

2.5.2 Angle between stable and unstable manifolds and enstrophy

Here we study the relation of the angle between the local stable and unstable manifolds, θ, and the enstrophy Q (the energy dissipation rate ε). Fig.2.12 shows the joint probability density functions (joint PDF) $P(\theta, Q)$ of the angle θ and the enstrophy Q measured along the solution orbit at (a) $R/R_{cr} = 20.0$, (b),$R/R_{cr} = 21.0$, (c) $R/R_{cr} = 22.0$, (d) $R/R_{cr} = 23.0$, (e)

$R/R_{cr} = 24.0$. The joint PDF $P(\theta, Q)$ was obtained in the form of a histogram with 200×200 bins over the range $[0, \pi/2) \times [0.0, 0.3]$ and normalized so as $\int \int P(\theta, Q) d\theta dQ = 1$. At $R/R_{cr} = 20.0, 21.0, 22.0$, the enstrophy takes

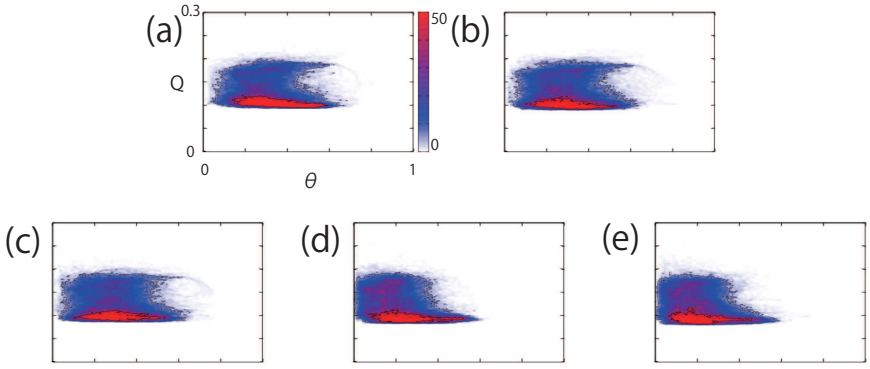

Fig. 2.12: Joint probability density functions of the enstrophy Q and the angle θ. The horizontal axis is the angle θ, the vertical axis is the enstrophy Q and the contour is the joint PDF at $R/R_{cr} =$ (a) 20.0, (b) 21.0, (c) 22.0, (d) 23.0, (e) 24.0.

both large and small values at large angles. However, at $R/R_{cr} = 23.0, 24.0$, it is observed that the enstrophy does not take large values at large angles. It may be worth noting that the change of the relation between the angle and the enstrophy takes place at the Reynolds number close to that of the hyperbolic-nonhyperbolic transition of the attractor.

2.6 Discussions and Conclutions

In the chaotic Kolmogorov flows, Inubushi *et al.* [52] observed the hyperbolic-nonhyperbolic transition (in §IV. of [52]) employing the covariant Lyapunov analysis [36]. Therefore In this chapter, we focused our attention on the relations between the hyperbolic and physical properties.

We studied the correlation decay of vorticity for several Reynolds numbers across the hyperbolic-nonhyperbolic transition point. In lower-dimensional dynamical systems hyperbolic/nonhyperbolic properties are known to be related to decay of correlations, especially, nonhyperbolicity usually leads to non-exponential decay of correlations. We found that the qualitative change

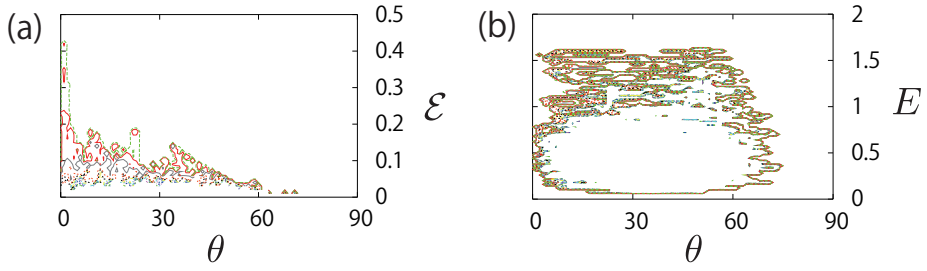

Fig. 2.13: Joint probability density functions of the angle θ and (a) the energy dissipation rate $\mathcal{E}$ and (b) energy E.

of the long-time correlation function occurs at the Reynolds number close to the hyperbolic-nonhyperbolic transition point and to the Reynolds number where the 2nd positive Lyapunov exponent emerge, suggesting that the asymptotic decay of the time-correlation reflects the transition to nonhyperbolicity and/or the emergence of "unstable mode" of the flow. Also, we reported that the angle θ is relevant to the enstrophy Q (the energy dissipation rate ε) ; the enstrophy is small when the angle is large, which holds at Reynolds numbers where the attractor is nonhyperbolic. A similar relation between the angle and the energy dissipation rate is also observed in GOY shell model (Kobayashi and Yamada [57]). They studied GOY model employing the covariant Lyapunov analysis and found that the angle between the stable and unstable manifolds θ is related to the energy dissipation rate in a similar manner (i.e. the angle θ tends to be small when the energy dissipation rate is large). Interestingly, this relation can not hold between the angle θ and the energy (in GOY model, the energy is not necessary correlated to energy dissipation rate as in fully developed turbulence). It will be intriguing future work to see how these properties relate to each other and whether this relation holds in general dissipative systems including fully developed Navier-Stokes turbulence.

Chapter 3

Orbital instability of the regeneration cycle in minimal Couette turbulence

3.1 Introduciton

As one of 'generic' properties of near-wall turbulence, a scaling law (known as *Prandtl wall law*) is observed in near wall region of a wide variety of wall turbulence such as turbulence in pipes, channels, ducts, and boundary layers, where a scaled mean velocity profile $\bar{u}(z)$ is logarithmic: $\bar{u}(z) \propto \log z$ (z is a scaled distance from the wall) [1]. A number of researchers have studied this statistical property, and flow structures (so-called *coherent structures*) have been recognized as key elements to understand near-wall turbulence (Jiménez and Moin [58], Hamilton *et al.* [59]). In order to find out mechanisms producing the wall turbulence, they searched numerically the minimal size of periodic box (minimal flow unit) in which we can observe the turbulence. As a result, in the minimal flow units, they found *regeneration cycle* consisting of breakdown and reformation of the coherent structures such as streamwise vortices and *streaks* which are high/low speed regions[2] in Poiseuille turbulence [58] and in Couette turbulence [59]. The regeneration cycle has been observed in many types of turbulence (Panton [60]) and was recently observed

[1] The streamwise mean flow profile scales with the kinetic viscosity ν and the wall friction velocity u_τ, where the wall friction velocity is $u_\tau = \sqrt{\nu \langle | \frac{\partial U_x}{\partial z} | \rangle_{\text{wall}}}$ (the bracket $\langle \cdot \rangle_{\text{wall}}$ denotes long-time and horizontal direction spatial mean at the walls and U_x is the streamwise mean velocity.).

[2] See Fig.3.5 and description of it for details.

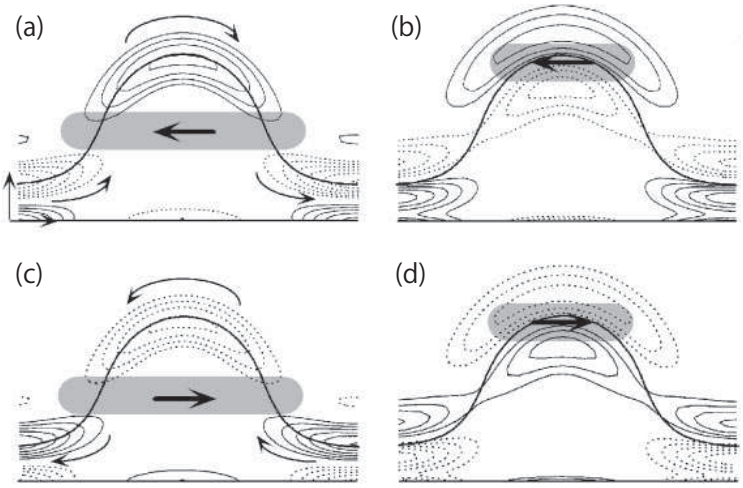

Fig. 3.1: Perturbation streamwise vorticity ω_x for sinuous streak instability mode of the model streak at (a) $\alpha x = 0$, (b) $\alpha x = \pi/2$, (c) $\alpha x = \pi$, and (d) $\alpha x = 3\pi/2$ shown in Fig.9 in Schoppa and Hussain [71], where α denotes the streamwise number. Positive and negative ω_x are shown as solid and dotted contours respectively, and the bell-shaped line denotes the phase speed contour $U = \sigma_i/\alpha$, where σ_i denotes the imaginary part of the eigenvalue. The shading shows the regions of induced spanwise flow (in the direction of the thick arrow).

in experiments of boundary layer turbulence by Duriez *et al.* [61].

In order to describe the regeneration cycle, Hamilton *et al.* [59] and Waleffe [62] proposed a mechanisms (what they call *self-sustaining process*) which consists of streak instability, regeneration of the streamwise vortices, and formation of the streaks, by modeling the streaks and the streamwise vortices. On the streak instability, Schoppa and Hussain [71] investigated linear stability of models of the streaks numerically and found that these models are linearly unstable to *sinuous* instability mode (Fig.3.1. See also Figure 9 in [71]) which causes meandering of the straight streak as observed by Hamilton *et al.* [59]. Linear stability of a corrugated vortex sheet, which is an inviscid model of the streak, is studied by Kawahara *et al.*[72]. They found the vortex sheet is linearly unstable equally to both sinuous and varicose disturbances (i.e. their growth rates are identical) in a long-wave limit and

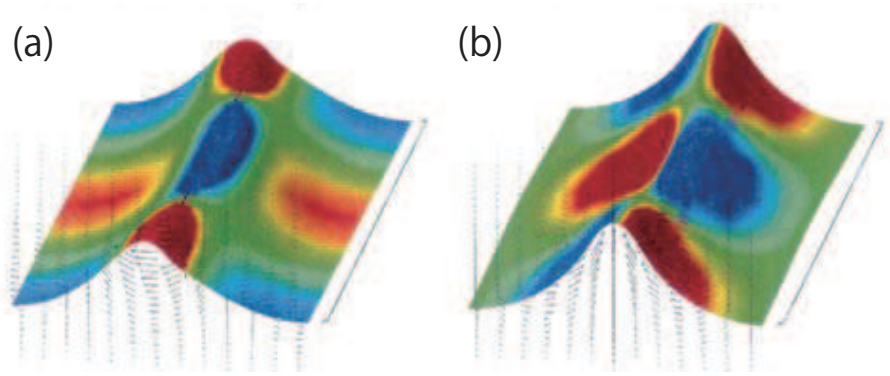

Fig. 3.2: Unstable fundamental eigenstructures of a corrugated vortex sheet shown in Figure 3 (c,d) in Kawahara [72] for (a) sinuous mode and (b) varicose mode. The streamwise circulation density (see [72] for details) in the perturbed vortex sheet is shown for $\xi_0 = 1/3\pi$ where ξ_0 denotes positions of the sheet. Red is positive (clockwise) and blue is negative (counterclockwise). The disturbance velocity vectors, in a frame of reference moving with the real part of the phase velocity, are shown in the plane $x = 0$. One wavelength is shown both in the x- and in the z-directions.

discussed similarities between the obtained sinuous eigenfunction (Fig.3.2. See also Figure 3 in [72]) and the invariant solutions of the Poiseuille flows and the Couette flows. There are numerous studies on linear stability of model streaks including the above models (see [72] and references therein) and most of them suggest that the sinuous mode is the most unstable (often referred to as the most 'dangerous') perturbations. Characteristics of the sinuous instability modes are (A) appearances of different signs streamwise vorticity alternatively, (B) localizations of streamwise vorticity near the low-speed streak 'crest' and the high-speed 'trough' regions (see Fig.3.1 and Fig.3.2). However these models are not solutions of the full Navier-Stokes equation and it is unclear how the linear stability analyses of these models of steady solutions are crucial for understanding of the stability of the streak in the actual turbulent flows.

Following the meanderings of the straight streaks, the flow changes into fully three-dimensional turbulence, and streamwise vortices are expected to be generated. Toward an understanding of this process, many mechanisms has been proposed such as Waleffe [62] and Jiménez and Moin [58] (See Kawa-

hara [69] for review of regeneration mechanisms of streamwise vortices). Once the streamwise vortices are generated by some sort of mechanism, these vortices advect the gradient of the streamwise velocity in the cross-streamwise plane, which forms the streak structures. In other words, the streamwise vortices lift up low-velocity fluid from the bottom wall, and lifted down high-velocity fluid from the top wall. Kawahara [69] showed that an analytical model of the streamwise vortex forms the streak structures by the above mechanism. The formation of the streaks closes the regeneration cycle. Waleffe [62] derived a low-dimensional model for understanding of the regeneration cycle (self-sustaining process) from the viewpoint of dynamical system theory, which has been modified and used to study transitions to turbulence over a wide parameter region (Kim and Moehlis [75]). While these descriptions and models are suggestive, the mechanisms composing the regeneration cycle, particularly the generation mechanism of the streamwise vortices, remain unclear. Moreover, the whole of the regeneration cycle is expected to be understood not on the basis of the models and the phenomenological arguments but on the full Navier-Stokes equation.

One of the crucial steps toward understanding of the regeneration cycle on the basis of the full Navier-Stokes equation is finding of the UPO by Kawahara and Kida [25] which approximates turbulent statistics very well as mentioned in §1. Also, they found that temporal variations of spatial structures along the UPO exhibit the regeneration cycle. Recently, a lot of invariant solutions of the full Navier-Stokes equation and the (homoclinic and heteroclinic) connections between them have been found numerically and used to clarify the state space structures for understanding mechanisms of transition to turbulence and the regeneration cycle (see §1 for the brief review and Kawahara [29] for the detailed review).

We here focus our attention on the properties of the orbital instabilities of minimal Couette turbulence employing the covariant Lyapunov analysis, by which we can study 'linear stability' of the streaks in actual turbulence instead of the model streaks. Moreover, the covariant Lyapunov analysis is expected to capture not only the streak instability but also the other exponential instabilities in the whole of the regeneration cycle. Understanding of the instabilities of the cycle can be useful for a control of turbulence as well (Kawahara [22]). Also, some fundamental information on the attractor can be obtained by the analysis such as the attractor dimension[3] and

[3]The attractor dimension of the minimal Couette turbulence is considered to be not high since the regeneration cycle can be characterized by only two coherent structures (i.e. the streak and the streamwise vortex) and dynamics of several low-dimensional models

Kolmogorov-Sinai entropy. The goals of this chapter are to characterize the mechanisms composing the regeneration cycle in terms of the orbital instability and contribute toward an understanding of the cycle on the basis of the full Navier-Stokes equation.

In §3.2 we describe problem setting, equation of motion, and numerical methods used in this chapter. The results of time integration are shown in §3.3, where we observe the regeneration cycle discussed in the previous studies. There, we see localization events of streamwise vorticities in detail, which play an important role in later sections. In §3.4, we present main results of this chapter, namely characterization of the regeneration cycle through the covariant Lyapunov analysis; Lyapunov spectrum, local Lyapunov exponents, and associated Lyapunov vectors. Based on the results above section, we discuss in detail the regeneration cycle in a manner consistent with properties of orbital instabilities. In §3.5, discussions and conclusions are given.

3.2 Couette flow system and numerical method

3.2.1 Problem setting

Plane Couette flow is a fluid system where incompressible viscose fluid is in between upper and lower walls (the width is $2h$) and the fluid motion is driven by the walls moving in the opposite direction (the velocity of the walls are $\pm U_0$, respectively). As shown in Fig.3.3, we refer to the direction which the wall is moving along as *streamwise* or x-direction, the direction which is normal to the walls as *wall-normal* or z-direction, and the direction which is normal to x-z plane as *spanwise* or y-direction[4]. The domain is $(x, y, z) \in \Omega = [0, L_x h] \times [0, L_y h] \times [-h, h]$. Kawahara [22] sets the streamwise flux and the spanwise mean pressure gradient to be zero and we here employ the same conditions.

3.2.2 Equation of motion

We non-dimensionalize lengths in units of h, velocity in units of U_0, pressure in units of $U_0^2 \rho$ where ρ is the fluid density. Reynolds number is $Re =$

can resemble those of the actual regeneration cycles (for instance the 8-dimensional model proposed by Waleffe [62]). However, Keefe *et al.* [34] found that the attractor dimension of the wall-turbulence at relatively high Reynolds number is $D \simeq 780$. Thus it is not trivial how large the attractor dimension of the turbulence is.

[4]This coordinate setting is the same as Clever and Busse [64]

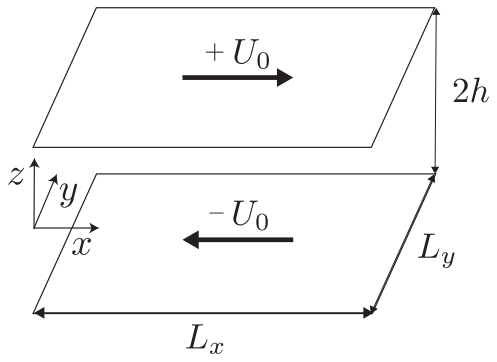

Fig. 3.3: Illustration of plane Couette flow system. x, y, z-direction are referred to as *streamwise, spanwise, wall-normal* direction, respectively.

$U_0 h/\nu$ where ν is the kinematic viscosity. Non-dimensionalised Navier-Stokes equation and the incompressible condition is

$$\frac{\partial \boldsymbol{u}}{\partial t} + (\boldsymbol{u}\cdot\boldsymbol{\nabla})\boldsymbol{u} = -\boldsymbol{\nabla} p + \frac{1}{Re}\boldsymbol{\nabla}^2\boldsymbol{u}, \tag{3.1}$$

$$\boldsymbol{\nabla}\cdot\boldsymbol{u} = 0 \tag{3.2}$$

where $\boldsymbol{u} = (u_x, u_y, u_z)$ is the non-dimensionalised velocity, p is the non-dimensionalised pressure defined in the domain $(x, y, z) \in [0, L_x] \times [0, L_y] \times [-1, 1]$.

We use non-slip boundary condition on the walls ($z = \pm 1$);

$$u_x(x, y, \pm 1) = \pm 1, \tag{3.3}$$

$$u_z(x, y, \pm 1) = u_y(x, y, \pm 1) = 0, \tag{3.4}$$

and periodic boundary condition in a horizontal direction;

$$\boldsymbol{u}(x, y, z) = \boldsymbol{u}(x + L_x, y, z) = \boldsymbol{u}(x, y + L_y, z), \tag{3.5}$$

$$\boldsymbol{\nabla} p(x, y, z) = \boldsymbol{\nabla} p(x + L_x, y, z) = \boldsymbol{\nabla} p(x, y + L_y, z). \tag{3.6}$$

Here, we describe procedures for obtaining evolution equations which we actually solve numerically. First, we decompose the velocity and pressure field to the mean part and the fluctuation part respectively (appendix B.1.1).

Then, we derive the evolution equations of the mean filed and the fluctuation field (appendix B.1.2). Next, we set the mean pressure gradient and the mean flux (appendix B.1.3). Finally, boundary conditions of the means and fluctuation flows are fixed (appendix B.1.4).

Employing toroidal and poloidal potential (see appendix B.1.2), these procedures lead to the equation of motion as the forms of vorticity equations (evolution equations of toroidal and poloidal potential) and mean flow equations;

$$\begin{cases} \frac{\partial}{\partial t}\boldsymbol{\nabla}_H^2\tilde{\psi} + \boldsymbol{e}_z \cdot \boldsymbol{\nabla} \times (\boldsymbol{u} \times \boldsymbol{\omega}) = \frac{1}{Re}\boldsymbol{\nabla}_H^2\boldsymbol{\nabla}^2\tilde{\psi} \\ \frac{\partial}{\partial t}\boldsymbol{\nabla}_H^2\boldsymbol{\nabla}^2\tilde{\phi} - \boldsymbol{e}_z \cdot \boldsymbol{\nabla} \times \boldsymbol{\nabla} \times (\boldsymbol{u} \times \boldsymbol{\omega}) = \frac{1}{Re}\boldsymbol{\nabla}_H^2\boldsymbol{\nabla}^2\boldsymbol{\nabla}^2\tilde{\phi} \\ \frac{\partial}{\partial t}\boldsymbol{U} + \frac{\partial}{\partial z}\langle u_z \boldsymbol{u}\rangle_H = -\frac{1}{Re}\left\langle \frac{\partial^2 U_x}{\partial z^2} \right\rangle_V \boldsymbol{e}_x + \frac{1}{Re}\frac{\partial^2 \boldsymbol{U}}{\partial z^2}. \end{cases} \tag{3.7}$$

where $\boldsymbol{\omega}$ denotes the vorticity vector ($\boldsymbol{\omega} = \boldsymbol{\nabla} \times \boldsymbol{u}$), $\tilde{\psi}$ and $\tilde{\phi}$ denote respectively the toroidal and poloidal potential of the fluctuation velocity field, $\boldsymbol{\nabla}_H^2$ denotes the horizontal Laplacian ($\boldsymbol{\nabla}_H^2 = \partial_x^2 + \partial_y^2$), and $\langle\cdot\rangle_H$ denotes the horizontal mean and $\langle\cdot\rangle_V$ denotes the volume mean such that

$$\left\langle \cdot \right\rangle_H = \frac{1}{L_x L_y}\int_0^{L_y}\int_0^{L_x} \cdot \, dxdy, \tag{3.8}$$

$$\left\langle \cdot \right\rangle_V = \frac{1}{2L_x L_y}\int_{z=-1}^{z=+1}\int_{y=0}^{y=L_y}\int_{x=0}^{x=L_x} \cdot \, dxdydz. \tag{3.9}$$

Correspondingly the boundary conditions of the potentials and the mean flows are

$$\begin{cases} \tilde{\phi}(x,y,\pm 1) = \frac{\partial\tilde{\phi}}{\partial z}(x,y,\pm 1) = \tilde{\psi}(x,y,\pm 1) = 0 \\ \tilde{\psi}(x,y,z) = \tilde{\psi}(x+L_x,y,z) = \tilde{\psi}(x,y+L_y,z) \\ \tilde{\phi}(x,y,z) = \tilde{\phi}(x+L_x,y,z) = \tilde{\phi}(x,y+L_y,z) \\ U_x(z=\pm 1,t) = \pm 1 \\ U_y(z=\pm 1,t) = 0. \end{cases} \tag{3.10}$$

It is to be noted that the streamwise volume flux must be zero initially;

$$\langle u_x(x,y,z,0)\rangle_V = 0. \tag{3.11}$$

3.2.3 Numerical method

Direct numerical simulation of Couette flow

Following the setting of the minimal Couette flow, the domain sizes are set to be $L_x = 1.755\pi$ and $L_y = 1.2\pi$ for the domain $(x, y, z) \in [0, L_x] \times [0, Ly] \times [-1, 1]$ and the Reynolds number is set to be $Re = 400$ [22]. The dealiased Fourier expansions are employed in the horizontal (x-y) directions, and the Chebyshev tau methods are employed in the wall-normal (z) direction. The toroidal potential, for example, is expanded as follows

$$\psi(x, y, z) = \sum_{k=-KM}^{KM} \sum_{l=-LM}^{LM} \sum_{m=0}^{MM} \hat{\psi}_{(k,l,m)} e^{i(\alpha k x + \beta l y)} T_m(z) \tag{3.12}$$

where $\hat{\psi}_{(k,l,m)}$ is the expansion coefficient, $\alpha = 2\pi/L_x$ and $\beta = 2\pi/L_y$ is the fundamental streamwise and spanwise wavenumbers respectively, and $T_m(z)$ is the m-th order Chebyshev-polynomial. We set the truncation mode numbers $KM = 8$(x-direction), $LM = 8$(y-direction), $MM = 32$(z-direction) and the grid points are $32 \times 32 \times 33$ (in $x, y,$ and$z$). The time integration is performed with the 2nd order Adams-Bashford method with a time step width $\Delta t = 1.0 \times 10^{-3}$. The resolution we use here is almost the same as (or higher than) the often used resolution [25]. The CFL number is less than 0.1 which is less than Philip and Manneville [65] use in the similar setting. The friction Reynolds number $Re_\tau (= u_\tau h/\nu)$ is $Re_\tau = 34.0$ and the periods of the domain in streamwise and spanwise direction normalized by $l_\tau = \nu/u_\tau$ are $L_x^+ = L_x/l_\tau = 187$ and $L_y^+ = L_y/l_\tau = 128$ respectively, which is in good agreement with the values reported in Kawahara [25]. The grid spacing in the x, y and z direction normalized by l_τ is $\Delta x^+ = 5.9$, $\Delta y^+ = 4.0$, and $\Delta z^+ = 0.16$-3.3 (the minimum-maximum grid spacing), which is comparable to those in most direct numerical simulations [59].

We used the library for spectral transform ISPACK [66], its Fortran90 wrapper library SPMODEL library [67] and the subroutine of LAPACK. For drawing the figures, the products of the Dennou Ruby project [68] and gnuplot were used.

covariant Lyapunov analysis

Here we describe the numerical methods of covariant Lyapunov analysis which we use in this paper. We consider the Couette flow as a dynamical system and the state vector $\boldsymbol{X}$ is defined by the spectral coefficients

$\hat{\psi}_{(k,l,m)}, \hat{\phi}_{(k,l,m)}, \hat{U}_{x(m)}, \hat{U}_{y(m)}$ of the potentials ψ, ϕ and the mean flow fields U_x, U_y as follows

$$\boldsymbol{X} = \left(\hat{\psi}_{(-K,-L,0)}, \cdots, \hat{\psi}_{(K,L,M)}, \hat{\phi}_{(-K,-L,0)}, \cdots, \hat{\phi}_{(K,L,M)}, \hat{U_x}_{(0)}, \cdots, \hat{U_x}_{(M)}, \hat{U_y}_{(0)}, \cdots, \hat{U_y}_{(M)}\right) \in \mathbb{R}^N \tag{3.13}$$

where N is the number of the degrees of freedom given by $N = 2((2KM + 1)(2LM + 1) - 1)(MM + 1) + 2(MM + 1) = 19,074$. Inner product we use here for Lyapunov analysis is defined by

$$(\boldsymbol{X}, \boldsymbol{Y})_{\mathcal{E}} = \frac{1}{2}\left\langle \boldsymbol{\omega_X} \cdot \boldsymbol{\omega_Y} \right\rangle_V \tag{3.14}$$

where $\boldsymbol{\omega_X}$ ($\boldsymbol{\omega_Y}$) is the vorticity vector field calculated from the state vector $\boldsymbol{X}$ ($\boldsymbol{Y}$). We use an induced norm from the inner product $(\cdot,\cdot)_{\mathcal{E}}$ which is volume average enstrophy; $||\boldsymbol{X}||^2 = (\boldsymbol{X}, \boldsymbol{X})_{\mathcal{E}}$.

Linearized evolution equation of this system is given by

$$\begin{cases} \frac{\partial}{\partial t}\boldsymbol{\nabla}_H^2\psi' + \boldsymbol{e}_z \cdot \boldsymbol{\nabla} \times (\boldsymbol{u} \times \boldsymbol{\omega}') + \boldsymbol{e}_z \cdot \boldsymbol{\nabla} \times (\boldsymbol{u}' \times \boldsymbol{\omega}) = \frac{1}{Re}\boldsymbol{\nabla}_H^2\boldsymbol{\nabla}^2\psi' \\ \frac{\partial}{\partial t}\boldsymbol{\nabla}_H^2\boldsymbol{\nabla}^2\phi' - \boldsymbol{e}_z \cdot \boldsymbol{\nabla} \times \boldsymbol{\nabla} \times (\boldsymbol{u}' \times \boldsymbol{\omega}) - \boldsymbol{e}_z \cdot \boldsymbol{\nabla} \times \boldsymbol{\nabla} \times (\boldsymbol{u} \times \boldsymbol{\omega}') = \frac{1}{Re}\boldsymbol{\nabla}_H^2\boldsymbol{\nabla}^2\boldsymbol{\nabla}^2\phi' \\ \frac{\partial}{\partial t}\boldsymbol{U}' + \frac{\partial}{\partial z}\langle {u_z}'\boldsymbol{u}\rangle_H + \frac{\partial}{\partial z}\langle u_z\boldsymbol{u}'\rangle_H = -\frac{1}{Re}\left\langle \frac{\partial^2 {U_x}'}{\partial z^2} \right\rangle_V \boldsymbol{e}_x + \frac{1}{Re}\frac{\partial^2\boldsymbol{U}'}{\partial z^2} \end{cases} \tag{3.15}$$

where the prime $'$ denotes small perturbations; $\psi,\ \phi,\ U_x,\ U_y\ \rightarrow\ \psi+\psi',\ \phi+\phi',\ U_x + {U_x}',\ U_y + {U_y}'$.

Boundary condition of the perturbation is the same as the base flow except the streamwise mean flow U_x'. It is natural that the boundary condition of streamwise mean flow of the perturbation flow is set to be zero on the walls; $U_x'(z = \pm 1) = 0$, while that of the base flow is $U_x(z = \pm 1) = \pm 1$.

We calculate the time evolution of the linearized flows by the same way as the base flow (2nd order Adams-Bashford method) using the Message Passing Interface (MPI) where each cpu calculates each linearized flow. We set the time interval of the QR decomposition $T_{QR} = 1$ and after the every QR decompositions we employ the Euler method for just 1 step to calculate the linearized flows.

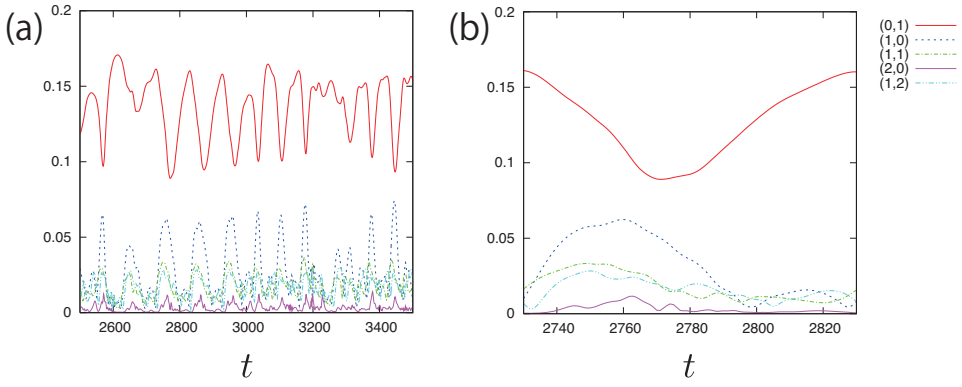

Fig. 3.4: Time series of model RMS velocities $\sqrt{\langle|\hat{\boldsymbol{u}}(\boldsymbol{k})|^2\rangle_z}$ for (a) multiple regeneration cycles (b) single regeneration cycle. Solid line (red) : $\boldsymbol{k} = (0, 1)$, dotted line (blue) : $\boldsymbol{k} = (1, 0)$, dashed dotted (green) : $\boldsymbol{k} = (1, 1)$, thin solid line (pink) : $\boldsymbol{k} = (2, 0)$, and dashed double-dotted (light blue) : $\boldsymbol{k} = (1, 2)$.

3.3 Turbulent behavior of minimal Couette flow

Here we see the turbulent behavior of minimal Couette flow briefly. First of all, we show time series of modal RMS velocities[5] $\sqrt{\langle|\hat{\boldsymbol{u}}(\boldsymbol{k}, z)|^2\rangle_z}$ in Fig.3.4 where $\boldsymbol{k} = (k, l) \in \mathbb{Z}^2$ and $\hat{\boldsymbol{u}}(\boldsymbol{k}, z) = \hat{\boldsymbol{u}}(k, l, z)$ is the Fourier coefficient of the velocity filed : $\hat{\boldsymbol{u}}(\boldsymbol{k}, z) = \langle \boldsymbol{u}(x, y, z)e^{-i(k_x x+k_y y)}\rangle_H$ ($k_x = \alpha k, k_y = \beta l$). Hereafter we may drop z-dependence of $\hat{\boldsymbol{u}}(\boldsymbol{k}, z)$ as $\hat{\boldsymbol{u}}(\boldsymbol{k})$ for simplicity. As reported by Hamilton *et al.* [59], the time series of the modal RMS velocities oscillate nearly periodically (multiple regeneration cycles in Fig.3.4 (a)) and the period of the oscillation T_p is approximately $T_p \simeq 100$ (single regeneration cycle in Fig.3.4 (b)). Specifically, it is found that the amplitude of y-independet mode ($\boldsymbol{k}$=(1,0)) increases when that of x-independent mode ($\boldsymbol{k}$=(0,1)) decreases.

Corresponding to the time series of the regeneration cycles (Fig.3.4 (b)), the flow fields change in time nearly periodically. In Fig.3.5 (a-f), we show snap shots of the streamwise velocity field $u_x(\boldsymbol{x})$ (contour lines) and the streamwise vorticity field $\omega_x(\boldsymbol{x})$ (tone levels) at $t = 2730$ (a), 2750 (b), 2760

[5]The definition of the 'modal RMS velocity' is slightly different from that of Hamilton *et al.* [59] by a factor $\sqrt{2}$.

(c), 2770 (d), 2790 (e), 2820 (f). Upper figure of each snap shot is cross-sectional view taken along $z = 0$ and lower one is cross-sectional view taken along $x = 1.5$ (indicated by a small arrow in Fig.3.5 (a)) The regeneration cycle can be observed in these snap shots. At the beginning of the cycle ($t = 2730$), flow field is almost x-independent, which corresponds to the predominance of the modal RMS velocity of the $\boldsymbol{k} = (0, 1)$ mode in the time series. It is particularly worth noting that the high and low speed regions form so-called streak structures consisting of an upward shift of the low streamwise velocity region and a downward shift of the high streamwise velocity region (see the cross-sectional veiw). The (high and low speed) streaks are well known as the one of the key structures in trying to understand the regeneration cycle. The x-independent structures soon break up and the streaks start to meander ($t = 2750, 2760$), which corresponds to the growth of the modal RMS velocity of the $\boldsymbol{k} = (1, 0)$ and the higher modes in the time series. In a narrow region between the meandering structures of the streaks, plus and minus streamwise vortices appear strongly along nearly $z = 0$ plane ($t = 2760$). We consider that these localized strong streamwise vortices are also key structures in understanding regeneration cycle especially from a point of view of instability in the flow.

In order to characterize the localization of the streamwise vortices, we show time series of 'horizontal' RMS of the streamwise vorticity $\sqrt{\langle \omega_x^2 \rangle_H}$ at $z = 0$ in Fig.3.6. When the x-independent streaks begin to meander ($t = 2730$), the 'horizontal' RMS of the streamwise vorticity begins to increase. Moreover, It is found that the 'horizontal' RMS of the streamwise vorticity achieve a strong and sharp peak just before $t = 2760$, indicating the strong localization of the streamwise vortices along $z = 0$ plane. Almost at the same time, the modal RMS velocities except $\boldsymbol{k} = (0, 1)$ mode reach maximum values (see Fig.3.4).

After the disappearing of the streamwise vortices, the x-independent streaks regenerate ($t = 2770, 2790, 2820$), which closes the regeneration cycle.

We can divide the regeneration cycle into two phase using the sharp peak of the 'horizontal' RMS of streamwise vorticity; (i) streak meandering phase (before the peak) and (ii) streak reformation phase (after the peak). In the time series of the Fig.3.6, the phase (i) shifts to the phase (ii) at the peak $t \simeq 2760$ of the 'horizontal' RMS of streamwise vorticity.

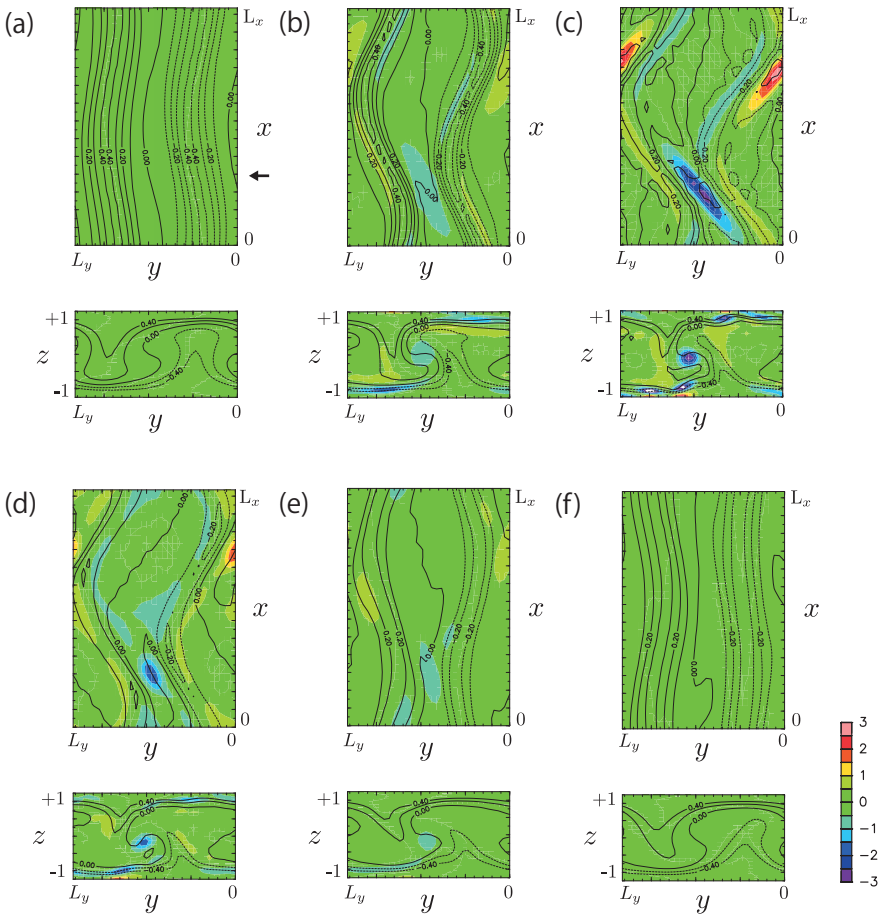

Fig. 3.5: Snap shots of the streamwise velocity field $u_x(\boldsymbol{x}, t)$ (contour lines) and the streamwise vorticity field $\omega_x(\boldsymbol{x}, t)$ (tone levels) at (a): $t = 2730$,(b): $t = 2750$, (c): $t = 2760$, (d): $t = 2770$, (e): $t = 2790$, (f): $t = 2820$. Upper figure of each snap shot is cross-sectional view taken along $z = 0$ and lower one is cross-sectional view taken along $x = 1.5$ (indicated by a small arrow in (a))

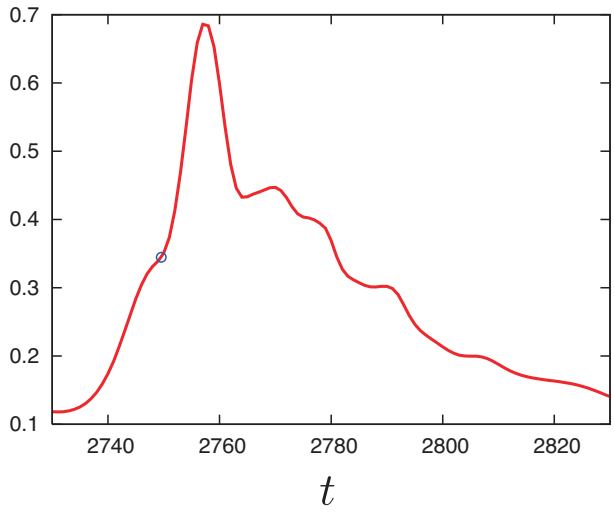

Fig. 3.6: Time series of 'horizontal' RMS of streamwise vorticity $\sqrt{\langle\omega_x^2\rangle_H}$ of the single regeneration cycle at the mid-plane ($z = 0$). Blue circle in the figure represents the value of $\sqrt{\langle\omega_x^2\rangle_H}$ at $t = 2750$ for reference in a later section.

3.4 Orbital instability of the regeneration cycle in minimal Couette turbulence

For over five decades (see Schoppa and Hussain [71] and references therein), a number of researchers have discussed the regeneration cycle observed in the previous section. While their findings are highly suggestive, they are on the basis of the models and the phenomenological arguments. Here we study the orbital instability of the regeneration cycle toward characterizing it quantitatively on the basis of the full Navier-Stokes equation. In particular, we show the Lyapunov spectrum, local Lyapunov exponents, and associated Lyapunov mode of the regeneration cycle in the minimal Couette turbulence.

Fig.3.7 shows Lyapunov spectrum λ_j ($j = 1, 2, \cdots, 30$) of Couette turbulence. It is found that Couette turbulence possesses four positive Lyapunov exponents ($\lambda_j > 0$ ($j = 1, 2, 3, 4$)), three zero Lyapunov exponents ($\lambda_j = 0$ ($j = 5, 6, 7$)), and minus Lyapunov exponents ($\lambda_j < 0$ ($j \geq 8$)). The zero Lyapunov exponents correspond to the symmetries of the dynam-

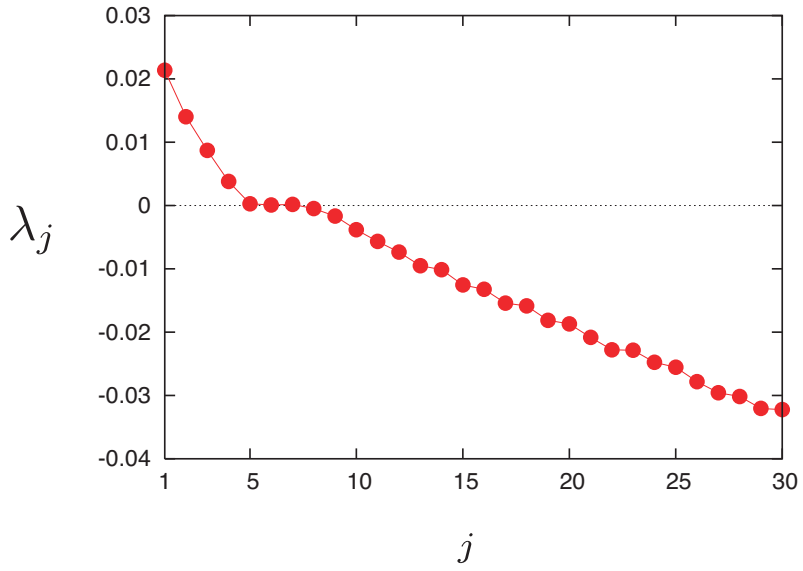

Fig. 3.7: Lyapunov spectrum λ_j ($j = 1, 2, 3, \cdots, 30$) of the minimal Couette turbulence. The number of positive Lyapunov exponents is four ($\lambda_j > 0$ ($j = 1, 2, 3, 4$)) and the number of zero Lyapunov exponents is three ($\lambda_j = 0$ ($j = 5, 6, 7$)). The maximum Lyapunov exponent is $\lambda_1 = 0.021$.

ical system; time translational symmetry and spatial translational symmetries in horizontal directions (x, y). The maximum Lyapunov exponent λ_1 is $\lambda_1 = 0.021$ and a corresponding time scale ($T_L = 1/\lambda_1$) is nearly half (or slightly less than) the 'period' of regeneration cycle; $T_L \simeq T_p/2$. Interestingly, the maximum Lyapunov exponent is close to the maximum Floquet exponent $\mu = 0.019$ of the 'strong' unstable periodic orbit reported by Kawahara [69][6]. Besides, the Floquet exponents of unstable (relative) periodic orbits calculated by Viswanath [70] are also near the maximum Lyapunov exponent ($\mu = 0.023 \sim 0.035$. See the TABLE 1. in Viswanath [70]). Lyapunov dimension $D_L \big(= K + \frac{1}{|\lambda_{K+1}|} \sum_{j=1}^{K} \lambda_j \big)$ is $D_L = 14.8$ where K is the largest in-

[6]In this paper (p.16 and p.19), they reported that the period of the strong periodic orbit is $T \simeq 65$ and the most unstable Floquet multiplier is − 3.4 [69]. Therefore the Floquet exponent is calculated by $\mu = \ln 3.4/65 = 0.018827....$

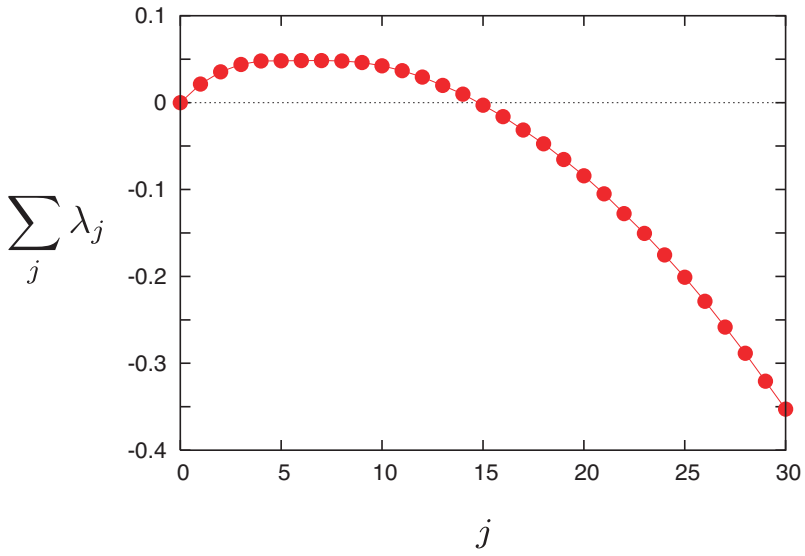

Fig. 3.8: Summation of the Lyapunov spectrum $\sum_j \lambda_j$ $(j = 1, 2, 3, \cdots, 30)$ of the minimal Couette turbulence. to calculate Lyapunov dimension and Kolmogorov-Sinai entropy. The Lyapunov dimension is $D_L = 14.8$ and Kolmogorov-Sinai entropy is $h_{\mathrm{KS}} = 0.048$.

teger such that $\sum_{j=1}^{K} \lambda_j \geq 0$ (Fig.3.8). Kolmogorov-Sinai entropy estimated by summation of the positive Lyapunov exponents is $h_{\mathrm{KS}} = 0.048$.

The existence of the positive Lyapunov exponents indicates that there are some instability mechanisms which play an important role in driving the regeneration cycle. We here study the instability mechanisms in the regeneration cycle via local Lyapunov exponents $\tilde{\lambda}_j(t, \tau)$. Temporal variations of the local Lyapunov exponents $\tilde{\lambda}_j(t, \tau)$ $(j = 1, 2, 3, 4)$ are shown in a upper panel of Fig.3.9 and the temporal variations of the 'horizontal' RMS of streamwise vorticity is shown in a lower panel of Fig.3.9 (the same time series as Fig.3.6, but including three regeneration cycles). We set $\tau = 1$ and write $\tilde{\lambda}_j(t, 1) = \tilde{\lambda}_j(t)$ hereafter. The local Lyapunov exponents $\tilde{\lambda}_j(t)$ $(j = 1, 2, 3, 4)$ shown in Fig.3.9 are positive after the longtime averaging as shown in Fig.3.7. It is found that the local Lyapunov exponents tend to be positive during the phase (i) and negative during (ii), although they fluctuate quickly over time.

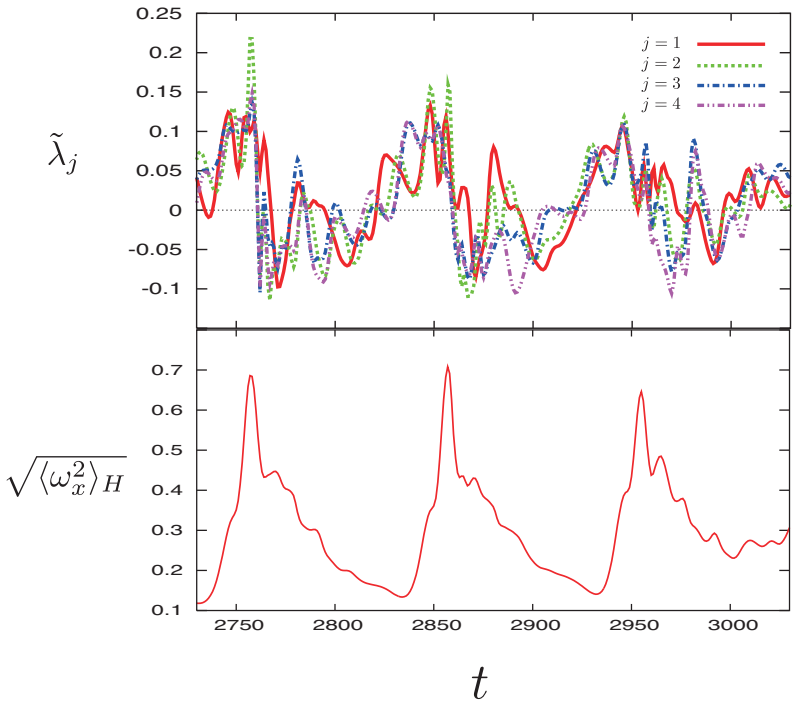

Fig. 3.9: [upper panel] Time series of local Lyapunov exponents $\tilde{\lambda}_j(t)$ for solid line (red) : $j = 1$, dotted line (green) : $j = 2$, dashed dotted (blue) : $j = 3$, and dashed double-dotted (pink) : $j = 4$. [lower panel] The 'horizontal' RMS of streamwise vorticity $\sqrt{\langle \omega_x^2 \rangle_H}$ at the mid-plane ($z = 0$).

Roughly speaking, the period of the fluctuation is about $10 \sim 20$ which indicates that the local stability of the flow is sensitive to the details of the base flow as observed in Hamilton *et al.* [59][7]. Moreover, the local Lyapunov

[7]They described the stability of the base flows as follows ; "The principal limitation of the linear approach is that the 'base' flow we are trying to analyse evolves on the same time scale as the instability. The choice of a base flow corresponding to a peak in $M(0, \beta)$ for the stability computation was for this reason somewhat arbitrary. A base flow obtained from data at $t = 753.8$, just slightly before the peak at $t = 757.5$, gives rather different results. At the earlier time, only the α-modes are unstable, while at the later time, both the α-and the 2α-modes grow. Clearly, the linear analysis is sensitive to the details of the base flow.". See §5 in Hamilton *et al.* [59] for details.

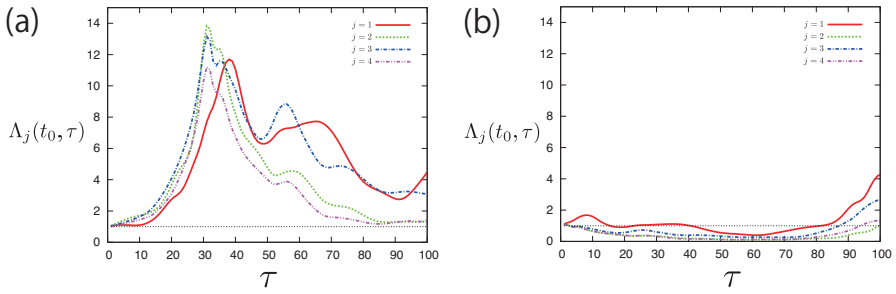

Fig. 3.10: Accumulative expanding rate $\Lambda(t_0,\tau)$; (a) $t_0 = 2730$, (b) $t_0 = 2760$ for $\tilde{\lambda}_j(t)$ for solid line (red) : $j = 1$, dotted line (green) : $j = 2$, dashed dotted (blue) : $j = 3$, and dashed double-dotted (pink) : $j = 4$. The black dot horizontal line denotes $\Lambda_j(t_0,\tau) \equiv 1$ (i.e. nutral).

exponents appear to reach their maximum values (i.e. most unstable state in the regeneration cycle) at the peak of the 'horizontal' RMS of streamwise vorticity and suddenly decrease to zero and minus values (i.e. stable period in the regeneration cycle) after the peak. These observations suggest that the localized streamwise vortices in the mid-plane have a key influence on the instability of the flow.

How does the infinitely small perturbation added the flow actually evolve? By definition, the amplitude of the perturbation along j-th Lyapunov vector evolves as $||v_j(t+\tau)|| = ||v_j(t)||e^{\tilde{\lambda}_j(t,\tau)\tau}$. Thus we define *accumulative expanding rate* as $\Lambda_j(t,\tau) = e^{\tilde{\lambda}_j(t,\tau)\tau}$. When we add the perturbation at time $t = t_0$, the accumulative expanding rate $\Lambda_j(t_0,\tau)$ measures the ratio of the norm of the perturbation at $t = t_0 + \tau$ to that of $t = t_0$, i.e. $||v_j(t_0+\tau)|| = ||v_j(t_0)||\Lambda_j(t_0,\tau)$, as a function τ. Fig.3.10 shows the accumulative expanding rate $\Lambda_j(t_0,\tau)$ where (a) $t_0 = 2730$ (the initial stage of phase (i))and (b) $t_0 = 2760$ (the final stage of phase (i)) for $\tilde{\lambda}_j(t)$ $(j = 1,2,3,4)$. In the appendix B.2, we show the accumulative expanding rate for $\tilde{\lambda}_j(t)$ $(1 \le j \le 20)$ which displays almost the same behaviors. In Fig.3.10 (a), clearly small perturbations grow until $\tau \simeq 30$ $(t_0 + \tau = 2760)$ and the peaks of the growth of the perturbations are close to that of the 'horizontal' RMS of the streamwise vortices. Furthermore, after reaching its maximum, it is considered that the streamwise vortices never destabilize the flow since the small perturbations hardly grow and decay until $\tau \simeq 70$; the flow is (neutral) stable (Fig.3.10 (b)). In other words, it suggests that there is no exponential instability in the phase (ii).

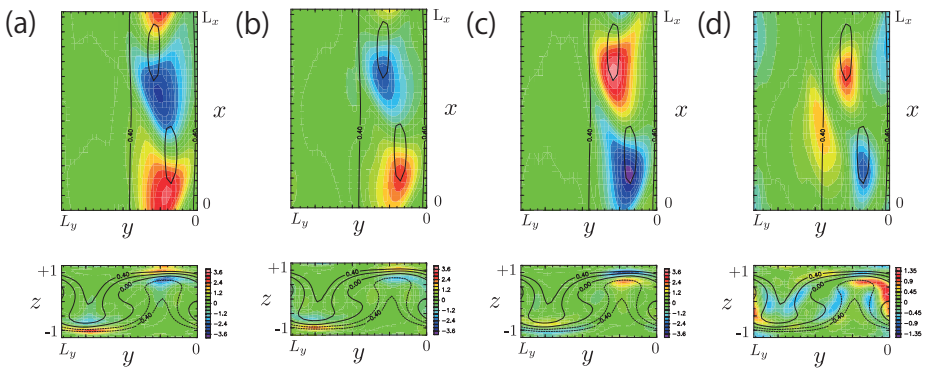

Fig. 3.11: Lyapunov modes at the initial stage of the phase (i) ($t = 2730$). Streamwise vorticities of the Lyapunov modes $\delta\omega_{xj}$ are shown as color tone for (a); $j = 1$, (b); $j = 2$, (c); $j = 3$, (d); $j = 4$ and streamwise velocities of the base flow are shown as counter lines.

Examining the exponential instabilities in the phase (i) more closely, we next see Lyapunov modes associated to the Lyapunov exponents. Firstly we show the Lyapunov modes at the initial stage of the phase (i) ($t = 2730$) in Fig.3.11. The streamwise vorticities of the Lyapunov modes $\delta\omega_{xj}$ are shown as color tone for (a); $j = 1$, (b); $j = 2$, (c); $j = 3$, (d); $j = 4$ and streamwise velocities of the base flow (the turbulent solution) are shown as counter lines. The Lyapunov modes are normalized by the enstrophy norm as $1/2\langle|\delta\boldsymbol{\omega}_j|^2\rangle_V = 1$. Tone levels are set $|\delta\omega_{xj}| \leq 4.0$ for (a),(b),(c) and $|\delta\omega_{xj}| \leq 1.5$ for (d). Upper figure of each panel is cross-sectional view taken along $z = 0.8$ and lower one is cross-sectional view taken along $x = 1.5$. Here we consider the physical significance of the Lyapunov modes except the fourth Lyapunov mode which is not localized in space and its physical interpretation is not well understood at this time. The streamwise vorticities of the Lyapunov modes $\delta\omega_{xj}$ ($j = 1, 2, 3$) are found to be localized near-wall regions of $u_x = 0$ sheet in the cross-stream plane (lower panel) and the signs of those appear alternately in streamwise direction (upper panel). Moreover, The vorticities of the Lyapunov modes $\delta\omega_{xj}$ ($j = 1, 2, 3$) are nearly even function to the each high and low speed streak; $\delta\omega_j(x, y_0 - \Delta_y, z) \simeq \delta\omega_j(x, y_0 + \Delta_y, z)$ where $y_0 \simeq L_y/4$ or $3L_y/4$ for small Δ_y.

The other cross-sectional views of the 1st (i.e. most unstable) Lyapunov modes at the same time ($t = 2730$) are shown in Fig.3.12 along (a); $x = L_x/4$,

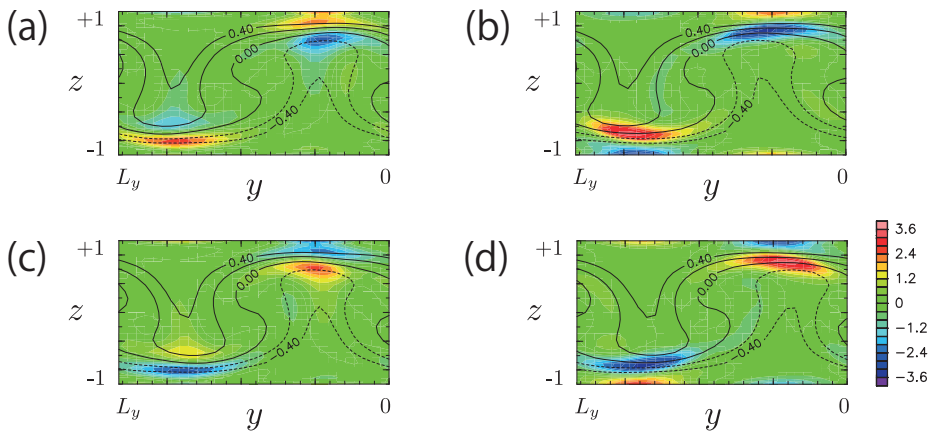

Fig. 3.12: Cross-sectional views of the most unstable Lyapunov mode at the initial stage of the phase (i) ($t = 2730$) at (a); $x = L_x/4$, (a); $x = L_x/2$, (a); $x = 3L_x/4$, (a); $x = L_x$. Streamwise vorticities of the Lyapunov mode $\delta\omega_{x1}$ are shown as color tone and streamwise velocities of the base flow are shown as counter lines.

(a); $x = L_x/2$, (a); $x = 3L_x/4$, (a); $x = L_x$. Streamwise vorticities of the Lyapunov mode $\delta\omega_{x1}$ are shown as color tone and streamwise velocities of the base flow are shown as counter lines. These snap shots are taken at the initial stage of the phase (i) ($t = 2730$), thus these Lyapunov modes can be related to the meandering of the x-independent streaks. In fact, the patterns of the Lyapunov modes are similar to that of the eigenfunctions (so-called sinuous streak instability modes) as a result of linear instability analysis of the model streak calculated by Schoppa and Hussain [71] (Fig.3.1) and the corrugated sheet calculated by Kawahara *et al.* [72] (Fig.3.2 (a)). Particularly, we can see the characteristics of the sinuous instability mode in the patterns of the Lyapunov modes, i.e. (A) appearances of different signs streamwise vorticity alternatively, (B) localizations of streamwise vorticity near the low-speed streak 'crest' and the high-speed 'trough' regions. Hence we conclude that the Lyapunov modes observed here correspond to the sinuous mode appearing in the linear stability analysis of the model streak. Moreover it is found that the sinuous streak instability mode is important not only in the linear stability of the stationary solution (models) but also in the asymptotic stability of the turbulent solution.

Following the growth of the sinuous mode and the meandering of the

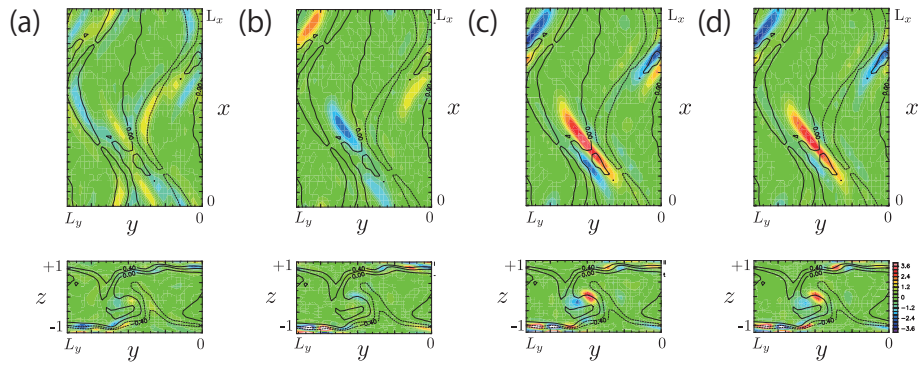

Fig. 3.13: Lyapunov modes at the final stage of the phase (i) ($t = 2760$). Streamwise vorticities of the Lyapunov modes $\delta\omega_{xj}$ are shown as color tone for (a); $j = 1$, (b); $j = 2$, (c); $j = 3$, (d); $j = 4$ and streamwise velocities of the base flow are shown as counter lines.

streaks, the observation of the local Lyapunov exponents indicates another instability mechanism related to the streamwise vortices as mentioned above. Clarifying the instability mechanism, we show the Lyapunov mode at the final stage of the phase (i) in Fig.3.13. The streamwise vorticities of the Lyapunov modes $\delta\omega_{xj}$ are shown as color tone for (a); $j = 1$, (b); $j = 2$, (c); $j = 3$, (d); $j = 4$ and streamwise velocities of the base flow (the turbulent solution) are shown as counter lines as well as in Fig.3.11. The Lyapunov modes are normalized by the enstrophy norm as $1/2\langle|\delta\boldsymbol{\omega}_j|^2\rangle_V = 1$. Tone levels are set $|\delta\omega_{xj}| \leq 4.0$ for all panels. Upper figure of each panel is cross-sectional view taken along $z = 0$ (mid-plane) and lower one is cross-sectional view taken along $x = 1.5$. It is found that the streamwise vorticities of the Lyapunov modes $\delta\omega_{xj}$ (particularly $j = 3, 4$) localize at the narrow space between the meandering streaks where the streamwise vorticities of the turbulent solution also localize seen in Fig.3.5 (c). This observation supports the idea that the the localization of the streamwise vortices in the final stage of the phase (i) is a source of the instability of the flow.

3.5 Regeneration cycle from a viewpoint of orbital instability

Here we consider the regeneration cycle of Couette turbulence from a standpoint of orbital instability, which partially overlaps with the self-sustaining mechanisms proposed by the previous studies. Firstly we describe important mechanisms in the phase (i); mechanisms of the streak meandering and the generation of the streamwise vortices. Then we discuss a key mechanism closing the regeneration cycle in the phase (ii); a reformation mechanism of the x-independent streak. Finally the regeneration cycle mentioned above is summarized by examining 'energy flow' in the dynamical system.

3.5.1 Phase (i); How do the streaks mender and the streamwise vortices appear?

From the observation of the domination of $\boldsymbol{k} = (0, 1)$ mode in the modal RMS velocities $\sqrt{\langle|\hat{\boldsymbol{u}}(\boldsymbol{k}, z)|^2\rangle_z}$ (Fig.3.4) and the snap shot of the flow (Fig.3.5 (a)), the predominant structure of the flow at the initial stage of the phase (i) is clearly (almost) x-independent streak. It is well known that large 'amplitude' streak steady solution and streak model are linearly unstable and the most unstable eigenmode is the sinuous mode [72]. Moreover, the covariant Lyapunov analysis presented here clarified that the sinuous instability causes not only the meandering of the model streak but also the meandering of the streak in the turbulent flows.

Following the streak meandering by the sinuous instability, the streamwise vorticties localize strongly along the mid-plane as shown in Fig.3.5 (c) and Fig.3.6. Here we consider the mechanism generating the localized streamwise vortices. Fig.3.14 shows snap shots of the streamwise velocity field $u_x(\boldsymbol{x}, t)$ (contour lines) and the streamwise vorticity field $\omega_x(\boldsymbol{x}, t)$ (tone levels) at (a): $t = 2748$,(b): $t = 2750$, (c): $t = 2752$, (d): $t = 2754$. We can see the streamwise vortices generation in these snap shots: the positive streamwise vortex appear around $(x, y, z) = (3L_x/4, 0, 0)$ and the negative streamwise vortex appear around $(x, y, z) = (L_x/4, L_y/2, 0)$ in Fig.3.14 (d). By observing carefully these snap shots, it is found that there are small amplitude vorticities already in Fig.3.14 (a)[8] and the small amplitude vorticities grow into the localized streamwise vortices with time. Moreover, the time series

[8]See the appendix B.3 for a detailed generation mechanism of these small amplitude vorticities.

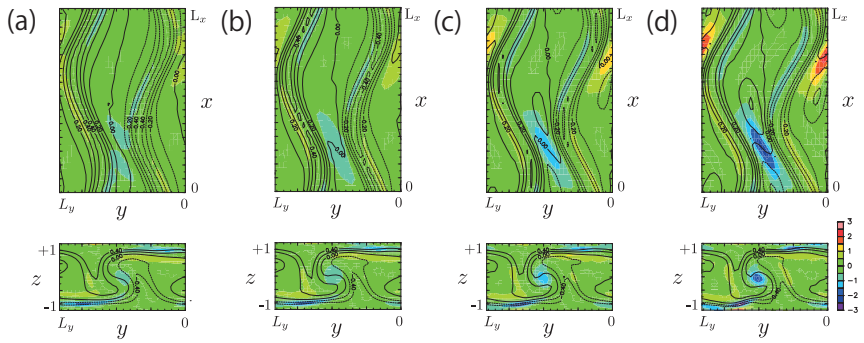

Fig. 3.14: Snap shots of the streamwise velocity field $u_x(\boldsymbol{x}, t)$ (contour lines) and the streamwise vorticity field $\omega_x(\boldsymbol{x}, t)$ (tone levels) at (a): $t = 2748$,(b): $t = 2750$, (c): $t = 2752$, (d): $t = 2754$. Planes of the cross-sectional views are the same as that of Fig.3.5.

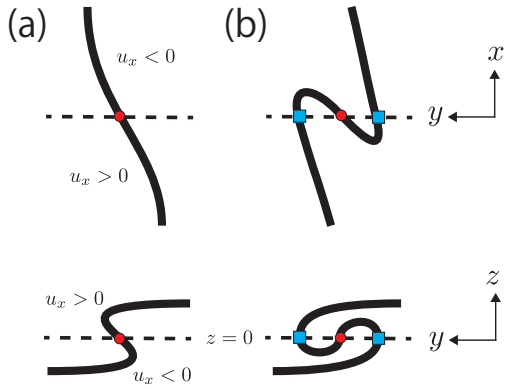

Fig. 3.15: Illustration of the formation mechanism of the positive gradient region of the streamwise velocity ($\partial_x u_x > 0$) which triggers the vortex stretching. Upper and lower panels correspond to the upper and lower panels of the cross-sectional views in Fig.3.14 respectively. Thick lines represent contour lines defined as $u_x = 0$ and dash lines represent the plane of the cross-sectional views (a): before the turnover, (b): after the turnover.

of the local Lyapunov exponents and the Lyapunov modes give a hint that the growth of the streamwise vortices is exponential with time.

From these observations, the localization of the streamwise vortices is considered to be driven by the following mechanism;

stage I the small amplitude vorticities appear at the narrow region between the meandering streaks (see Fig.3.14 (a) and the appendix B.3 for detail),

stage II the small amplitude vorticities wind up and turn over the contour line of the streamwise velocity u_x, which forms the positive gradient region of the streamwise velocity; $\partial_x u_x > 0$ (see Fig.3.14 (b)),

stage III by vortex stretching, the small amplitude vorticities grow into the localized streamwise vortices (see Fig.3.14 (c-d)).

To describe the step II, we show the illustration of the formation mechanism of the positive gradient region of the streamwise velocity ($\partial_x u_x > 0$) in Fig.3.15, focusing on the narrow region between streaks at $(x, y, z) = (L_x/4, L_y/2, 0)$. Upper and lower panels correspond to the upper and lower panels of the cross-sectional views in Fig.3.14 respectively. Thick lines represent contour lines defined as $u_x = 0$ and dash lines represent the plane of the cross-sectional views (a): before the turnover, (b): after the turnover. Soon after the streak meandering, streamwise gradient of the the streamwise velocity is negative ($\partial_x u_x < 0$: see Fig.3.15 (a)) where the small amplitude vorticity appear. Therefore at this stage, the vortex stretching do not occur considering the streamwise component of the vorticity equation: $D_t \omega_x \sim (\partial_x u_x)\ \omega_x$[9]. However, the small amplitude vorticity winds up and turns over the contour line of the streamwise velocity u_x in a clockwise fashion in this case as the sign of the small amplitude vorticity is negative. Thus the positive gradient region of the streamwise velocity ($\partial_x u_x > 0$: see Fig.3.15 (b)) emerges, which triggers the vortex stretching. The localization of the positive vorticity occurs similarly around $(x, y, z) = (3L_x/4, 0, 0)$.

Corresponding to the occurrence of the vortex stretching, we can see a qualitative change also in the time series of 'horizontal' RMS of streamwise vorticity $\sqrt{\langle \omega_x^2 \rangle_H}$ at the mid-plane ($z = 0$). We put a blue circle on the time series shown in Fig.3.6 where the vortex stretching occurs ($t = 2750$). Obviously the qualitative change can be observed around the blue circle.

[9]We here drop the other terms including vortex tilting terms and viscous term for simplicity since our interest is in whether the vortex stretching occurs or not.

The vortex stretching described above appears to occur in most regeneration cycle. As a reference, we show another vortex stretching events following the event mentioned above in the appendix B.2.

By vortex stretching, the amplitude of the localized vortices grow up exponentially. Thus if we perturb the vortices, the perturbation also grow up exponentially. Hence, we can regard the localization process of the streamwise vorticities as some kind of a process driven by an exponential instability. This is the reason why there are some observations implying the relation between the localization of the streamwise vorticities and the orbital exponential instability; the time series of the local Lyapunov exponents shown in Fig.3.9, Fig3.10 (a) and the Lyapunov modes shown in Fig.3.13.

Apparently, the localized streamwise vortices wind up and break large-scale flow structure to small-scale one. Thus we calculate energy flux function and verify that the energy cascade coincides with the localization of the streamwise vortices (see for details in the appendix B.10).

3.5.2 Phase (ii); What regenerates the streaks?

As we see the previous section, the x-independent streaks mender because of the sinuous instability at the early stage of the regeneration cycle. However the x-independent streaks are generated again during the phase (ii), which closes the regeneration cycle. Here we discuss the regeneration mechanism of the x-independent streaks. We consider the regeneration process of the x-independent streaks as an energy gain process of the $\boldsymbol{k} = (0, 1)$ mode (hereafter referred to as 'streak mode' $\boldsymbol{k}_s = (0, 1)$ and written by $\hat{\boldsymbol{u}}(\boldsymbol{k}_s)$) whose amplitude increases in the phase (ii) shown in the time series of the modal RMS velocities (Fig.3.4).

An evolution equation of 'modal energy'[10]of the $\boldsymbol{k}$ mode is generally

$$\begin{aligned}\frac{d}{dt}\left\langle |\hat{\boldsymbol{u}}(\boldsymbol{k})|^2 \right\rangle_z &= -\left\langle 2Re\left[\hat{\boldsymbol{u}}^*(\boldsymbol{k}) \cdot \left(\hat{u}_z(\boldsymbol{k})\partial_z\right)\hat{\boldsymbol{u}}(\boldsymbol{0})\right] \right\rangle_z \\ &\quad - \left\langle \sum_{\substack{\boldsymbol{k}''+\boldsymbol{k}'=\boldsymbol{k}, \\ \boldsymbol{k}'\neq\boldsymbol{0},\boldsymbol{k}''\neq\boldsymbol{0}}} \mathcal{N}(\hat{\boldsymbol{u}}(\boldsymbol{k}), \hat{\boldsymbol{u}}(\boldsymbol{k}'), \hat{\boldsymbol{u}}(\boldsymbol{k}'')) \right\rangle_z \\ &\quad - \frac{2}{Re}\left\langle \left\{(\alpha k)^2 + (\beta l)^2\right\}|\hat{\boldsymbol{u}}(\boldsymbol{k})|^2 + |\partial_z\hat{\boldsymbol{u}}(\boldsymbol{k})|^2 \right\rangle_z, \end{aligned} \tag{3.16}$$

[10]More precisely, it would be better to refer to it as 'twice of modal energy'.

(see appendix B.5 for a detailed derivation)[11].The first term of the r.h.s. of the above equation is an nonlinear interaction term with the mean flow, the second term is a summation of the other nonlinear terms (triad interaction $\boldsymbol{k}_s = \boldsymbol{k}' + \boldsymbol{k}''$ with $\boldsymbol{k}', \boldsymbol{k}''$ modes except the mean flow mode; $\boldsymbol{k}' \neq \boldsymbol{0}, \boldsymbol{k}'' \neq \boldsymbol{0}$), and the third term is the viscous dissipation term. The nonlinear interaction term with the mean flow can be approximated by

$$\left\langle 2Re\Big[\hat{\boldsymbol{u}}^*(\boldsymbol{k}) \cdot \big(\hat{u}_z(\boldsymbol{k})\partial_z\big)\hat{\boldsymbol{u}}(\boldsymbol{0})\Big]\right\rangle_z \simeq \left\langle 2Re[\hat{u}_x^*(\boldsymbol{k})\hat{u}_z(\boldsymbol{k})\partial_z\hat{u}_x(\boldsymbol{0})]\right\rangle_z \tag{3.17}$$

with an assumption about the mean flow: $\partial_z\hat{u}_x(\boldsymbol{0}) \gg \partial_z\hat{u}_y(\boldsymbol{0})$ (see appendix B.5.2 for a validity of the mean flow assumption). For simplicity, we refer to the approximated term as "the nonlinear interaction term with the mean flow" hereafter.

In order to study the energy gain process of the streak mode, we show a result of budget analysis of the evolution equation of streak mode 'energy' ($\boldsymbol{k} = \boldsymbol{k}_s$ in the evolution equation (3.16)) in Fig.3.16. The red (solid) line is the time derivative term of $\langle|\hat{\boldsymbol{u}}(\boldsymbol{k}_s)|^2\rangle_z$ (l.h.s. of the evolution equation), the green (dashed) line is the nonlinear interaction term with the mean flow, the blue (dot) line is the other nonlinear terms, and the pink (dashed-dot) line is the viscous dissipation term, where the other nonlinear terms is calculated from the other three terms. The time derivative of $\langle|\hat{\boldsymbol{u}}(\boldsymbol{k}_s)|^2\rangle_z$ is negative in the phase (i) and positive in the phase (ii), which correspond to the meandering and regeneration of the streaks. Furthermore It is found that an energy input term to the streak mode (i.e. the positive term in the r.h.s. of the evolution equation) is only the mean flow interaction term throughout the regeneration cycle. Thus we conclude that the regeneration of the streaks is driven by the mean flow interaction.

[11]Using horizontal direction Fourier expansion: $f(\boldsymbol{x}) = \sum_{\boldsymbol{k}} \hat{f}(\boldsymbol{k}.z)e^{i\boldsymbol{k}\cdot\boldsymbol{x}}$, square of the L^2 norm of the function f is

$$\begin{aligned}
||f(x,y,z)||_{L_2}^2 &= \frac{1}{2L_xL_y}\int_{z=-1}^{z=+1}\int_{y=0}^{y=L_y}\int_{x=0}^{x=L_x} f(x,y,z)^2 dxdydz \\
&= \frac{1}{2}\int_{z=-1}^{z=+1}\sum_{\boldsymbol{k}}|\hat{f}(\boldsymbol{k},z)|^2 dz \\
&= \langle\sum_{\boldsymbol{k}}|\hat{f}(\boldsymbol{k},z)|^2\rangle_z.
\end{aligned}$$

Here we consider $\langle|\hat{\boldsymbol{u}}(\boldsymbol{k})|^2\rangle_z = ||\boldsymbol{u}^{\boldsymbol{k}}(\boldsymbol{x})||_{L_2}^2$, where $\boldsymbol{u}^{\boldsymbol{k}}(\boldsymbol{x})$ is velocity field consisting of $\boldsymbol{k}$ mode only.

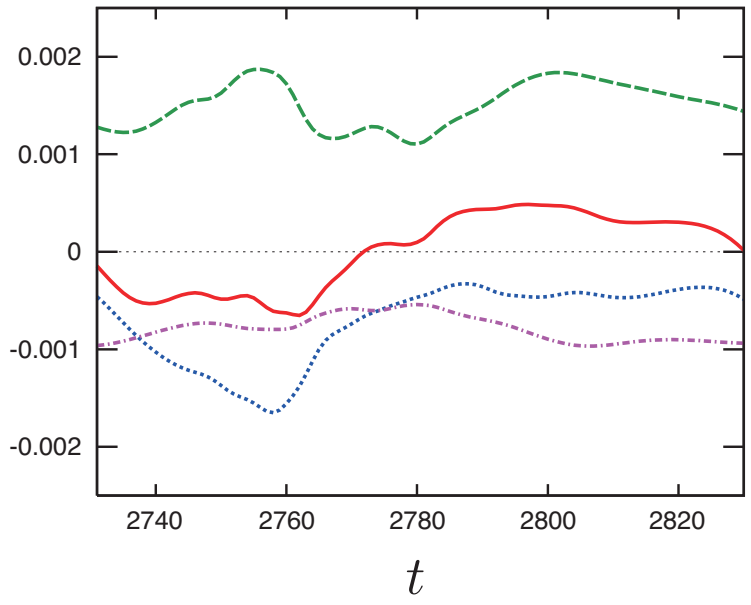

Fig. 3.16: Budget analysis of the evolution equation of the 'modal energy' (3.16) in the case of the streak mode (i.e. $\boldsymbol{k} = \boldsymbol{k}_s$). The red (solid) line is the time derivative term (l.h.s. of the evolution equation), the green (dashed) line is the nonlinear interaction term with the mean flow, the blue (dot) line is the other nonlinear terms, and the pink (dashed-dot) line is the viscous dissipation term.

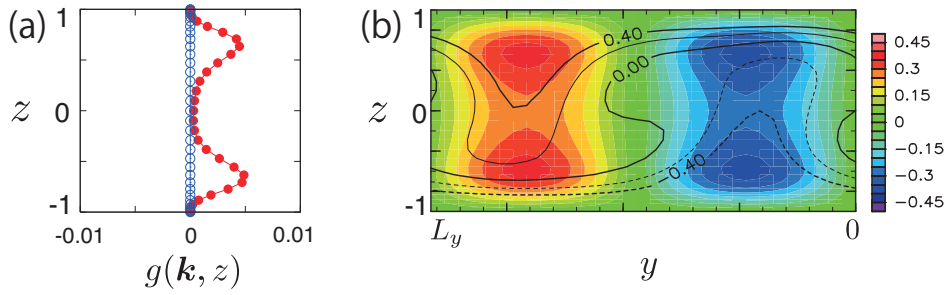

Fig. 3.17: (a) Wall-normal profile of the mean flow interaction term of the streak mode; $g(\boldsymbol{k}_s, z) = -2Re[\hat{u}_x^*(\boldsymbol{k}_s)\hat{u}_z(\boldsymbol{k}_s)\partial_z\hat{u}_x(\boldsymbol{0})]$ (red line with closed circles) and the meandering mode; $g(\boldsymbol{k}_m, z) = -2Re[\hat{u}_x^*(\boldsymbol{k}_m)\hat{u}_z(\boldsymbol{k}_m)\partial_z\hat{u}_x(\boldsymbol{0})]$ (blue line with open circles) at $t = 2800$. (b) The cross-sectional view of the streamwise velocity field consisting of the streak mode only; $u_x^{\boldsymbol{k}_s}(y, z)$ (color tone) and that consisting of the all modes (solid lines) at $t = 2820$.

Wall-normal profiles of the mean flow interaction term are also consistent with those of streak mode. Fig.3.17 (a) shows the wall-normal direction profiles of the mean flow interaction term of the streak mode; $g(\boldsymbol{k}_s, z) = -2Re[\hat{u}_x^*(\boldsymbol{k}_s)\hat{u}_z(\boldsymbol{k}_s)\partial_z\hat{u}_x(\boldsymbol{0})]$ at $t = 2800$ (red line with closed circles). The profile is almost the same throughout the regeneration cycle (see appendix B.2) and $g(\boldsymbol{k}_s, z) > 0$, indicating the energy injection from the mean flow to the streak mode throughout the regeneration cycle. Fig.3.17 (b) shows the cross-sectional view of the streamwise velocity field consisting of the streak mode only; $u_x^{\boldsymbol{k}_s}(y, z)$ at $t = 2820$ (color tone). The solid lines in Fig.3.17 (b) are the contour lines of the streamwise velocity field consisting of the all modes. It is found that the wall-normal direction profile of the streak mode amplitude has two local maxima at $z \simeq \pm 0.6$, which is similar to that of the mean flow interaction term. This observation also supports our conclusion that the regeneration of the streaks is driven by the mean flow interaction.

In Fig.3.17 (a), we also show the wall-normal direction profiles of the mean flow interaction term of the $\boldsymbol{k} = (1, 0)$ mode (hereafter referred to as 'meandering mode' $\boldsymbol{k}_m = (1, 0)$); $g(\boldsymbol{k}_m, z) = -2Re[\hat{u}_x^*(\boldsymbol{k}_m)\hat{u}_z(\boldsymbol{k}_m)\partial_z\hat{u}_x(\boldsymbol{0})]$ at $t = 2800$ (blue line with open circles). Clearly $g(\boldsymbol{k}_m, z) \simeq 0$ and this holds throughout the regeneration cycle (see appendix B.2). Therefore it is found that the energy of the mean flow is injected not to the meandering mode but

to the streak mode throughout the regeneration cycle[12].

The mean flow interaction term can be interpreted as a tilting of the spanwise vorticity of the mean flow to wall-normal vorticity. This physical interpretation of the mean flow interaction term and a relation between this mechanism and the well-known lift-up mechanism is discussed in appendix B.6.

3.5.3 Energy flows in the regeneration cycle; Which interaction does control the cycle?

Finally, here we summarize the regeneration mechanisms illustrated above by examining energy flows. Fig.3.16 shows that the mean flow interaction creates the regeneration of the streaks. However, while the mean flow interaction term and the energy dissipation term do not change drastically throughout the cycle, the other nonlinear terms change their amplitude with the shift from phase (i) to phase (ii); the summation of the other nonlinear terms reach a minimum ($\simeq -0.0015$) in the phase (i) and maintain a constant value ($\simeq -0.0005$) in the phase (ii). Thus, it appears that the other nonlinear interaction terms control the sign of the time derivative of $\langle|\hat{\boldsymbol{u}}(\boldsymbol{k}_s)|^2\rangle_z$; the meandering and regeneration of the streaks (i.e. the regeneration cycle).

When the other nonlinear interaction terms are active (phase (i)) the energy appears to "leak" from the streak mode, and when the other nonlinear terms are inactive (phase (ii)) the energy appears to "accumulate" in streak mode, which leads to the next final question: which interaction in the nonlinear terms does control the regeneration cycle?

At the initial stage of the phase (i), the amplitude of the streak mode decreases and the amplitude of the meandering mode increases. This observation implies that the "accumulated" energy "leaks" from the streak mode to the meandering mode through the nonlinear interaction during the phase (i). Therefore we focus our attention on the evolution equation of the streak mode 'energy', particularly writing the nonlinear interaction between the

[12]This is because the streamwise and wall-normal velocity components of the meandering mode are quite small (when compared to those of the streak mode).

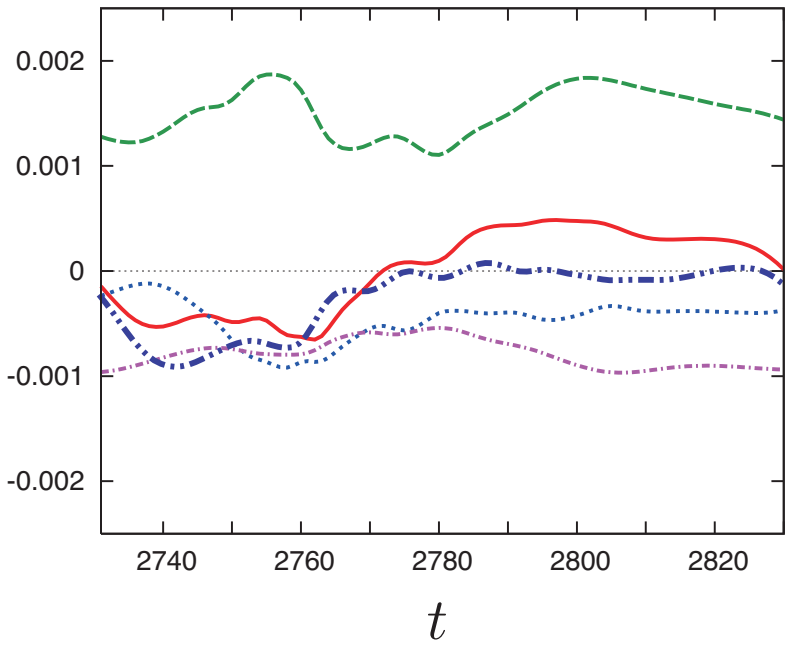

Fig. 3.18: Budget analysis of the evolution equation of the streak mode 'energy' Eq. (3.18). The red (solid) line, the green (dashed) line, and the pink (dashed-dot) line is the same as in Fig.3.16. The blue (dot) line is the other nonlinear terms and the navy (dashed double-dotted) line is the nonlinear interaction terms with the meandering mode in the Eq. (3.18).

streak mode $\boldsymbol{k}_s$ and the meandering mode $\boldsymbol{k}_m$ explicitly;

$$
\begin{aligned}
\frac{d}{dt}\left\langle |\hat{\boldsymbol{u}}(\boldsymbol{k}_s)|^2 \right\rangle_z =& -\left\langle 2Re\Big[\hat{\boldsymbol{u}}^*(\boldsymbol{k}_s)\cdot\big(\hat{u}_z(\boldsymbol{k}_s)\partial_z\big)\hat{\boldsymbol{u}}(\boldsymbol{0})\Big]\right\rangle_z \\
&-\left\langle 2Re\Big[\hat{\boldsymbol{u}}^*(\boldsymbol{k}_s)\cdot(i\alpha\hat{u}_x(\boldsymbol{k}_{ob-})+\hat{u}_z(\boldsymbol{k}_{ob-})\partial_z)\hat{\boldsymbol{u}}(\boldsymbol{k}_m)\Big]\right\rangle_z \\
&-\left\langle 2Re\Big[\hat{\boldsymbol{u}}^*(\boldsymbol{k}_s)\cdot\big(-i\alpha\hat{u}_x(\boldsymbol{k}_m)+i\beta\hat{u}_y(\boldsymbol{k}_m)+\hat{u}_z(\boldsymbol{k}_m)\partial_z\big)\hat{\boldsymbol{u}}(\boldsymbol{k}_{ob-})\Big]\right\rangle_z \\
&-\left\langle 2Re\big[\hat{\boldsymbol{u}}^*(\boldsymbol{k}_s)\cdot\big(-i\alpha\hat{u}_x(\boldsymbol{k}_{ob+})+\hat{u}_z(\boldsymbol{k}_{ob+})\partial_z\big)\hat{\boldsymbol{u}}^*(\boldsymbol{k}_m)\big]\right\rangle_z \\
&-\left\langle 2Re\big[\hat{\boldsymbol{u}}^*(\boldsymbol{k}_s)\cdot\big(i\alpha\hat{u}_x^*(\boldsymbol{k}_m)+i\beta\hat{u}_y^*(\boldsymbol{k}_m)+\hat{u}_z^*(\boldsymbol{k}_m)\partial_z\big)\hat{\boldsymbol{u}}(\boldsymbol{k}_{ob+})\big]\right\rangle_z \\
&-\left\langle \sum_{\substack{\boldsymbol{k}''+\boldsymbol{k}'=\boldsymbol{k}_s,\\ \boldsymbol{k}'\neq\boldsymbol{0},\boldsymbol{k}''\neq\boldsymbol{0}\\ \boldsymbol{k}'\neq\pm\boldsymbol{k}_m,\boldsymbol{k}''\neq\pm\boldsymbol{k}_m,}} \mathcal{N}'(\hat{\boldsymbol{u}}(\boldsymbol{k}_s),\hat{\boldsymbol{u}}(\boldsymbol{k}'),\hat{\boldsymbol{u}}(\boldsymbol{k}''))\right\rangle_z \\
&-\frac{2}{Re}\left\langle \beta^2|\hat{\boldsymbol{u}}(\boldsymbol{k}_s)|^2+|\partial_z\hat{\boldsymbol{u}}(\boldsymbol{k}_s)|^2\right\rangle_z \qquad (3.18)
\end{aligned}
$$

where $\boldsymbol{k}_{ob+}=(1,1)$ and $\boldsymbol{k}_{ob-}=(-1,1)$ which close the triad interaction; $\boldsymbol{k}_s=\boldsymbol{k}'+\boldsymbol{k}''$ (see appendix B.5.3 for a detailed derivation). Differences between the above equation and the equation (3.16) are the 2nd–5th terms in the r.h.s. of the above equation which are extracted from the other nonlinear terms in the equation (3.16). We refer to the 2nd–5th terms as "the (nonlinear) interaction terms with the meandering mode".

In Fig.3.18, the blue (dot) line is the other nonlinear terms and the navy (dashed double-dotted) line is the nonlinear interaction terms with the meandering mode in Eq.(3.18). The red, green, and pink lines are the same as those in the Fig.3.16. It is found that the interaction terms with the meandering mode is negative ($\simeq -0.001$) during the phase (i) and almost zero during the phase (ii), while the other nonlinear terms in Eq.(3.18) do not exhibit a drastic change throughout the cycle. Only in the Phase (i) the interaction term with meandering mode is working, which makes the time derivative of $\langle|\hat{\boldsymbol{u}}(\boldsymbol{k}_s)|^2\rangle_z$ be negative (i.e. decrease of the amplitude of the streak mode.) only in the Phase (i). Hence, we can interpret this observation as meaning that when the interaction between the streak mode and the meandering mode is "active" (the phase(i)) the energy leaks from the streak mode and when the interaction is "inactive" (the phase(ii)) the energy accumulates in

the streak mode. Therefore, we could conclude that the interaction between the streak mode and the meandering mode control the cycle.

3.6 Discussions and Conclusions

In this chapter, we characterized the regeneration cycle in the minimal Couette turbulence with the orbital instability. The orbital instability was studied by using the covariant Lyapunov analysis, which is a step toward understanding of turbulence on the basis of the full Navier-Stokes equation without modelings and phenomenological arguments. Our goal of this chapter was to tackle 'linear stability analysis' of the *full* regeneration cycle.

In §3.2, we described the problem settings, equations of motion (formulation by using toroidal and poloidal potentials), and numerical methods for time-integration and covariant Lyapunov analysis.

The results of the time-integrations are shown in §3.3, where we observed the regeneration cycle as reported by the previous studies [59]. Particularly, we focused our attention on the localization of the streamwise vortices and observed the strong and sharp localization in the time series of RMS of the vorticity. There, we divided roughly the regeneration cycle into two phases, i.e. phase (i) is the streak meandering period and phase (ii) is the streak reformation period.

In §3.4, we presented the main results of this chapter: the orbital instability of the regeneration cycle in the Couette turbulence. First, Lyapunov spectrum was shown, which produces the following results:
The maximum Lyapunov exponent λ_1.— The maximum Lyapunov exponent is $\lambda_1 = 0.021$, which appears to be the reciprocal of the half 'period' of the regeneration cycle. Interestingly, the value of λ_1 is close to the maximum Floquet exponent ($\mu = 0.019$) of the strong UPO reported by Kawahara [69]. As mentioned before, Kawahara and Kida [25] showed that the statistics of the minimal Couette turbulence can be approximated well by the strong UPO. Saiki and Yamada [28, 74] studied the relation between the statistics on the segments of the chaotic orbits and that on the UPOs numerically. Remarkably, they found that UPO whose Floquet exponent is close to the Lyapunov exponent of the chaotic attractor gives a good approximation to the statistics of the chaotic attractor (see Fig.2 in [74])[13]. Taking into account their results,

[13]They described this result as follows; "if we choose a special UPO whose Lyapunov exponent approximates that of a long chaotic orbit, the UPO also gives various macroscopic statistical quantities of chaos, even if the period is not large enough."

it would be natural to conclude that the strong UPO can approximate the statistics of the minimal Couette turbulence, *since* the Floquet exponent of it is close to the maximum Lyapunov exponent of the turbulence. In addition, the value of λ_1 is close to the that of the Flpquet exponents of the unstable (relative) periodic solutions obtained by Viswanath [70]. Nikitin [35] studied the maximum Lyapunov exponent of developed wall-turbulence in a circular tube and a plane channel. They found that the maximum Lyapunov exponent normalized by the wall time scale was estimated to be a constant value ($\lambda_N^+ \approx 0.021$) which is independent on the Reynolds number in the range of $4000 \leq Re \leq 10700$ ($140 \leq Re_\tau \leq 320$) and type of the boundary shape. In the case of the minimal Couette turbulence studied here, the maximum Lyapunov exponent normalized by the wall time scale[14]is $\lambda_1^+ \approx 0.007$ which is about one third of the exponent λ_N^+ found by Nikitin. It is considered that the large difference in the Reynolds number causes this discrepancy between the exponent of the minimal Couette turbulence and that of the developed wall-turbulence. Therefore we expect that the exponent $\lambda_1^+(Re, L_x, L_y)$ increases with the parameters such as Reynolds number or system sizes from the parameters of the minimal flows and asymptotically attains to the constant value $\lambda_N^+ \approx 0.021$ (for instance, $\lim_{Re\to\infty} \lambda_1^+(Re) = \lambda_N^+$).

Dimension of the unstable manifold.— Dimension of the unstable manifold of the attractor is the number of positive Lyapunov exponents. In the case of the minimal Couette flow, the dimension is four, since we observed four positive Lyapunov exponents. On the other hand, the strong UPO has one real and a complex conjugate pair of unstable Floquet multipliers [69], which means dimension of the unstable manifold of the strong UPO is three. While the strong UPO approximates the statistics of the turbulence well, the turbulent attractor itself may possess the other unstable direction (instability) which cannot be captured by the strong UPO only.

Dimension of the attractor.— Dimension of the turbulent attractor was calculated as $D_L \simeq 14.8$ by using Kaplan-Yorke formula[15]. This is why the low-dimensional models can reproduce the behaviors like the regeneration cycle. The attractor dimension of the turbulent Poiseuille flow was estimated

[14]The wall time scale t_τ is $t_\tau = l_\tau/u_\tau = Re/Re_\tau^2 = 0.346$ ($Re = 400, Re_\tau = 34$). Thus, the maximum Lyapunov exponent normalized by the wall time scale is $\lambda_1^+ = \lambda_1 t_\tau \approx 0.007$.

[15]Yang *et al.* [42] conjectured that the dimension of the inertial manifold D_{IM} is related to the number of 'physical modes' which is almost twice the Lyapunov dimension D_L (i.e. $D_{IM} \sim 2D_L$). Employing this formula directly without consideration of the existence of such manifold, the dimension of the inertial manifold of the minimal Couette turbulence is estimated as $D_{IM} \sim 30$.

as $D_L \simeq 780$ at the (not so high) Reynolds number $Re = 3200$ ($Re_\tau = 80$), therefore the attractor dimension of the wall turbulence is expected to increase drastically with the Reynolds number.
Kolmogorov-Sinai entropy.— Kolmogorov-Sinai entropy was calculated by the sum of the positive Lyapunov exponents (Pesin entropy formula).

Secondly, we characterized the regeneration cycle with the local Lyapunov exponents. Roughly speaking, the local Lyapunov exponents become positive at the initial stage of the phase (i) and attain their maxima at the moment when the phase shifts to (ii) from (i). After attaining their maxima, the Lyapunov exponents suddenly decrease and become negative during the phase (ii). This characterization was supported by observing the accumulative expanding rate $\Lambda(t_0, \tau)$, which indicated that if we put the perturbation at the initial stage of the phase (i), then the perturbation grows exponentially until the peak of the localization of the streamwise vortices. Moreover, it indicated that if we put the perturbation at the final stage of the phase (i), then the perturbation never grows and decays during the phase (ii). These results obtained here suggest that the localization of the streamwise vortices controls the instability of the whole of the regeneration cycle.

Finally, the Lyapunov modes associated with the Lyapunov exponents were shown, which also support the results described above. Namely, we observed the sinuous instability mode at the *initial* stage of the phase (i), and we observed the streamwise vortices instability mode at the *final* stage of the phase (i). At the initial stage of the phase (i), the streaks are dominant structures in the flows. Therefore, the sinuous instability mode can be interpreted as the unstable mode of the streaks. In the previous studies, it was suggested that the most unstable mode of the streaks is the sinuous mode [71, 72]. However, these studies employed the linear stability analyses of the streak *models* considered as *steady* solutions. We here showed that the sinuous instability mode is actually the unstable mode of the streaks in the turbulent flows. Since all 'history' of the successive regeneration cycles are reflected in the results of the Lyapunov analysis by definition, thus the sinuous mode captured by the Lyapunov analysis is unstable globally in time rather than locally in time. Moreover, the growth rate (i.e. local Lyapunov exponent) of the sinuous mode is smaller than that of the instability mode associated with the streamwise vortices. Therefore, the instability mode associated with the streamwise vortices is more important as regarding the instability of the whole of the regeneration cycle.

Hamilton *et al.* [59] and Waleffe [62] proposed the self-sustaining mechanisms consisting of streak instability, regeneration of the streamwise vor-

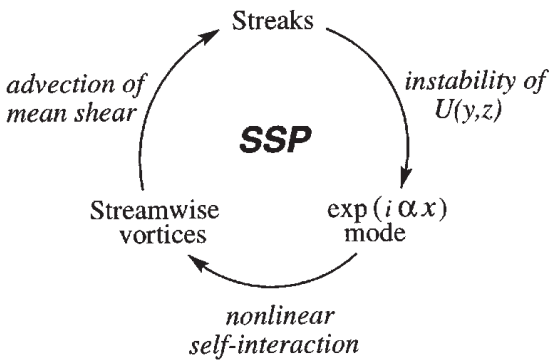

Fig. 3.19: Conceptual diagram of self-sustaining process (SSP) shown in Fig.1 of Waleffe [62].

tices, and formation of the streaks (Fig.3.19), by *modeling* the streaks and the streamwise vortices. In §3.5, we discussed the regeneration cycle from the different point of view from the previous studies [59, 62]. Three questions about the mechanisms composing the cycle were addressed there: How do the streaks mender and the streamwise vortices appear? What regenerates the streaks? Which interaction does control the cycle? Here, we summarize our answers to these questions.

In §3.5.1, we considered the first question: How do the streaks mender and the streamwise vortices appear? As mentioned above, the meandering of the streaks are caused by sinuous instability, which is verified by the previous studies [71, 72] and the covariant Lyapunov analysis. On the localization mechanisms of the streamwise vortices, we divided the mechanisms into three stages and described the stage II, III in detail (the stage I is argued in the appendix B.3). There, the small amplitude vorticities form the region $\partial_x u_x > 0$ (stage II), which trigger the vortex stretching there (stage III). As a result of the vortex stretching, the localized large amplitude vortices appear. This generating mechanism of the streamwise vortices are consistent with the time series of the 'horizontal' RMS of the streamwise vortices. Furthermore, the stretching process is considered to intensify the amplitude of the vortices exponentially, which is also consistent with the results of the covariant Lyapunov analysis.

The second question — What regenerates the streaks? — was discussed in §3.5.2. The energy gaining process of the $\boldsymbol{k} = \boldsymbol{k}_s = (0, 1)$ mode can be

interpreted as the regeneration process of the streaks. Therefore, we derived the evolution equation of the model 'energy' Eq. (3.16) and performed budget analysis, by which we obtained the following results;

- During the regeneration cycle, energy coming from the mean flows *only* runs into streak mode ($\boldsymbol{k}_s = (0, 1)$) almost constantly, not into the meandering mode at all ($\boldsymbol{k}_m = (1, 0)$).

- During the regeneration cycle, energy dissipation rate is almost constant.

- In the phase (i), the other nonlinear terms decrease the streak modal energy ($\boldsymbol{k}_s = (0, 1)$) considerably.

Thus, the answer to the above question is that the mean flow interaction regenerates the streaks. Physical interpretation of this interaction is argued in the appendix B.6.

The above budget analysis implies that the increase and decrease of the streak modal energy (i.e. the regeneration cycle) is governed by the other nonlinear interactions. In more detail, we asked 'which interaction does control the cycle?'. This is the final question in this chapter. In §3.5.3, we found out that the interaction terms between the streak mode ($\boldsymbol{k}_s = (0, 1)$) and the meandering mode ($\boldsymbol{k}_m = (1, 0)$) control the cycle. These interaction terms can be considered to play a role as a 'valve' of the energy flows in the system, i.e. the energy leaks from the streak mode when the interaction is active (the valve is open in the phase (i)), the energy accumulate in the streak mode when the interaction is inactive (the valve is closed in the phase (ii)).

We illustrate energy flows in the system in a conceptual diagram Fig.3.20 (i) for the phase (i) and (ii) for the phase (ii). The horizontal black lines represent walls. Energy is injected from the walls into the mean flows directly (red arrows). The energy flows into the streak mode ('streaks' in the diagram) not into the meandering mode ('$e^{i\alpha x}$ mode' in the diagram) at all (green arrows). In the phase (ii) (Fig.3.20 (ii)), the energy accumulates in the streak mode and the amplitude of it increases with time[16]. Eventually, the streaks become unstable if the amplitude exceeds a certain threshold (the sinuous instability), which sifts the phase from (ii) to (i). In the phase (i) (Fig.3.20 (i)), the energy of the streak mode leaks into the meandering mode

[16]We here draw only the dominant energy flows in the system. Therefore, we skip to draw the relatively small and constant flows such as the energy dissipation.

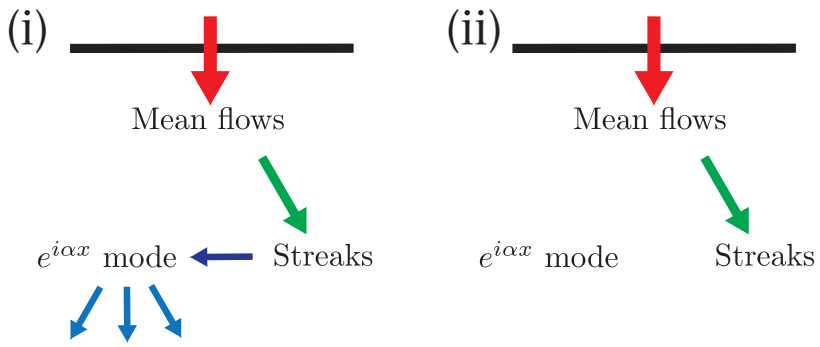

Fig. 3.20: Conceptual diagram of the energy flows in the regeneration cycle for (i); the phase (i) and for (ii); the phase (ii). In the diagrams, 'Mean flows' denotes $\boldsymbol{k} = (0, 0)$ mode, 'Streaks' denotes streak mode ($\boldsymbol{k} = (0, 1)$), and '$e^{i\alpha x}$ mode' denotes meandering mode ($\boldsymbol{k} = (1, 0)$).

(navy arrow). As we see in the appendix B.10, the energy cascades to the higher wavenumber mode (blue arrow) in the phase (i). From the viewpoint of the orbital instability, the sinuous mode activates the interaction between the streak and the meandering modes (i.e. opens the 'valve', navy arrow), which results in the localization of the streamwise vortices. The streamwise vortices grows exponentially, which stretches and breaks the large scale flow structure into small one (the energy cascade). After the energy cascade, the interaction between the streak and the meandering modes become inactive (i.e. the 'valve' is closed), which returns the state of the system to the starting point of the regeneration cycle.

The picture of the regeneration cycle described here is somewhat different from the prevailing notion, i.e. self-sustaining process [59, 62] (Fig.3.19). While the instability mechanism of the streaks is the same (sinuous instability), the other mechanisms are not. For instance, in the self-sustaining process [59, 62], the advection of the mean shear regenerates the streaks at the *final period of the cycle only* (Fig.3.19). However, as shown in the budget analysis (Fig.3.16) and the conceptual diagram (Fig.3.20), we showed that the tilting of the mean vorticity keeps to generate the streaks *throughout the cycle* and the interaction between the streak and the meandering modes controls whether the streaks are actually regenerated or not. Therefore, we conclude that the picture described here provides a novel (or modified) per-

spective of the regeneration cycle.

Chapter 4

Conclusions and future issues

Conclusions.— In this thesis, we considered fluid turbulence from the viewpoint of the dynamical system theory. Toward understanding of turbulence from this viewpoint, many researchers have found a number of invariant solutions of the Navier-Stokes equations numerically whose significance has been recognized in recent years [29]. Another important property of chaos is the orbital instability. Here we focused our attention on the orbital instability of turbulence, particularly that of the Kolmogorov flow and the Couette turbulence. Kolmogorov flow is fluid flow on the two-dimensional torus governed by the Navier-Stokes equation and its bifurcation and stability have been under intense study. The Couette turbulence is fluid turbulence between moving walls governed by the three-dimensional Navier-Stokes equation and has been studied with interests in the problems such as the transition to turbulence and the turbulent structures.

In §2, we studied the relations between the hyperbolic properties and the physical properties of the chaotic Kolmogorov flow. Since the hyperbolicity is one of fundamental properties of dynamical systems, Inubushi *et al.* [52] studied the hyperbolicity of the chaotic Kolmogorov flow and observed the hyperbolic-nonhyperbolic transition (in §IV. of [52]) employing the covariant Lyapunov analysis (Fig.2.6). Here, we examined the correlation functions and enstrophy (energy dissipation rate) as a physical properties. First, we studied the correlation decay of vorticity for several Reynolds numbers across the hyperbolic-nonhyperbolic transition point. As a result, we found that the hyperbolic-nonhyperbolic transition is reflected in the qualitative change of the long-time correlation functions (Fig.2.7, 2.8). Futhermore, we reported that the angle between the stable and unstable manifolds θ is relevant to the enstrophy (energy dissipation rate) (Fig.2.12).

In §3, we studied the regeneration cycle observed in the various type of wall-turbulence. Particularly, the goal of this chapter was to characterize the regeneration cycle in the minimal Couette turbulence with the orbital instability, employing the covariant Lyapunov analysis. First, we presented the Lyapunov spectrum (Fig.3.7). There, we obtained the maximum Lyapunov exponent, the dimension of the unstable manifold, the dimension of the attractor (Fig.3.8), and the Kolmogorov-Sinai entropy. Then, we compared these information on the attractor with the results reported by previous studies such as the Floquet exponents of (relative) UPOs [69, 70], the normalized maximum Lyapunov exponent of the wall-turbulence at the high Reynolds number [35], the low-dimensional models [62], and the attractor dimension of the Poiseuille turbulence [34].

To see the orbital instability of the regeneration cycle in more detail, we studied the local Lyapunov exponents (Fig.3.9, 3.10) and the associated Lyapunov mode (Fig.3.11, 3.12,3.13). These quantities indicated mainly that

- the streak instability originates from the sinuous mode which induces streaks to meander,
- the most unstable instability during the regeneration cycle is the instability associated with the localization of the streamwise vortices rather than the sinuous instability,
- Instabilities are found only in a very early stage of the cycle (phase (i)) and after that, there are no exponential instability at all (phase (ii)).

Here we make some comments on the above results. Although the sinuous instability has been pointed out by the previous studies [71, 72], they examined linear stability analyses of streak *models* which is not solution of the Navier-Stokes equations. On the other hand, the covariant Lyapunov analysis applied to the Navier-Stokes equation extracted the sinuous instability as the unstable mode of the streaks in the *actual* turbulence. Since all "history" of the successive regeneration cycles are reflected in the results of the Lyapunov analysis by definition, thus the sinuous mode is unstable globally in time rather than locally in time. Furthermore, the local Lyapunov exponent of the sinuous mode is smaller than that of the instability mode associated with the streamwise vortices localization. Therefore, the instability induced by the streamwise vortices is more important than the sinuous one as regarding the instability of the whole of the regeneration cycle. Final comment on the above results is that the minimal turbulence evolves

over time without any (exponential) instability during more than half[1] of the cycle (the phase (ii)). In other words, it was found that the instabilities is distributed "inhomogeneously" on the regeneration cycle. The regeneration cycle in wall-turbulence is important not only for science but also for engineering, thus there are a great deal of research on the regeneration cycle. However, as far as we know, the orbital instability picture of the cycle described above has been never proposed. Moreover, it may become one of important keys to untangle the problems of wall-turbulence such as relations between the regeneration cycle and its statistics.

In the final part of §3, we reconsidered the regeneration cycle from the viewpoint of the orbital instability. There, we argued the mechanism of the streak meandering and the localization of the streamwise vortices (phase (i), Fig.3.14, Fig.3.15) and the mechanism of the streak reformation (phase (ii), Fig.3.16, Fig.3.17). Besides these arguments, we studied the energy flows in the system during the regeneration cycle in detail and detected the interaction between the streak mode ($\boldsymbol{k}_s = (0, 1)$) and the meandering mode ($\boldsymbol{k}_m = (1, 0)$) that controls the regeneration cycle: the energy leaks from the streak mode when the interaction is "active" (the phase (i)), the energy accumulate in the streak mode when the interaction is "inactive" (the phase (ii)). Finally, we proposed the conceptual diagram (Fig.3.20) of the energy flows in the system during the regeneration cycle.

Future issues.— Finally, we address future issues briefly.

As regards the Kolmogorov flows, it remains open issues whether the results obtained here hold in general or not. Particularly, the issues are whether the hyperbolic-nonhyperbolic transition (as observed in the Lorenz system [48] and the the coupled Ginzburg-Landau equations [50]) occurs in another fluid system, which is independent of the problem settings such as the form of the external forcing, the aspect ratio of the system, the boundary condition, and so on. It is natural to ask if the relation between the hyperbolic and physical properties holds at the case of another fluid system. Also, it is expected to explain the reason why the hyperbolic properties are related to the physical properties. More important goal is to know if attractor of the fully developed turbulence is hyperbolic or not and its hyperbolic property is related to the physical properties such as the intermittent energy dissipation of isotropic homogeneous turbulence and the wall friction drag of wall-turbulence.

[1] About 70 % of the "period" T_p of the regeneration cycle ($T_p \simeq 100$).

As regards the Couette turbulence, we expect the orbital instability found in the minimal Couette turbulence to be a common characteristic of the regeneration cycle in the various wall-turbulence at medium Reynolds number. Future issues on this topic are as follows: How do the properties of the orbital instability of the cycle change with increasing Reynolds number or system size? Is it possible to characterize the robust layer in the velocity profiles such as viscous, buffer, and logarithmic layer (Prandtl's wall law) with Lyapunov modes in a statistical way[2]? How are the properties of the orbital instability related to the statistics? In this thesis, we can study only the regeneration cycle. However, as well as the cycle, so-called *bursting* event also occurs infrequently in wall-turbulence and is considered as an important phenomenon [21, 47, 77]. Hence, it is a challenging to characterize the bursting event from the standpoint of the orbital instability and clarify the bursting mechanism. For instance, Kobayashi and Yamada [57] studied intermittency in the GOY shell model and they characterized the bursting phenomenon in the GOY shell model with stable and unstable manifold structures via covariat Lyapunov analysis. Although there would be an essential difference between the bursting phenomenon in wall-turbulence and that in the GOY model, it is intriguing to study the bursting phenomenon in wall-turbulence in terms of changes in such manifold structures.

There are many open problems in physics of turbulence which is expected to be understood on the basis of the full Navier-Stokes equations [1, 2]. For instance, it is natural to ask how turbulent motion produces the 'generic' statistical laws, how we calculate *eddy viscosity*, and how intermittent behaviors occur in turbulence. Will it become possible to give answers to these questions with employing the dynamical system theory?[3] If we can obtain clear answers to the above questions, then we are able to say that the dynamical system theory is useful to understand turbulence.

[2]Karimi and Paul [33] showed statistically that a transition from 'boundary-dominated' dynamics to 'bulk-dominated' dynamics occurs as the system size is increased in the Rayleigh-Bénard convection with the Lyapunov vector associated with the largest Lyapunov exponent.

[3]It would be possible to obtain some answer by examining Ruelle's prediction on the shape of the Lyapunov spectrum near $\lambda_j \sim 0$ and Constantin-Foias-Temam's prediction on its asymptotic shape $j \to \infty$ (one of the pioneer works was done by Keefe [34] in the case of Poiseuille turbulence). Otherwise, in fully developed turbulence, detecting UPOs which represents the vortical motions in each scale and studying their orbital instability would shed new light on turbulent mechanism.

Appendix A

Appendix : Kolmogorov flow problem

A.1 Pomeau-Manneville scenario in chaotic Kolmogorov flow

Here, we study how the Kolmogorov flows become chaotic examing a critical exponent and a delay coordinate map which are the usual ways in low dimensional dynamical system[1].

At Reynolds number $R = 18.0$, there are four stable quasi-periodic solutions due to the symmetry of the Kolmogorov flow system, which is indicated by projections of the solution orbits, Lyapunov exponents and power spectrum (see chapter 2)[2]. At the critical Reynolds number ($R_T = 18.1574$), the quasi-periodic solutions become unstable and merge into a large chaotic attractor composed of the four (unstable) quasi-periodic solutions and their connecting orbits. The chaotic solution then wanders around the unstable quasi-periodic solutions and 'jumps' between them intermittently. The energy also undergo intermittent bursts simultaneously with the jumps and the average interval of time between energy bursts get longer as $R \to R_T + 0$. The type of intermittency can be categorized according to the critical exponent γ which is defined by $\langle \tau \rangle_R \propto \frac{1}{(R-R_T)^\gamma}$ where $\langle \tau \rangle_R$ is the average time interval between energy bursts [8]. To study the intermittency appearing in chaotic Kolmogorov flows, we show $\langle \tau \rangle_R$ in Fig.A.1 (a) by using three different initial conditions. The horizontal line is $R - R_T$ and the green line is

[1] Published in Inubushi *et al.* [9].

[2] Only in this section, we write Reynolds number R/R_{cr} as simply R.

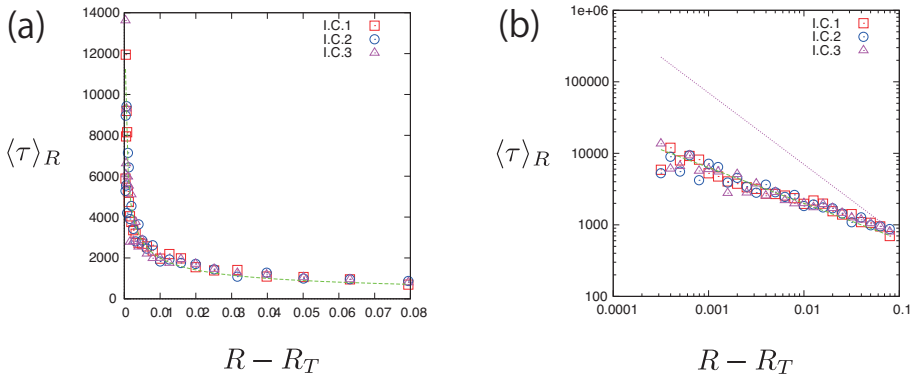

Fig. A.1: (a) Dependence of the average time interval between the energy bursts $\langle\tau\rangle_R$ on the distance from the critical Reynolds number R_T. The three symbols (square, circle, triangle) denote the data using the different initial conditions. (b) log-log plot of (a). The pink and green line denote $(R-R_T)^{-1}$ and $(R-R_T)^{-1/2}$ respectively.

proportional to $(R-R_T)^{-1/2}$. Fig.A.1 (b) is log-log plot of Fig.A.1 (a) The pink line is proportional to $(R-R_T)^{-1}$ and the green line is proportional to $(R-R_T)^{-1/2}$. Each data point appears to lie on the green line, which implies the intermittency appearing in chaotic Kolmogorov flows is *type-I* ($\gamma = 1/2$).

To see the validity of this categorization, we apply the time delay coordinate embedding methods to the chaotic Kolmogorov flows at $R = 18.2$ displaying intermittent behavior. As a delay coordinate, we use (E_n, E_{n+1}) where E_n denotes the value of the local maxima of the energy at "time" n. Fig.A.2 shows the delay coordinate map of this system. The red point is (E_n, E_{n+1}) and the blue line denotes $E_n = E_{n+1}$.

It is found that the part of red point appears to form a convex function nearly tangent to the $E_n = E_{n+1}$ line quadratically. At lower Reynolds number $R = 18.156 < R_T$, this map become one fixed point on the $E_n = E_{n+1}$ line, which corresponds to the quasi-periodic solution. Note that one of the two oscillations of quasi-periodic solution does not change the energy but corresponds to the travelling motion to x direction. And also the unclarity (clarity) of the map may correspond to the high (low) dimensionality of the stable (unstable) manifolds of the unstable quasi-periodic orbit. All these observations are consistent with the saddle-node bifurcation of quasi-periodic solutions, suggesting the type-I intermittency.

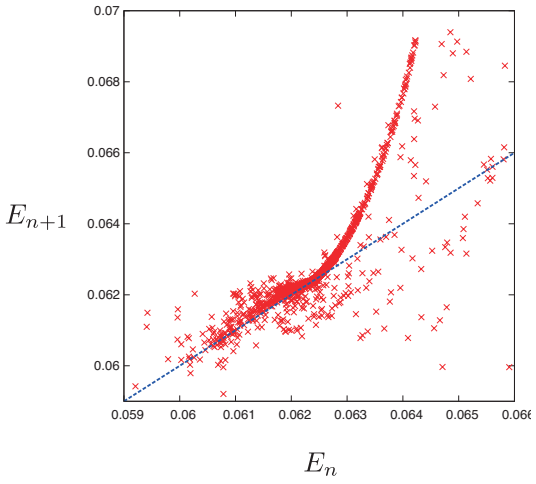

Fig. A.2: Delay coordinate map of the chaotic Kolmogorov flows at $R = 18.2$. The blue line denotes $E_n = E_{n+1}$.

Appendix B

Appendix : Couette flow problem

B.1 Formulation of Couette flow problem

B.1.1 Decomposition of velocity field and pressure field

Here we consider a decomposition of the velocity and pressure fields to a mean part and a fluctuation part. Hereafter we refer to the horizontal mean $\langle\cdot\rangle_H$ and the volume mean $\langle\cdot\rangle_V$ as

$$\left\langle \cdot \right\rangle_H = \frac{1}{L_x L_y} \int_0^{L_y} \int_0^{L_x} \cdot \, dxdy, \tag{B.1}$$

$$\left\langle \cdot \right\rangle_V = \frac{1}{2L_x L_y} \int_{z=-1}^{z=+1} \int_{y=0}^{y=L_y} \int_{x=0}^{x=L_x} \cdot \, dxdydz. \tag{B.2}$$

decomposition of the velocity field

The velocity field is decomposed to a mean and a fluctuation part;

$$\boldsymbol{u}(x,y,z,t) = \underbrace{\boldsymbol{U}(z,t)}_{\text{mean part}} + \underbrace{\tilde{\boldsymbol{u}}(x,y,z,t)}_{\text{fluctuation part}} \tag{B.3}$$

where

$$\boldsymbol{U}(z,t) = \langle \boldsymbol{u}(x,y,z,t) \rangle_H \tag{B.4}$$

$$\tilde{\boldsymbol{u}}(x,y,z,t) = \boldsymbol{u}(x,y,z,t) - \boldsymbol{U}(z,t). \tag{B.5}$$

decomposition of the pressure field

Volume mean of the wall-normal gradient of the pressure is zero[1]; $\langle \frac{\partial}{\partial z}\ p\rangle_V = 0$. Therefore the volume mean of the pressure gradient is

$$\left\langle \boldsymbol{\nabla} p \right\rangle_V = \Pi_x(t)\boldsymbol{e}_x + \Pi_y(t)\boldsymbol{e}_y \tag{B.9}$$

where $\Pi_x(t)$ is the streamwise (x-direction) mean pressure gradient and $\Pi_y(t)$ is the spanwise (y-direction) mean pressure gradient. Then the fluctuation part of the pressure gradient $\boldsymbol{\nabla} p'$can be defined as

$$\boldsymbol{\nabla} p'(x,y,z,t) = \boldsymbol{\nabla} p(x,y,z,t) - \Pi_x(t)\boldsymbol{e}_x - \Pi_y(t)\boldsymbol{e}_y \tag{B.10}$$

and p' is periodic in the horizontal direction[2].

Finally, the decomposition of the pressure field is

$$p(x,y,z,t) = \Pi_x(t)x + \Pi_y(t)y + p'(x,y,z,t) \tag{B.11}$$

and the decomposition of the pressure gradient field is

$$\boldsymbol{\nabla} p(x,y,z,t) = \underbrace{\Pi_x(t)\boldsymbol{e}_x}_{x\text{-mean pressure grad.}} + \underbrace{\Pi_y(t)\boldsymbol{e}_y}_{y\text{-mean pressure grad.}} + \underbrace{\boldsymbol{\nabla} p'(x,y,z,t)}_{\text{fluctuating pressure grad.}} . \tag{B.12}$$

[1]Using z-directional mean of the mean flow equation (B.69) in Appendix with the incompressibility and the periodicity of the velocity field in the horizontal direction

$$\frac{\partial}{\partial t}\langle u_z\rangle_V = -\left\langle \frac{\partial p}{\partial z}\right\rangle_V + \frac{1}{Re}\left\langle \frac{\partial^2}{\partial z^2}u_z\right\rangle_V \tag{B.6}$$

$$= -\left\langle \frac{\partial p}{\partial z}\right\rangle_V + \frac{1}{Re}\left\langle \frac{\partial}{\partial z}(-\frac{\partial u_x}{\partial x} - -\frac{\partial u_y}{\partial y})\right\rangle_V \tag{B.7}$$

$$= -\left\langle \frac{\partial p}{\partial z}\right\rangle_V . \tag{B.8}$$

Since the left hand side of this equation is zero (see Eq. (B.70)), we can get $\langle \frac{\partial p}{\partial z}\ \rangle_V = 0$.

[2] The streamwise derivative of the pressure $\frac{\partial p}{\partial x}$ is periodic in the horizontal direction, so $p = c_1 x + f(x,y,z)$ (f is periodic function in x-direction). And the spanwise derivative of the pressure $\frac{\partial p}{\partial y}$ is also periodic in the horizontal direction, $p = c_2 y + g(x,y,z)$ (g is periodic function in y-direction). Therefore the fluctuation part of the pressure p' is periodic in the horizontal direction when we put $c_1 = \Pi_x, c_2 = \Pi_y, h = p'$. It is to be noted that c_1, c_2 do not depend on z. If c_1, c_2 depend on z, $\partial_z p = c_1'(z)x + c_2'(z)y + \partial_z h(x,y,z)$ which violates the horizontal periodicity of the z-directional pressure gradient.

B.1.2 Equations of mean flow and fluctuating flow

Substituting the decomposition of velocity and pressure gradient (B.3) , (B.12) in the Navier-Stokes equations (3.1),

$$\frac{\partial}{\partial z}U_z + \boldsymbol{\nabla}\cdot\tilde{\boldsymbol{u}} = 0, \tag{B.13}$$

$$\frac{\partial \boldsymbol{U}}{\partial t} + \frac{\partial \tilde{\boldsymbol{u}}}{\partial t} + (\boldsymbol{u}\cdot\boldsymbol{\nabla})\boldsymbol{u} = -\Pi_x(t)\boldsymbol{e}_x - \Pi_y(t)\boldsymbol{e}_y - \boldsymbol{\nabla}p' + \frac{1}{Re}\frac{\partial^2}{\partial z^2}\boldsymbol{U} + \frac{1}{Re}\boldsymbol{\nabla}^2\tilde{\boldsymbol{u}} \tag{B.14}$$

Since the wall-normal mean flow is identical to zero ; $U_z(z,t)=0$, the continuity equation is

$$\boldsymbol{\nabla}\cdot\tilde{\boldsymbol{u}} = 0. \tag{B.15}$$

Therefore the fluctuating velocity field can be decomposed into the toroidal and the poloidal potentials as follows;

$$\tilde{\boldsymbol{u}} = \boldsymbol{\nabla}\times(\tilde{\psi}\boldsymbol{e}_z) + \boldsymbol{\nabla}\times\boldsymbol{\nabla}\times(\tilde{\phi}\boldsymbol{e}_z) \tag{B.16}$$

or

$$\tilde{u}_x = \frac{\partial\tilde{\psi}}{\partial y} + \frac{\partial^2\tilde{\phi}}{\partial x\partial z},\quad \tilde{u}_y = -\frac{\partial\tilde{\psi}}{\partial x} + \frac{\partial^2\tilde{\phi}}{\partial y\partial z},\quad \tilde{u}_z = -\boldsymbol{\nabla}_H^2\tilde{\phi}. \tag{B.17}$$

Inversely operating $\boldsymbol{e}_z\cdot$ and $\boldsymbol{e}_z\cdot\boldsymbol{\nabla}\times$ on the equations (B.16) respectively, the toroidal and poloidal potentials can be written by the wall-normal velocity and vorticity component as $\tilde{\psi} = -\boldsymbol{\nabla}_H^{-2}\tilde{\omega}_z,\ \tilde{\phi} = -\boldsymbol{\nabla}_H^{-2}\tilde{u}_z$.

The mean flows have the horizontal components only, therefore

$$\boldsymbol{U} = \begin{pmatrix} U_x(z,t) \\ U_y(z,t) \\ 0 \end{pmatrix} \tag{B.18}$$

$$\boldsymbol{e}_z\cdot\boldsymbol{\nabla}\times\boldsymbol{U} = \boldsymbol{e}_z\cdot\begin{pmatrix} -\partial_z U_y \\ \partial_z U_x \\ 0 \end{pmatrix} = 0 \tag{B.19}$$

$$\boldsymbol{e}_z\cdot\boldsymbol{\nabla}\times\boldsymbol{\nabla}\times\boldsymbol{U} = -\boldsymbol{e}_z\cdot\begin{pmatrix} \partial_z^2 U_x \\ \partial_z^2 U_y \\ 0 \end{pmatrix} = 0. \tag{B.20}$$

Thus, operating $\boldsymbol{e}_z \cdot \boldsymbol{\nabla}\times$ and $\boldsymbol{e}_z \cdot \boldsymbol{\nabla} \times \boldsymbol{\nabla}\times$ on the Navier-Stokes equations (B.14), the evolution equation of the potentials are found to be

$$\frac{\partial}{\partial t}\boldsymbol{\nabla}_H^2\tilde{\psi} + \boldsymbol{e}_z \cdot \boldsymbol{\nabla} \times (\boldsymbol{u} \times \boldsymbol{\omega}) = \frac{1}{Re}\boldsymbol{\nabla}_H^2\boldsymbol{\nabla}^2\tilde{\psi}, \tag{B.21}$$

$$\frac{\partial}{\partial t}\boldsymbol{\nabla}_H^2\boldsymbol{\nabla}^2\tilde{\phi} - \boldsymbol{e}_z \cdot \boldsymbol{\nabla} \times \boldsymbol{\nabla} \times (\boldsymbol{u} \times \boldsymbol{\omega}) = \frac{1}{Re}\boldsymbol{\nabla}_H^2\boldsymbol{\nabla}^2\boldsymbol{\nabla}^2\tilde{\phi}, . \tag{B.22}$$

Evolution equations of the mean flows are

$$\frac{\partial}{\partial t}\boldsymbol{U} + \frac{\partial}{\partial z}\langle u_z\boldsymbol{u}\rangle_H = -\langle\boldsymbol{\nabla}p\rangle_H + \frac{1}{Re}\frac{\partial^2}{\partial z^2}\boldsymbol{U} \tag{B.23}$$

(see B.1.5 for details). Decomposing the pressure gradient field and using the periodicity of p', the horizontal mean of the pressure gradient is $\langle\boldsymbol{\nabla}p\rangle_H = \langle\Pi_x(t)\boldsymbol{e}_x\rangle_H + \langle\Pi_y(t)\boldsymbol{e}_y\rangle_H + \langle\boldsymbol{\nabla}p'\rangle_H = \Pi_x(t)\boldsymbol{e}_x + \Pi_y(t)\boldsymbol{e}_y$. Therefore the evolution equation of the mean flows are found to be

$$\frac{\partial}{\partial t}\boldsymbol{U} + \frac{\partial}{\partial z}\langle u_z\boldsymbol{u}\rangle_H = -\Pi_x(t)\boldsymbol{e}_x - \Pi_y(t)\boldsymbol{e}_y + \frac{1}{Re}\frac{\partial^2}{\partial z^2}\boldsymbol{U}. \tag{B.24}$$

To close the above equations of the mean flows $\boldsymbol{U}$, we study the relation between the mean pressure gradient Π_x, Π_y and the velocity field (volume flux) in the next section.

B.1.3 Mean pressure gradient and volume flux

x and y direction mean volume fluxes

$$F_x(x,t) = \frac{1}{2L_y}\int_0^{L_y}\int_{-1}^{+1} u_x dz dy \tag{B.25}$$

$$F_y(y,t) = \frac{1}{2L_x}\int_0^{L_x}\int_{-1}^{+1} u_y dz dx \tag{B.26}$$

are independent on the plane where the volume fluxes are defined due to the incompressibility.

For example, the streamwise derivative of the volume flux gives

$$\frac{\partial}{\partial x}F_x(x,t) = \frac{1}{2L_y}\int_0^{L_y}\int_{-1}^{+1}\frac{\partial u_x}{\partial x}dzdy \tag{B.27}$$

$$= \frac{1}{2L_y}\int_0^{L_y}\int_{-1}^{+1}\left(-\frac{\partial u_y}{\partial y} - \frac{\partial u_z}{\partial z}\right)dzdy = 0. \tag{B.28}$$

Therefore, $F_x(x,t) = F_x(t)$. The same is true for the spanwise direction.

Thus, the mean volume fluxes are equal to the mean momentums;

$$F_x(x,t) = F_x(t) = \frac{1}{L_x}\int_0^{L_x} F_x(t)dx = \langle u_x \rangle_V \tag{B.29}$$

$$F_y(y,t) = F_y(t) = \frac{1}{L_y}\int_0^{L_y} F_y(t)dy = \langle u_y \rangle_V. \tag{B.30}$$

Since the equations of the mean momentums are given by

$$\frac{d}{dt}\langle \boldsymbol{u} \rangle_V = -\langle \boldsymbol{\nabla} p \rangle_V + \frac{1}{Re}\left\langle \frac{\partial^2 \boldsymbol{U}}{\partial z^2} \right\rangle_V \tag{B.31}$$

(see B.1.6 for details), substituting $\boldsymbol{\nabla} p = \Pi_x(t)\boldsymbol{e}_x + \Pi_y(t)\boldsymbol{e}_y + \boldsymbol{\nabla} p'$ in this equations and using the periodicity of p' gives the relation between Π_x, Π_y and the mean momentums (volume fluxes);

$$\frac{d}{dt}F_x(t) = -\Pi_x(t) + \frac{1}{Re}\left\langle \frac{\partial^2 U_x}{\partial z^2} \right\rangle_V \tag{B.32}$$

$$\frac{d}{dt}F_y(t) = -\Pi_y(t) + \frac{1}{Re}\left\langle \frac{\partial^2 U_y}{\partial z^2} \right\rangle_V. \tag{B.33}$$

The viscous terms of the right hand side of the above equations are

$$\left\langle \frac{\partial^2 \boldsymbol{U}}{\partial z^2} \right\rangle_V = \frac{1}{2L_xL_y}\int_{z=-1}^{z=+1}\int_{y=0}^{y=L_y}\int_{x=0}^{x=L_x} \frac{\partial^2 \boldsymbol{U}}{\partial z^2}\, dxdydz \tag{B.34}$$

$$= \frac{1}{2}\left\{ \left(\frac{\partial \boldsymbol{U}}{\partial z}\right)\Big|_{z=1} - \left(\frac{\partial \boldsymbol{U}}{\partial z}\right)\Big|_{z=-1} \right\}, \tag{B.35}$$

which means the time evolutions of the mean momentums (volume fluxes) depend on the mean pressure gradients and the wall shear stress.

Setting A

Spanwise gradient of the mean pressure and streamwise volume flux can be set zero respectively, i.e. $F_x(t) \equiv 0$, $\Pi_y(t) \equiv 0$. We refer to this setting as *setting A* in this thesis.

In this case, the evolution equations of the mean flows are as follows from Eq.(B.24)

$$\frac{\partial}{\partial t}\boldsymbol{U} + \frac{\partial}{\partial z}\langle u_z \boldsymbol{u} \rangle_H = -\Pi_x(t)\boldsymbol{e}_x + \frac{1}{Re}\frac{\partial^2}{\partial z^2}\boldsymbol{U}. \tag{B.36}$$

Here, from Eq.(B.32) , (B.33), the streamwise mean pressure gradient and the spanwise volume flux are respectively

$$\Pi_x(t) = \frac{1}{Re}\left\langle \frac{\partial^2 U_x}{\partial z^2} \right\rangle_V \tag{B.37}$$

$$\frac{d}{dt}F_y(t) = \frac{1}{Re}\left\langle \frac{\partial^2 U_y}{\partial z^2} \right\rangle_V. \tag{B.38}$$

Therefore, Eq. (B.37) gives the streamwise mean pressure gradient $\Pi_x(t)$ in the evolution equation of the mean flows. Note that if Eq. (B.37) is satisfied, then $\frac{d}{dt}F_x(t) \equiv 0$. Thus, we must employ the initial conditions such that $F_x(0) = 0$ so that $F_x(0) = 0$.

Setting B

Both streamwise and spanwise gradient of the mean pressure can be set zero respectively, i.e. $\Pi_x(t) \equiv 0,\ \Pi_y(t) \equiv 0$. We refer to this setting as *setting B* in this thesis.

In this case, the evolution equations of the mean flows are as follows from Eq.(B.24)

$$\frac{\partial}{\partial t}\boldsymbol{U} + \frac{\partial}{\partial z}\langle u_z \boldsymbol{u}\rangle_H = \frac{1}{Re}\frac{\partial^2}{\partial z^2}\boldsymbol{U}. \tag{B.39}$$

Here, from Eq.(B.32) , (B.33), the streamwise and the spanwise volume flux are respectively

$$\frac{d}{dt}F_x(t) = \frac{1}{Re}\left\langle \frac{\partial^2 U_x}{\partial z^2} \right\rangle_V \tag{B.40}$$

$$\frac{d}{dt}F_y(t) = \frac{1}{Re}\left\langle \frac{\partial^2 U_y}{\partial z^2} \right\rangle_V. \tag{B.41}$$

B.1.4 Boundary conditions

Finally, we consider the boundary conditions of the mean and fluctuation flows.

boundary conditions of the velocity fields

Corresponding to the boundary conditions Eq.(3.3) , (3.4), the fluctuation velocities are non-slip on the walls ($z = \pm 1$)

$$\tilde{u}_x(x, y, \pm 1) = \tilde{u}_y(x, y, \pm 1) = \tilde{u}_z(x, y, \pm 1) = 0, \tag{B.42}$$

and periodic in horizontal directions

$$\tilde{\boldsymbol{u}}(x,y,z) = \tilde{\boldsymbol{u}}(x+L_x,y,z) = \tilde{\boldsymbol{u}}(x,y+L_y,z). \tag{B.43}$$

The boundary conditions of the mean flows are

$$U_x(z=\pm 1,t) = \pm 1 \tag{B.44}$$
$$U_y(z=\pm 1,t) = 0. \tag{B.45}$$

boundary conditions of the fluctuation velocity fields

Here we describe the boundary conditions of the fluctuation velocity fields by using the potentials. If the potentials on the walls are given by

$$\tilde{\phi}(x,y,\pm 1) = 0, \tag{B.46}$$
$$\frac{\partial\tilde{\phi}}{\partial z}(x,y,\pm 1) = \tilde{\psi}(x,y,\pm 1) = 0, \tag{B.47}$$

then, the fluctuation velocity fields satisfy the non-slip boundary conditions Eq.(B.42). Conversely, here we consider the case that the fluctuation velocity fields satisfy the non-slip boundary conditions on the walls Eq.(B.42), i.e.

$$\tilde{u}_x = \frac{\partial\tilde{\psi}}{\partial y} + \frac{\partial^2\tilde{\phi}}{\partial x\partial z} = 0 \qquad (z=\pm 1) \tag{B.48}$$
$$\tilde{u}_y = -\frac{\partial\tilde{\psi}}{\partial x} + \frac{\partial^2\tilde{\phi}}{\partial y\partial z} = 0 \quad (z=\pm 1) \tag{B.49}$$
$$\tilde{u}_z = -\boldsymbol{\nabla}_H^2\tilde{\phi} = 0 \qquad\qquad (z=\pm 1). \tag{B.50}$$

The addition ∂_x(B.48)+∂_y(B.49) leads to $\boldsymbol{\nabla}_H^2\partial_z\tilde{\phi} = 0 \;\; (z=\pm 1)$ and the subtraction ∂_y(B.48)$-\partial_x$(B.49) leads to $\boldsymbol{\nabla}_H^2\tilde{\psi} = 0 \;\; (z=\pm 1)$. Employing the property of harmonic function and using Eq.(B.50), it is found that $\partial_z\tilde{\phi},\ \tilde{\psi},\ \tilde{\phi}$ are constant on the walls[3]. The potentials $\tilde{\psi},\tilde{\phi}$ have redundant degrees of

[3]Let us consider doubly periodic (in x,y-direction) Harmonic function $u(x,y)$ and its conjugate harmonic function $v(x,y) \quad (\partial_x u = \partial_y v, \partial_y u = -\partial_x v)$. Then, a complex-valued function $f(z) = u + iv$ is is holomorphic over the whole complex plane (entire function) where $z = x + iy$. Liouville's theorem states that every bounded entire function $f(z)$ must be constant. Therefore, $u(x,y) =$ constant. [Sketch of proof of Liouville's theorem] There exists a constant M such that $|f(z)| \le M$. Taylor expansion $f(z) = \sum_{n=0}^{\infty} a_n z^n$ and Cauchy's integral formula lead to $|a_n| \le |\oint_{|\zeta|=R} f(\zeta)/\zeta^{n+1} d\zeta/(2\pi i)| \le \int_0^{2\pi} M/R^{n+1} R d\theta/(2\pi) = M/R^n$. Therefore, with $R\to\infty$, $f(z) = a_0$ (i.e. constant).

freedom (cf. gauge transformation);

$$\tilde{\psi}\boldsymbol{e}_z \to \tilde{\psi}\boldsymbol{e}_z + \boldsymbol{\nabla} f(z), \tag{B.51}$$

$$\tilde{\phi}\boldsymbol{e}_z \to \tilde{\phi}\boldsymbol{e}_z + \boldsymbol{\nabla} g(z). \tag{B.52}$$

Therefore, we can take f, g such that

$$\partial_z\tilde{\phi} = 0, \quad \tilde{\psi} = 0, \quad \tilde{\phi} = 0 \tag{B.53}$$

on the walls $(z = \pm 1)$[4] .

Boundary conditions of the potentials are periodic in the horizontal directions;

$$\tilde{\psi}(x, y, z) = \tilde{\psi}(x + L_x, y, z) = \tilde{\psi}(x, y + L_y, z), \tag{B.58}$$

$$\tilde{\phi}(x, y, z) = \tilde{\phi}(x + L_x, y, z) = \tilde{\phi}(x, y + L_y, z). \tag{B.59}$$

boundary conditions of the fluctuation pressure fields

Boundary conditions of the fluctuation pressure fields are periodic in horizontal directions;

$$p'(x, y, z) = p'(x + L_x, y, z) = p'(x, y + L_y, z) \tag{B.60}$$

(see the footnote 2).

B.1.5 Derivation of horizontal mean flow equation

We here derive the horizontal mean flow equation. We denote the horizontal mean as $\langle\cdot\rangle_H = \frac{1}{L_x L_y}\int_0^{L_y}\int_0^{L_x} \cdot\, dxdy$. Let us consider the horizontal mean Navier-Stokes equation

$$\frac{\partial}{\partial t}\langle\boldsymbol{u}\rangle_H + \langle(\boldsymbol{u}\cdot\boldsymbol{\nabla})\boldsymbol{u}\rangle_H = -\langle\boldsymbol{\nabla}p\rangle_H + \frac{1}{Re}\langle\boldsymbol{\nabla}^2\boldsymbol{u}\rangle_H. \tag{B.61}$$

[4]On the walls $(z = \pm 1)$, $\partial_z\tilde{\phi},\ \tilde{\psi},\ \tilde{\phi}$ are constant. For instance, let us consider the case that

$$\partial_z\tilde{\phi} = c_1, \quad \tilde{\psi} = c_2, \quad \tilde{\phi} = c_3 \tag{B.54}$$

on $z = +1$ where c_1, c_2, c_3 are some constants. In this case, if we set $f(z) = -c_2 z,\ g(z) - (c_3 - c_1)z - c_1/2z^2$, then

$$\psi\boldsymbol{e}_z = \tilde{\psi}\boldsymbol{e}_z + \boldsymbol{\nabla} f(z) = (\tilde{\psi} - c_2)\boldsymbol{e}_z, \tag{B.55}$$

$$\phi\boldsymbol{e}_z = \tilde{\phi}\boldsymbol{e}_z + \boldsymbol{\nabla} g(z) = (\tilde{\phi} - (c_3 - c_1) - c_1 z)\boldsymbol{e}_z \tag{B.56}$$

$$\partial_z\phi\boldsymbol{e}_z = \partial_z\tilde{\phi}\boldsymbol{e}_z + \boldsymbol{\nabla} g'(z) = (\partial_z\tilde{\phi} - c_1)\boldsymbol{e}_z, \tag{B.57}$$

and thus, $\psi = 0, \quad \phi = 0, \quad \partial_z\phi = 0$ on $z = +1$.

Advection term

The i-th component of the horizontal mean advection term is

$$\Big[\langle(\boldsymbol{u}\cdot\boldsymbol{\nabla})\boldsymbol{u}\rangle_H\Big]_i = \frac{1}{L_xL_y}\int_0^{L_y}\int_0^{L_x} u_j\partial_j u_i\ dxdy \tag{B.62}$$

$$= \frac{1}{L_xL_y}\int_0^{L_y}\int_0^{L_x} \partial_j(u_iu_j)\ dxdy \tag{B.63}$$

$$= \frac{1}{L_xL_y}\int_0^{L_y}\int_0^{L_x} \Big(\partial_x(u_iu_x)+\partial_y(u_iu_y)+\partial_z(u_iu_z)\Big)dxdy \tag{B.64}$$

$$= \frac{1}{L_xL_y}\int_0^{L_y}\int_0^{L_x} \partial_z(u_iu_z)\ dxdy. \tag{B.65}$$

Also, we can rewrite

$$\langle(\boldsymbol{u}\cdot\boldsymbol{\nabla})\boldsymbol{u}\rangle_H = \frac{\partial}{\partial z}\langle u_z\boldsymbol{u}\rangle_H. \tag{B.66}$$

Viscous term

The horizontal mean viscous term is

$$\langle\boldsymbol{\nabla}^2\boldsymbol{u}\rangle_H = \frac{1}{L_xL_y}\int_0^{L_y}\int_0^{L_x} \boldsymbol{\nabla}^2\boldsymbol{u}\ dxdy \tag{B.67}$$

$$= \frac{\partial^2}{\partial z^2}\langle\boldsymbol{u}\rangle_H. \tag{B.68}$$

Therefore, we obtain

$$\frac{\partial}{\partial t}\langle\boldsymbol{u}\rangle_H + \frac{\partial}{\partial z}\langle u_z\boldsymbol{u}\rangle_H = -\langle\boldsymbol{\nabla}p\rangle_H + \frac{1}{Re}\frac{\partial^2}{\partial z^2}\langle\boldsymbol{u}\rangle_H. \tag{B.69}$$

However, z-directional component of this equation is identically zero (i.e. $\langle u_z\rangle_H = 0$)[5]. We denote $\langle u\rangle_H = \boldsymbol{U}(z,t)$ and the horizontal mean flow equations are

$$\frac{\partial}{\partial t}\boldsymbol{U} + \frac{\partial}{\partial z}\langle u_z\boldsymbol{u}\rangle_H = -\langle\boldsymbol{\nabla}p\rangle_H + \frac{1}{Re}\frac{\partial^2}{\partial z^2}\boldsymbol{U}. \tag{B.71}$$

where the nonlinear term is $\frac{\partial}{\partial z}\langle u_z\boldsymbol{u}\rangle_H = \frac{\partial}{\partial z}\langle\tilde{u_z}(\boldsymbol{U}+\tilde{\boldsymbol{u}})\rangle_H$.

[5]Horizontal mean of the incompressible condition ($\boldsymbol{\nabla}\cdot\boldsymbol{u}=0$) gives

$$\langle\boldsymbol{\nabla}\cdot\boldsymbol{u}\rangle_H = \left\langle\frac{\partial u_z}{\partial z}\right\rangle_H = \frac{d}{dz}\langle u_z\rangle_H = 0. \tag{B.70}$$

Hence, $\langle u_z\rangle_H = 0$ because of the boundary conditions $\langle u_z\rangle_H(\pm1,t)=0$.

B.1.6 Derivation of momentum equation

We here derive the momentum equations. The evolutions equation of the horizontal mean flows $\boldsymbol{U}(z,t) = \langle u \rangle_H$ are

$$\frac{\partial}{\partial t}\boldsymbol{U} + \frac{\partial}{\partial z}\langle u_z \boldsymbol{u} \rangle_H = -\langle \boldsymbol{\nabla} p \rangle_H + \frac{1}{Re}\frac{\partial^2}{\partial z^2}\boldsymbol{U} \tag{B.72}$$

(see B.1.5). A calculation of the z-directional mean of the above equations gives

$$\frac{1}{2}\frac{d}{dt}\int_{-1}^{1}\boldsymbol{U}(z,t)dz + \frac{1}{2}\int_{-1}^{1}\frac{\partial}{\partial z}\langle u_z \boldsymbol{u}\rangle_H dz = -\frac{1}{2}\int_{-1}^{1}\langle \boldsymbol{\nabla} p\rangle_H dz + \frac{1}{2Re}\int_{-1}^{1}\frac{\partial^2}{\partial z^2}\boldsymbol{U}dz. \tag{B.73}$$

Here, the nonlinear term vanishes because of the boundary conditions on the walls. Since z-directional mean is

$$\frac{1}{2}\int_{-1}^{1}\langle\cdot\rangle_H \, dz = \frac{1}{2L_xL_y}\int_{z=-1}^{z=+1}\int_{y=0}^{y=L_y}\int_{x=0}^{x=L_x}\cdot \, dxdydz = \langle\cdot\rangle_V \tag{B.74}$$

, thus the evolutions equation of the horizontal mean flows are

$$\frac{d}{dt}\langle \boldsymbol{u}\rangle_V = -\langle \boldsymbol{\nabla} p\rangle_V + \frac{1}{2Re}\left\{\left(\frac{\partial \boldsymbol{U}}{\partial z}\right)\Big|_{z=1} - \left(\frac{\partial \boldsymbol{U}}{\partial z}\right)\Big|_{z=-1}\right\} \tag{B.75}$$

$$= -\langle \boldsymbol{\nabla} p\rangle_V + \frac{1}{Re}\left\langle \frac{\partial^2 \boldsymbol{U}}{\partial z^2}\right\rangle_V. \tag{B.76}$$

B.2 Supplemental data

Mean and RMS velocity profiles of minimal Couette turbulence

Here we show mean and RMS velocity profiles of minimal Couette turbulence as Fig.3 in Kawahara and Kida [25]. Fig.B.1 (a) shows mean streamwise velocity profile and Fig.B.1 (b) shows RMS velocity profiles. In Fig.B.1 (b), circle symbols indicate the streamwise component, squares the wall-normal component, and triangles the spanwise component. These profiles are in agreement with Fig.3 in Kawahara and Kida [25].

Accumulative expanding rate of the high index Lyapunov exponents

Here we show the accumulative expanding rate $\Lambda_j(t,\tau) = e^{\tilde{\lambda}_j(t,\tau)\tau}$ for $\tilde{\lambda}_j(t)$ $(1 \leq j \leq 20)$ in Fig.B.2. The accumulative expanding rates are found to display

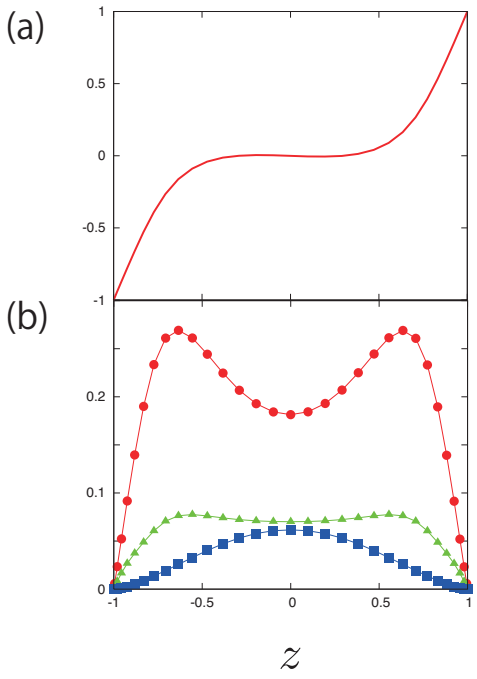

Fig. B.1: (a) The mean streamwise velocity profile, (b) The RMS velocities profiles. In (b), circle symbols indicate the streamwise component, squares the wall-normal component, and triangles the spanwise component.

almost the same behaviors qualitatively. It should be noted that in the phase (i) (Fig.B.2 (a)) even the high index accumulative expanding rate is larger than 1 until $\tau \sim 60$.

Stretching of the streamwise vortices

§3.5.1, we discussed the generation mechanism of the streamwise vortices and concluded that the streamwise vortices are generated by the vortex stretching mechanism. There, we showed the snap shots of the velocity and vorticity fields supporting this mechanism during $2748 \leq t \leq 2754$. Here we show another realizations of this mechanism. In the lower panel of the Fig.3.9, we can observe the three successive regeneration cycles and correspondingly three localization events of the streamwise vortices. The first event occurs during $2748 \leq t \leq 2754$ and we showed that the localization event appears to be explained by the vortex stretching mechanism. Thus,

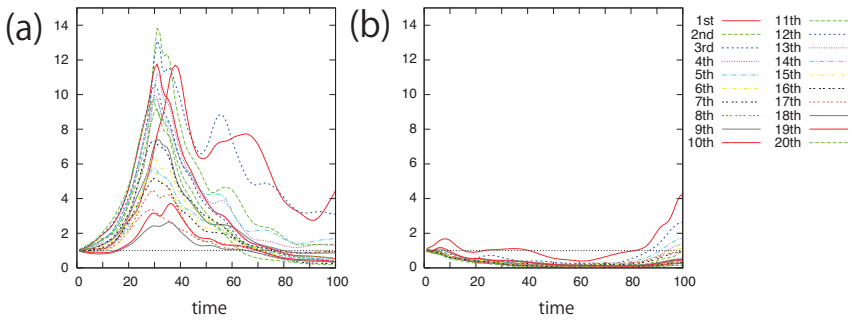

Fig. B.2: Accumulative expanding rate $\Lambda(t_0, \tau)$; (a) $t_0 = 2730$, (b) $t_0 = 2760$ for $\tilde{\lambda}_j(t)$ $(1 \leq j \leq 20)$. The black dot horizontal line denotes $\Lambda_j(t_0, \tau) \equiv 1$ (i.e. nutral).

here we show the second and third events during $2848 \leq t \leq 2854$ and $2948 \leq t \leq 2954$ respectively. It is found that these realizations also support our conclusion that the vortex stretching mechanism causes the localization of the streamwise vortices.

Wall-normal profile of the mean flow interaction term

In §3.5.2, we discussed the reformation of the streaks and focused our attention on the nonlinear interaction between the streaks and the mean flows. In particular, we showed the wall-normal profiles of the mean flow interaction term of the streak mode; $g(\boldsymbol{k}_s, z) = -2Re[\hat{u}_x^*(\boldsymbol{k}_s)\hat{u}_z(\boldsymbol{k}_s)\partial_z\hat{u}_x(\boldsymbol{0})]$ and the meandering mode; $g(\boldsymbol{k}_m, z) = -2Re[\hat{u}_x^*(\boldsymbol{k}_m)\hat{u}_z(\boldsymbol{k}_m)\partial_z\hat{u}_x(\boldsymbol{0})]$ at $t = 2800$. Here, we give these profiles throughout the regeneration cycle. Fig.B.5 showed the profiles at (a) $t = 2740$, (b) $t = 2760$, (c) $t = 2780$, (d) $t = 2800$, (e) $t = 2820$. Clearly, these profiles remain the same qualitatively and there appear to be no interaction between the meandering mode and the mean flows throughout the cycle, which also support our conclusion that the energy of the mean flows injected not into the meandering mode but into the streak mode.

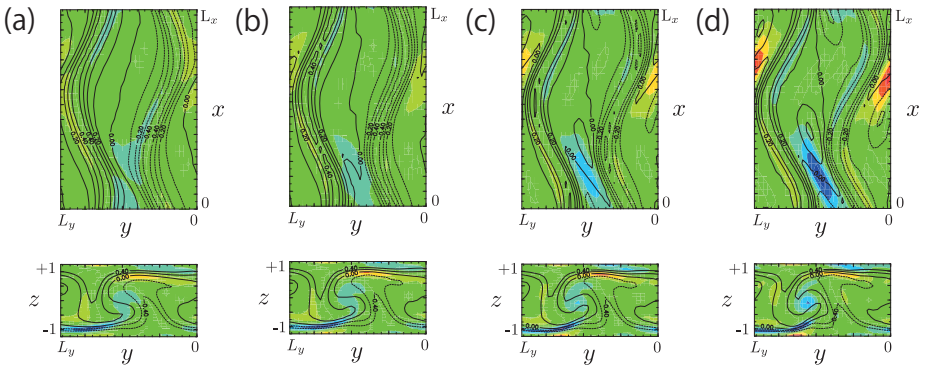

Fig. B.3: Snap shots of the streamwise velocity field $u_x(\boldsymbol{x}, t)$ (contour lines) and the streamwise vorticity field $\omega_x(\boldsymbol{x}, t)$ (tone levels) at (a): $t = 2848$,(b): $t = 2850$, (c): $t = 2852$, (d): $t = 2854$.

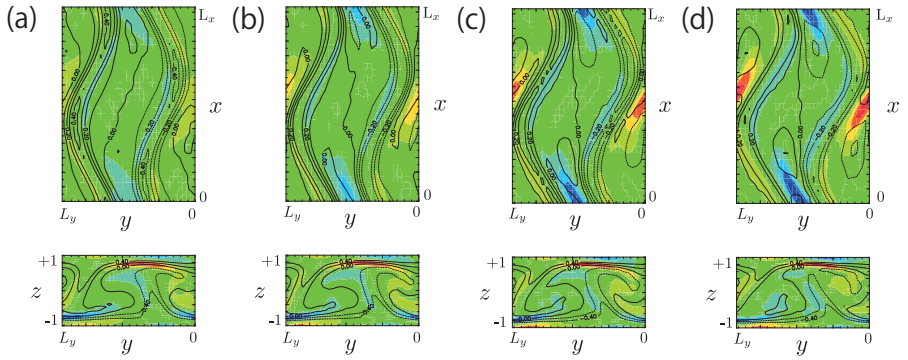

Fig. B.4: Snap shots of the streamwise velocity field $u_x(\boldsymbol{x}, t)$ (contour lines) and the streamwise vorticity field $\omega_x(\boldsymbol{x}, t)$ (tone levels) at (a): $t = 2948$,(b): $t = 2950$, (c): $t = 2952$, (d): $t = 2954$.

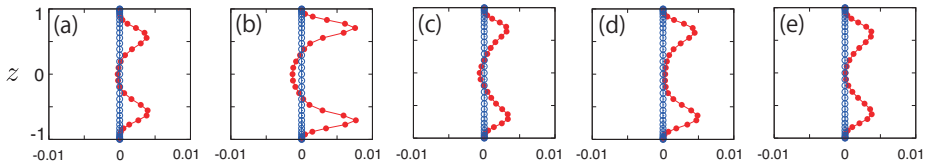

Fig. B.5: Wall-normal profiles of the mean flow interaction term of the streak mode; $g(\boldsymbol{k}_s, z) = -2Re[\hat{u}_x^*(\boldsymbol{k}_s)\hat{u}_z(\boldsymbol{k}_s)\partial_z\hat{u}_x(\boldsymbol{0})]$ (red line with closed circles) and the meandering mode; $g(\boldsymbol{k}_m, z) = -2Re[\hat{u}_x^*(\boldsymbol{k}_m)\hat{u}_z(\boldsymbol{k}_m)\partial_z\hat{u}_x(\boldsymbol{0})]$ (blue line with open circles) at (a) $t = 2740$, (b) $t = 2760$, (c) $t = 2780$, (d) $t = 2800$, (e) $t = 2820$.

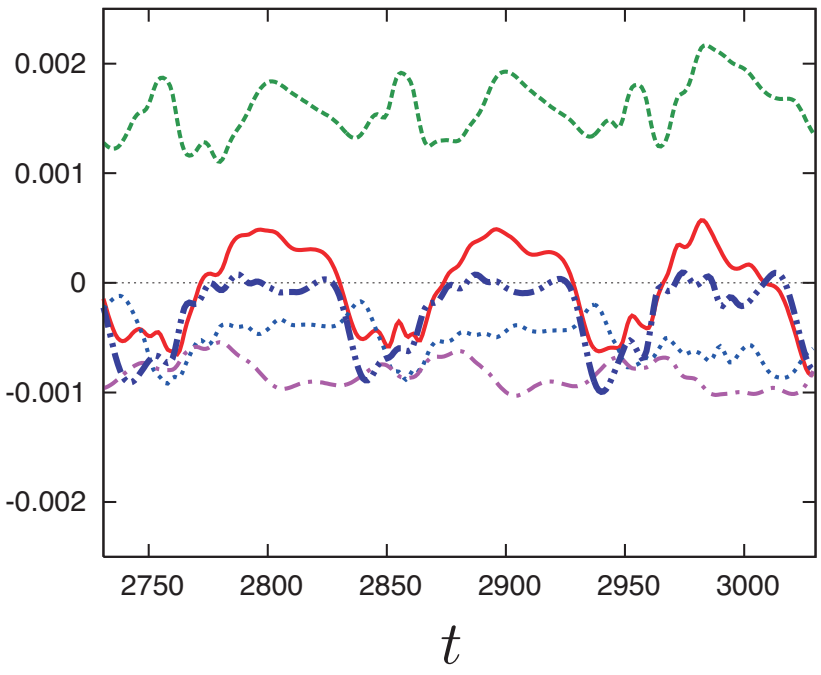

Fig. B.6: Energy budget analysis of the evolution equation of the streak mode 'energy' (3.16) during $2730 \leq t \leq 3030$ including three regeneration cycles. The red (solid) line is the time derivative term (l.h.s. of the evolution equation), the green (dashed) line is the nonlinear interaction term with the mean flow, the blue (dot) line is the other nonlinear terms, and the pink (dashed-dot) line is the viscous dissipation term. The navy (dashed double-dotted) line is the nonlinear interaction terms with the meandering mode in the equation (3.18).

Budget analysis of the evolution equation of the streak mode 'energy'

In §3, we showed Energy budget analysis of the evolution equation of the streak mode 'energy' in Fig.3.18 for a single regeneration cycle. Here, we show the same figure but including three successive cycles in Fig.B.6.

B.3 Description of the stage I in the phase (i)

Here we consider the generation of the streamwise vortices. Particularly, we discuss the stage I in the phase (i), i.e. the mechanism how the small amplitude vorticities appear at the narrow region between the meandering streaks. Hereafter, we focus our attention on the area around the reference point $(x, y, z) \sim (L_x/4, L_y/2, 0)$ (see Fig.B.7) as an example.

The streamwise vorticity equation is

$$\begin{aligned} D_t\omega_x = (\boldsymbol{\omega}\cdot\nabla)\ u_x &= \omega_x\partial_x u_x + \omega_y\partial_y u_x + \omega_z\partial_z u_x \\ &= \omega_x\partial_x u_x + (\partial_z u_x - \partial_x u_z)\partial_y u_x + (\partial_x u_y - \partial_y u_x)\partial_z u_x \\ &= \omega_x\partial_x u_x - \partial_x u_z\partial_y u_x + \partial_x u_y\partial_z u_x \end{aligned} \tag{B.77}$$

where and the viscous term is omitted for simplicity. Before the stage II (the 'turn over' the contour line illustrated in Fig.3.15), the streamwise gradient of the streamwise velocity is negative (i.e. $\partial_x u_x < 0$) around the reference point as shown in Fig.B.7 (a) (see the first term of r.h.s. of Eq.(B.77)). Thus, the vortex stretching does not occur at this time and this term damps the amplitude of the streamwise vortices. Alternatively, it is possible for the second and third term of r.h.s. of Eq.(B.77) to generate the streamwise vortices. At this time, it is found that the wall-normal gradient of the streamwise velocity is negative : $\partial_z u_x < 0$ as shown in the lower panel of Fig.3.15) (a). Furthermore, the spanwise gradient of the streamwise velocity is positive : $\partial_y u_x > 0$ as shown in Fig.B.7 (a) and also the streamwise gradient of the spanwise velocity is positive : $\partial_x u_y > 0$ as shown in Fig.B.7 (b). Since the the streamwise gradient of the wall-normal velocity is nearly zero : $\partial_x u_z \sim 0$, the vorticity equation become $D_t\omega_x \simeq \partial_x u_y\partial_z u_x < 0$ where and the stretching term is omitted. As a result, the small amplitude negative vorticity appears at the narrow region between the meandering streaks, which plays the important role in the stage II in phase (i) as described in §3.5.1.

B.4 Energy cascade in regeneration cycle

In this section, we briefly study energy cascade in minimal Couette turbulence. Firstly, we define energy spectrum function at z-plane $E(K, z)$ as

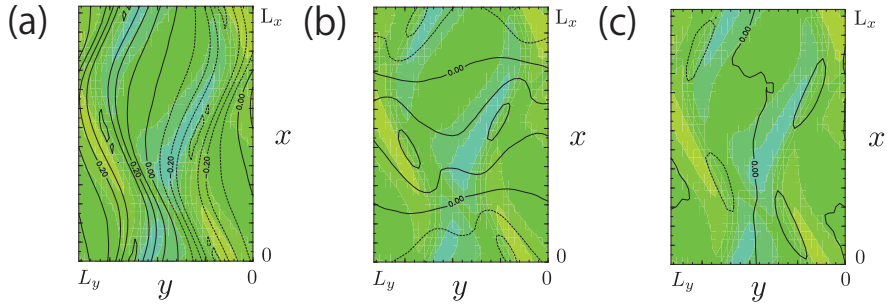

Fig. B.7: Contour lines: snap shots of (a) the streamwise velocity field $u_x(\boldsymbol{x}, t)$, (b) the spanwise velocity field $u_y(\boldsymbol{x}, t)$, and (c) the wall-normal velocity field $u_z(\boldsymbol{x}, t)$ at $t = 2744$ (just before the time when the snap shots shown in Fig.3.14 are taken). Tone levels: the streamwise vorticity field $\omega_x(\boldsymbol{x}, t)$. The snap shots are cross-sectional view taken along $z = 0$ plane.

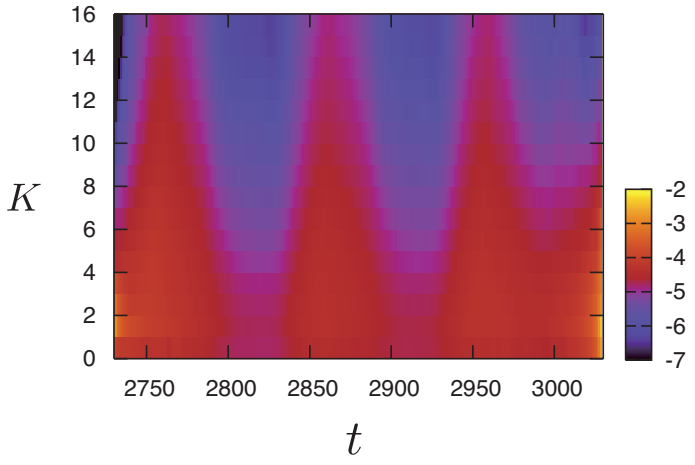

Fig. B.8: Energy spectrum function at mid-plane $E(K, z = 0)$ during $2730 \leq t \leq 3030$ including three regeneration cycles. Horizontal axis is time t, vertical axis is wavenumber K, and color tone is $\log E(K, z = 0)$.

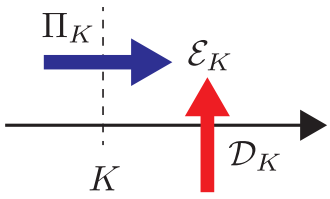

Fig. B.9: Illustration of energy budget in wavenumber space. $\mathcal{E}_K$ denotes cumulative energy (energy for the wavenumber range higher than K), Π_K denotes energy flux (energy coming into the wavenumber range higher than K via nonlinear interaction), and $\mathcal{D}_K$ denotes energy injection and dissipation (energy coming into the wavenumber range higher than K via viscous term).

follows :

$$E(K,z) = \frac{1}{2} \sum_{K \le |\hat{\boldsymbol{k}}| < K+1} |\hat{\boldsymbol{u}}(\hat{\boldsymbol{k}}, z)|^2 \tag{B.78}$$

where $\hat{\boldsymbol{k}} = (k_x, k_y)$. We show the energy spectrum function at mid-plane ($z = 0$) $E(K, z = 0)$ in Fig.B.8 during $2730 \le t \le 3030$ including three regeneration cycles. Horizontal axis is time t, vertical axis is wavenumber K, and color tone is $\log E(K, z = 0)$. It is found that at high wavenumber ($K \gtrsim 4$) the energy spectrum drastically change through the cycles. In particular, large scale structures (low wavenumber modes) contain almost all energy at the initial stage of the cycle (e.g. $t \sim 2730$), and soon after that (e.g. $t \sim 2760$) energy appears to cascade down to small scale structures (higher wavenumber modes).

Examining energy flow in the minimal Couette turbulence in more deital, we study scale-by-scale energy budget equation (see §2.4 in Frisch [1]) :

$$\frac{d}{dt}\mathcal{E}_K = \Pi_K + \mathcal{D}_K \tag{B.79}$$

where

$$\hat{\boldsymbol{u}}_K^<(\boldsymbol{x},z) = \sum_{|\hat{\boldsymbol{k}}|<K} \hat{\boldsymbol{u}}(\boldsymbol{k},z)e^{i\hat{\boldsymbol{k}}\cdot\boldsymbol{x}}, \tag{B.80}$$

$$\hat{\boldsymbol{u}}_K^>(\boldsymbol{x},z) = \sum_{|\hat{\boldsymbol{k}}|\geq K} \hat{\boldsymbol{u}}(\boldsymbol{k},z)e^{i\hat{\boldsymbol{k}}\cdot\boldsymbol{x}}, \tag{B.81}$$

$$\mathcal{E}_K = \frac{1}{2}\left\langle |\hat{\boldsymbol{u}}_K^>|^2 \right\rangle_V, \tag{B.82}$$

$$\Pi_K = -\left\langle \hat{\boldsymbol{u}}_K^> \cdot (\hat{\boldsymbol{u}}_K^< \cdot \boldsymbol{\nabla}\hat{\boldsymbol{u}}_K^<) \right\rangle_V - \left\langle \hat{\boldsymbol{u}}_K^> \cdot (\hat{\boldsymbol{u}}_K^> \cdot \boldsymbol{\nabla}\hat{\boldsymbol{u}}_K^<) \right\rangle_V, \tag{B.83}$$

$$\mathcal{D}_K = \frac{1}{Re}\left\langle \hat{\boldsymbol{u}}_K^> \cdot \boldsymbol{\nabla}^2\hat{\boldsymbol{u}}_K^> \right\rangle_V. \tag{B.84}$$

In the above equations, $\hat{\boldsymbol{u}}_K^<$ denotes *low-pass* filtered velocity field, $\hat{\boldsymbol{u}}_K^>$ denotes *high-pass* filtered velocity field, $\mathcal{E}_K$ denotes *cumulative* energy, Π_K denotes *energy flux*, and $\mathcal{D}_K$ denotes energy injection and dissipation. As illustrated in Fig.B.9, the cumulative energy $\mathcal{E}_K$ is energy for the wavenumber range higher than K, the energy flux Π_K is energy coming into the wavenumber range higher than K per unit time via nonlinear interaction, and the energy injection and dissipation $\mathcal{D}_K$ is energy coming into the wavenumber range higher than K per unit time via viscous term.

Fig.B.10 shows time series of (a) the cumulative energy $\mathcal{E}_K$, (b) the energy flux Π_K, and (c) the energy injection and dissipation $\mathcal{D}_K$ during $2730 \leq t \leq 3030$ including three regeneration cycles for the red line : $K = 0$, the green line : $K = 1$, the blue line : $K = 2$, the pink line : $K = 3$, the light blue line : $K = 4$, the yarrow line : $K = 5$, the black line : $K = 10$, and the orange line : $K = 15$. As a reference, time series of the horizontal RMS of the streamwise vortices $\sqrt{\langle\omega_x^2\rangle_H}$ is shown in Fig.B.10 (d) (the same figure as the lower panel of Fig.3.9), which characterizes localization of the streamwise vortices. Increase and decrease of the cumulative energy $\mathcal{E}_K$ found in Fig.B.10 (a) are considered to correspond to the formation and breakdown of the streaks. The energy flux Π_K is positive throughout the regeneration cycles, indicating that the energy actually cascades down to small structures (higher wavenumber modes). More importantly, the three sharp peaks of the energy flux Π_K and the energy injection and dissipation $\mathcal{D}_K$ clearly correspond to those of the horizontal RMS of the streamwise vortices $\sqrt{\langle\omega_x^2\rangle_H}$. At the wavenumber $K = 0$, the energy injection and dissipation $\mathcal{D}_K$ become positive after the peaks, which is consistent with the fart that the energy is injected

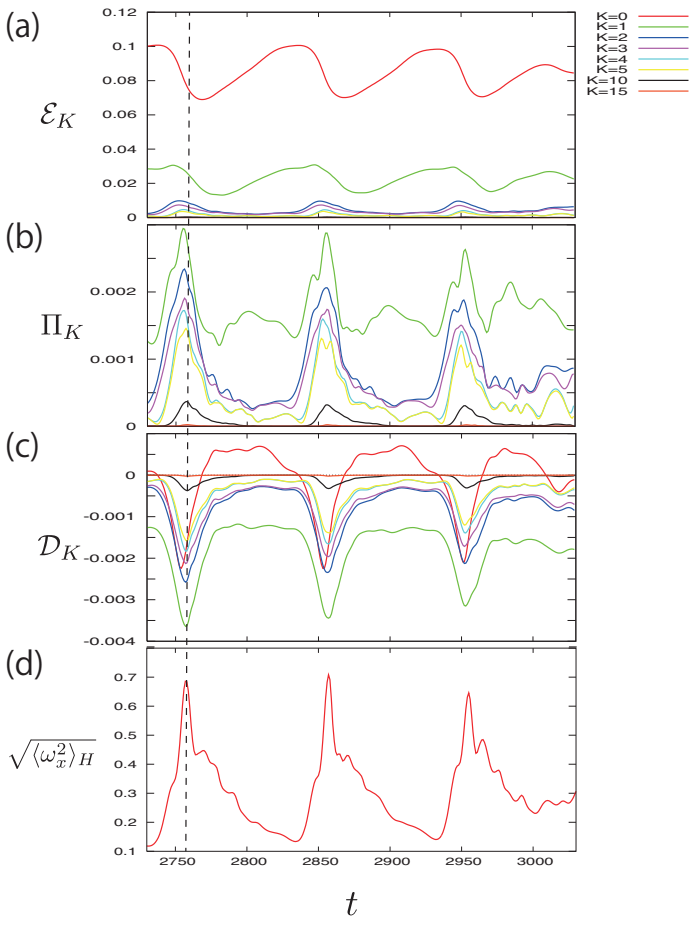

Fig. B.10: Time series of (a) the cumulative energy $\mathcal{E}_K$, (b) the energy flux Π_K, and (c) the energy injection and dissipation $\mathcal{D}_K$ during $2730 \leq t \leq 3030$ including three regeneration cycles for $K = 0$ (red), $K = 1$ (green), $K = 2$ (blue), $K = 3$ (pink), $K = 4$ (light blue), $K = 5$ (yarrow), $K = 10$ (black), and $K = 15$ (orange). (d) Time series of the horizontal RMS of the streamwise vortices $\sqrt{\langle\omega_x^2\rangle_H}$ (the same figure as the lower panel of Fig.3.9).

from walls to mean flows (i.e. $K = 0$ modes). At the wavenumber range of $K > 0$, the energy injection and dissipation $\mathcal{D}_K$ are negative throughout the cycles, corresponding to the energy dissipation. These observations support that the localization of the streamwise vortices induces the energy cascade and energy dissipation strongly.

B.5 Derivation of evolution equation of modal energy

Here we derive the the evolution equation of the modal energy with focusing on the mean flow interactions. First, we consider the horizontal Fourier coefficient of the velocity fields $\hat{\boldsymbol{u}}(\boldsymbol{k}, z) = \left\langle \boldsymbol{u}(x, y, z) e^{-i\boldsymbol{k}\cdot\boldsymbol{x}} \right\rangle_H$ and derive the evolution equations of the modal 'energy'. Hereafter, we write the energy as $\hat{\boldsymbol{u}}(\boldsymbol{k}, z) = \hat{\boldsymbol{u}}(\boldsymbol{k})$ shortly. The goal of the derivation in this section is to obtain the evolution equations of the modal 'energy';

$$
\begin{aligned}
\frac{d}{dt}\left\langle |\hat{\boldsymbol{u}}(\boldsymbol{k})|^2 \right\rangle_z =& -\left\langle 2Re[\hat{\boldsymbol{u}}^*(\boldsymbol{k}) \cdot \big(\hat{u}_z(\boldsymbol{k})\partial_z\big)\hat{\boldsymbol{u}}(\boldsymbol{0})] \right\rangle_z \\
& -\left\langle \sum_{\substack{\boldsymbol{k}''+\boldsymbol{k}'=\boldsymbol{k}, \\ \boldsymbol{k}'\neq\boldsymbol{0}, \boldsymbol{k}''\neq\boldsymbol{0}}} \mathcal{N}(\hat{\boldsymbol{u}}(\boldsymbol{k}), \hat{\boldsymbol{u}}(\boldsymbol{k}'), \hat{\boldsymbol{u}}(\boldsymbol{k}'')) \right\rangle_z \\
& - 2\delta_{\boldsymbol{k},\boldsymbol{0}} \Big(\langle \hat{u}_x(\boldsymbol{0}) \rangle_z \Pi_x + \langle \hat{u}_y(\boldsymbol{0}) \rangle_z \Pi_y \Big) \\
& + \frac{\delta_{\boldsymbol{k},\boldsymbol{0}}}{Re} \Big(\partial_z \hat{u}_x(\boldsymbol{k}, z=+1) + \partial_z \hat{u}_x(\boldsymbol{k}, z=-1) \Big) \\
& - \frac{2}{Re} \left\langle (k^2+l^2)|\hat{\boldsymbol{u}}(\boldsymbol{k})|^2 + |\partial_z \hat{\boldsymbol{u}}(\boldsymbol{k})|^2 \right\rangle_z,
\end{aligned}
\tag{B.85}
$$

where we write the z-directional mean as $1/2 \int_{z=-1}^{z=+1} \cdot\, dz = \langle \cdot \rangle_z$ and the horizontal mean as $1/(L_x L_y) \int_{y=0}^{y=L_y} \int_{x=0}^{x=L_x} \cdot\, dxdy = \langle \cdot \rangle_H$.

B.5.1 Derivation

We write the Navier-Stokes equations as

$$
\partial_t \boldsymbol{u} + \boldsymbol{u} \cdot \boldsymbol{\nabla} \boldsymbol{u} = -\boldsymbol{\nabla} p + \frac{1}{Re} \boldsymbol{\nabla}^2 \boldsymbol{u} = \boldsymbol{f}(\boldsymbol{u}). \tag{B.86}
$$

Substituting the horizontal Fourier expansion of the velocity fields

$$\boldsymbol{u}(x,y,z) = \sum_{\boldsymbol{k}} \hat{\boldsymbol{u}}(\boldsymbol{k},z)e^{i\boldsymbol{k}\cdot\boldsymbol{x}} \tag{B.87}$$

into the Navier-Stokes equations;

$$\partial_t \sum_{\boldsymbol{k}} \hat{\boldsymbol{u}}(\boldsymbol{k})e^{i\boldsymbol{k}\cdot\boldsymbol{x}} + \sum_{\boldsymbol{k}',\boldsymbol{k}''} \Big(ik'\hat{u}_x(\boldsymbol{k}'') + il'\hat{u}_y(\boldsymbol{k}'') + \hat{u}_z(\boldsymbol{k}'')\partial_z \Big)\hat{\boldsymbol{u}}(\boldsymbol{k}')e^{i(\boldsymbol{k}'+\boldsymbol{k}'')\cdot\boldsymbol{x}} = \boldsymbol{f}(\boldsymbol{u}). \tag{B.88}$$

Then, multiplying $e^{-i\boldsymbol{k}\cdot x}$ by the above equations and calculating the horizontal mean give

$$\partial_t \hat{\boldsymbol{u}}(\boldsymbol{k}) = -\sum_{\boldsymbol{k}''+\boldsymbol{k}'=\boldsymbol{k}} \Big(ik'\hat{u}_x(\boldsymbol{k}'') + il'\hat{u}_y(\boldsymbol{k}'') + \hat{u}_z(\boldsymbol{k}'')\partial_z \Big)\hat{\boldsymbol{u}}(\boldsymbol{k}') + \Big\langle \boldsymbol{f}(\boldsymbol{u})e^{-i\boldsymbol{k}\cdot x} \Big\rangle_H . \tag{B.89}$$

Time derivative of the modal energy $\partial_t|\hat{\boldsymbol{u}}(\boldsymbol{k})|^2 = \hat{\boldsymbol{u}}^*(\boldsymbol{k})\cdot\partial_t\hat{\boldsymbol{u}}(\boldsymbol{k}) + \hat{\boldsymbol{u}}(\boldsymbol{k})\cdot\partial_t\hat{\boldsymbol{u}}^*(\boldsymbol{k})$ can be calculated straightforwardly;

$$\begin{aligned}\partial_t|\hat{\boldsymbol{u}}(\boldsymbol{k})|^2 = &-\sum_{\boldsymbol{k}''+\boldsymbol{k}'=\boldsymbol{k}} \hat{\boldsymbol{u}}^*(\boldsymbol{k})\cdot\Big(ik'\hat{u}_x(\boldsymbol{k}'') + il'\hat{u}_y(\boldsymbol{k}'') + \hat{u}_z(\boldsymbol{k}'')\partial_z \Big)\hat{\boldsymbol{u}}(\boldsymbol{k}') + \text{c.c.} \\ &+\hat{\boldsymbol{u}}^*(\boldsymbol{k})\cdot\Big\langle \boldsymbol{f}(\boldsymbol{u})e^{-i\boldsymbol{k}\cdot x} \Big\rangle_H + \text{c.c.}\end{aligned} \tag{B.90}$$

where c.c. denotes complex conjugate term.
Next, we consider the term $\boldsymbol{f}(\boldsymbol{u}) = -\boldsymbol{\nabla}p + \frac{1}{Re}\boldsymbol{\nabla}^2\boldsymbol{u}$ in detail. Firstly we discuss the pressure term, and then we discuss the viscous term.

Pressure term
Considering z-directional mean of the modal energy equation, the pressure term become as follows

$$\frac{1}{2}\int_{z=-1}^{z=+1} \hat{\boldsymbol{u}}(\boldsymbol{k})^*\cdot\Big\langle \boldsymbol{\nabla}p(\boldsymbol{x})e^{-i\boldsymbol{k}\cdot x} \Big\rangle_H + \hat{\boldsymbol{u}}(\boldsymbol{k})\cdot\Big\langle \boldsymbol{\nabla}p(\boldsymbol{x})e^{-i\boldsymbol{k}\cdot x} \Big\rangle_H^* dz \tag{B.91}$$

$$= 2\delta_{\boldsymbol{k},\boldsymbol{0}}\Big(\langle\hat{u}_x(\boldsymbol{0})\rangle_z\Pi_x + \langle\hat{u}_y(\boldsymbol{0})\rangle_z\Pi_y \Big). \tag{B.92}$$

In this thesis, we set $\langle\hat{u}_x\rangle_z \equiv 0$ and $\Pi_y \equiv 0$, thus the r.h.s. of the above equation is identically zero. We here derive the above equation. The horizontal

Fourier expansion of the pressure can be written $p(\boldsymbol{x}) = \sum_{\boldsymbol{k}} \hat{p}(\boldsymbol{k}, z) e^{i\boldsymbol{k}\cdot\boldsymbol{x}} + \Pi_x x + \Pi_y y$. Therefore, we have

$$\left\langle \boldsymbol{\nabla} p(\boldsymbol{x}) e^{-i\boldsymbol{k}\cdot x} \right\rangle_H = ik\hat{p}(\boldsymbol{k}, z)\boldsymbol{e}_x + il\hat{p}(\boldsymbol{k}, z)\boldsymbol{e}_y + \partial_z \hat{p}(\boldsymbol{k}, z)\boldsymbol{e}_z + \delta_{\boldsymbol{k},\boldsymbol{0}}(\Pi_x \boldsymbol{e}_x + \Pi_y \boldsymbol{e}_y). \tag{B.93}$$

where Π_x, Π_y denote the x, y-directional mean pressure gradient respectively. Thus,

$$\begin{aligned}
&\hat{\boldsymbol{u}}(\boldsymbol{k})^* \cdot \left\langle \boldsymbol{\nabla} p(\boldsymbol{x}) e^{-i\boldsymbol{k}\cdot x} \right\rangle_H + \hat{\boldsymbol{u}}(\boldsymbol{k}) \cdot \left\langle \boldsymbol{\nabla} p(\boldsymbol{x}) e^{-i\boldsymbol{k}\cdot x} \right\rangle_H^* \\
=&(ik\hat{u}_x^*(\boldsymbol{k}) + il\hat{u}_y^*(\boldsymbol{k}) + \hat{u}_z^*(\boldsymbol{k})\partial_z)\hat{p}(\boldsymbol{k}) + (-ik\hat{u}_x(\boldsymbol{k}) - il\hat{u}_y(\boldsymbol{k}) + \hat{u}_z(\boldsymbol{k})\partial_z)\hat{p}^*(\boldsymbol{k}) \\
&+ 2\delta_{\boldsymbol{k},\boldsymbol{0}}(\hat{u}_x(\boldsymbol{0})\Pi_x + \hat{u}_y(\boldsymbol{0})\Pi_y) \\
=&i\Big(k\hat{u}_x^*(\boldsymbol{k}) + l\hat{u}_y^*(\boldsymbol{k})\Big)\hat{p}(\boldsymbol{k}) - i\Big(k\hat{u}_x(\boldsymbol{k}) + l\hat{u}_y(\boldsymbol{k})\Big)\hat{p}^*(\boldsymbol{k}) \\
&+ \Big(\hat{u}_z^*\partial_z\hat{p}(\boldsymbol{k}) + \hat{u}_z(\boldsymbol{k})\partial_z\hat{p}^*(\boldsymbol{k})\Big) + 2\delta_{\boldsymbol{k},\boldsymbol{0}}(\hat{u}_x(\boldsymbol{0})\Pi_x + \hat{u}_y(\boldsymbol{0})\Pi_y).
\end{aligned} \tag{B.94}$$

Calculating z-directional mean of the above equation Eq.(B.94), the $5, 6$-th terms are as follows;

$$\begin{aligned}
&\frac{1}{2}\int_{-1}^{+1} \Big(\hat{u}_z^*\partial_z\hat{p}(\boldsymbol{k}) + \hat{u}_z(\boldsymbol{k})\partial_z\hat{p}^*(\boldsymbol{k})\Big)dz \\
&= \frac{1}{2}\Big[\hat{u}_z^*(\boldsymbol{k})\hat{p}(\boldsymbol{k}) + \hat{u}_z(\boldsymbol{k})\hat{p}^*(\boldsymbol{k})\Big]_{-1}^{+1} - \frac{1}{2}\int_{-1}^{+1} \partial_z\hat{u}_z^*\hat{p}(\boldsymbol{k}) + \partial_z\hat{u}_z(\boldsymbol{k})\hat{p}^*(\boldsymbol{k})dz \\
&= -\frac{1}{2}\int_{-1}^{+1} \Big(ik\hat{u}_x^*(\boldsymbol{k}) + il\hat{u}_y^*(\boldsymbol{k})\Big)\hat{p}(\boldsymbol{k}) - \Big(ik\hat{u}_x(\boldsymbol{k}) + il\hat{u}_y(\boldsymbol{k})\Big)\hat{p}^*(\boldsymbol{k})dz,
\end{aligned} \tag{B.95}$$

where we use the incompressible condition $(ik\hat{u}_x(\boldsymbol{k}) + il\hat{u}_y(\boldsymbol{k}) + \partial_z\hat{u}_z(\boldsymbol{k}) = 0)$ and its complex conjugate. It is found that the r.h.s. of Eq.(B.95) is the opposite sign of $1, 2, 3, 4$-th terms of z-directional mean of Eq.(B.94). Therefore, these terms cancel out and remaining terms are only the terms related to the mean pressure gradient $2\delta_{\boldsymbol{k},\boldsymbol{0}}(\langle\hat{u}_x(\boldsymbol{0})\rangle_z\Pi_x + \langle\hat{u}_y(\boldsymbol{0})\rangle_z\Pi_y)$.

Viscous term

Considering z-directional mean of the modal energy equation as above, the

viscous terms are as follows

$$\frac{1}{2}\int_{z=-1}^{z=+1}\hat{\boldsymbol{u}}(\boldsymbol{k})^*\cdot\left\langle(\boldsymbol{\nabla}^2\boldsymbol{u}(\boldsymbol{x}))e^{-i\boldsymbol{k}\cdot x}\right\rangle_H+\hat{\boldsymbol{u}}(\boldsymbol{k})\cdot\left\langle(\boldsymbol{\nabla}^2\boldsymbol{u}(\boldsymbol{x}))e^{-i\boldsymbol{k}\cdot x}\right\rangle_H^* dz$$
$$=\Big(\partial_z\hat{u}_x(\boldsymbol{k},z=+1)+\partial_z\hat{u}_x(\boldsymbol{k},z=-1)\Big)\delta_{\boldsymbol{k},\boldsymbol{0}}-2\left\langle(k^2+l^2)|\hat{\boldsymbol{u}}(\boldsymbol{k})|^2+|\partial_z\hat{\boldsymbol{u}}(\boldsymbol{k})|^2\right\rangle_z. \tag{B.96}$$

Here we derive this equation. We have

$$\left\langle(\boldsymbol{\nabla}^2\boldsymbol{u}(\boldsymbol{x}))e^{-i\boldsymbol{k}\cdot x}\right\rangle_H=\left\langle\sum_{\boldsymbol{k}'}\{-(k'^2+l'^2)\hat{\boldsymbol{u}}(\boldsymbol{k}')+\partial_z^2\hat{\boldsymbol{u}}(\boldsymbol{k}')\}e^{-i(\boldsymbol{k}-\boldsymbol{k}')\cdot x}\right\rangle_H \tag{B.97}$$
$$=-(k^2+l^2)\hat{\boldsymbol{u}}(\boldsymbol{k})+\partial_z^2\hat{\boldsymbol{u}}(\boldsymbol{k}). \tag{B.98}$$

Thus, it follows

$$\hat{\boldsymbol{u}}(\boldsymbol{k})^*\cdot\left\langle(\boldsymbol{\nabla}^2\boldsymbol{u}(\boldsymbol{x}))e^{-i\boldsymbol{k}\cdot x}\right\rangle_H+\hat{\boldsymbol{u}}(\boldsymbol{k})\cdot\left\langle(\boldsymbol{\nabla}^2\boldsymbol{u}(\boldsymbol{x}))e^{-i\boldsymbol{k}\cdot x}\right\rangle_H^* \tag{B.99}$$
$$=-2(k^2+l^2)|\hat{\boldsymbol{u}}(\boldsymbol{k})|^2+\hat{\boldsymbol{u}}^*(\boldsymbol{k})\cdot\partial_z^2\hat{\boldsymbol{u}}(\boldsymbol{k})+\hat{\boldsymbol{u}}(\boldsymbol{k})\cdot\partial_z^2\hat{\boldsymbol{u}}^*(\boldsymbol{k}). \tag{B.100}$$

Here we consider the z-directional mean of the above equation. Particularly, the 2-nd and 3-rd terms become

$$\left\langle\hat{\boldsymbol{u}}^*(\boldsymbol{k})\cdot\partial_z^2\hat{\boldsymbol{u}}(\boldsymbol{k})+\hat{\boldsymbol{u}}(\boldsymbol{k})\cdot\partial_z^2\hat{\boldsymbol{u}}^*(\boldsymbol{k})\right\rangle_z$$
$$=\frac{1}{2}\int_{-1}^{+1}\hat{\boldsymbol{u}}^*(\boldsymbol{k})\cdot\partial_z^2\hat{\boldsymbol{u}}(\boldsymbol{k})+\hat{\boldsymbol{u}}(\boldsymbol{k})\cdot\partial_z^2\hat{\boldsymbol{u}}^*(\boldsymbol{k})dz$$
$$=\frac{1}{2}\Big[\hat{\boldsymbol{u}}^*(\boldsymbol{k})\cdot\partial_z\hat{\boldsymbol{u}}(\boldsymbol{k})+\hat{\boldsymbol{u}}(\boldsymbol{k})\cdot\partial_z\hat{\boldsymbol{u}}^*(\boldsymbol{k})\Big]_{z=-1}^{z=+1}-\int_{-1}^{+1}|\partial_z\hat{\boldsymbol{u}}(\boldsymbol{k})|^2dz$$
$$=\Big(\partial_z\hat{u_x}(\boldsymbol{k},z=+1)+\partial_z\hat{u_x}(\boldsymbol{k},z=-1)\Big)\delta_{\boldsymbol{k},\boldsymbol{0}}-2\left\langle|\partial_z\hat{\boldsymbol{u}}(\boldsymbol{k})|^2\right\rangle_z. \tag{B.101}$$

As a result, we obtain Eq.(B.96). The first term represents energy injection (into $\boldsymbol{k}=\boldsymbol{0}$ mode only) thorough viscous stress on the walls, and the second term represents energy dissipation.

Mean flow interaction terms

The nonlinear terms in Eq.(B.90) are

$$-\sum_{\boldsymbol{k}''+\boldsymbol{k}'=\boldsymbol{k}}\hat{\boldsymbol{u}}^*(\boldsymbol{k})\cdot\Big(ik'\hat{u}_x(\boldsymbol{k}'')+il'\hat{u}_y(\boldsymbol{k}'')+\hat{u}_z(\boldsymbol{k}'')\partial_z\Big)\hat{\boldsymbol{u}}(\boldsymbol{k}')+\text{c.}c. \tag{B.102}$$

and we focus our attention on mean flow interaction terms (i.e. interaction with $\boldsymbol{k} = \boldsymbol{0}$ mode). Possible triad interactions with the mean flow are as follows
(i) $\boldsymbol{k}' = \boldsymbol{0}, \boldsymbol{k}'' = \boldsymbol{k}$,
(ii) $\boldsymbol{k}' = \boldsymbol{k}, \boldsymbol{k}'' = \boldsymbol{0}$.
Therefore, we write down the interaction term in the case (i) and (ii);

$$
\begin{aligned}
&- \hat{\boldsymbol{u}}^*(\boldsymbol{k}) \cdot \Big(\hat{u}_z(\boldsymbol{k}) \partial_z \Big) \hat{\boldsymbol{u}}(\boldsymbol{0}) - \hat{\boldsymbol{u}}(\boldsymbol{k}) \cdot \Big(\hat{u}_z^*(\boldsymbol{k}) \partial_z \Big) \hat{\boldsymbol{u}}^*(\boldsymbol{0}) \\
&- \hat{\boldsymbol{u}}^*(\boldsymbol{k}) \cdot \Big(ik\hat{u}_x(\boldsymbol{0}) + il\hat{u}_y(\boldsymbol{0}) + \hat{u}_z(\boldsymbol{0}) \partial_z \Big) \hat{\boldsymbol{u}}(\boldsymbol{k}) \\
&- \hat{\boldsymbol{u}}(\boldsymbol{k}) \cdot \Big(- ik\hat{u}_x^*(\boldsymbol{0}) - il\hat{u}_y^*(\boldsymbol{0}) + \hat{u}_z^*(\boldsymbol{0}) \partial_z \Big) \hat{\boldsymbol{u}}^*(\boldsymbol{k}).
\end{aligned}
$$

The Fourier coefficient of the mean flows are $\hat{u}_z(\boldsymbol{0}) = 0$ and $\hat{u}_x(\boldsymbol{0}) \in \mathbb{R}$. Therefore, the above equation become simply

$$
-2Re[\hat{\boldsymbol{u}}^*(\boldsymbol{k}) \cdot \big(\hat{u}_z(\boldsymbol{k}) \partial_z \big) \hat{\boldsymbol{u}}(\boldsymbol{0})], \tag{B.103}
$$

where $Re[z]$ denotes the real part of z.

Finally, we obtain the modal energy equation of $\boldsymbol{k}$ mode is as follows

$$
\begin{aligned}
\frac{d}{dt} \Big\langle |\hat{\boldsymbol{u}}(\boldsymbol{k})|^2 \Big\rangle_z = &- \Big\langle 2Re[\hat{\boldsymbol{u}}^*(\boldsymbol{k}) \cdot \big(\hat{u}_z(\boldsymbol{k}) \partial_z \big) \hat{\boldsymbol{u}}(\boldsymbol{0})] \Big\rangle_z \\
&- \Big\langle \sum_{\substack{\boldsymbol{k}''+\boldsymbol{k}'=\boldsymbol{k}, \\ \boldsymbol{k}' \neq \boldsymbol{0}, \boldsymbol{k}'' \neq \boldsymbol{0}}} \mathcal{N}(\hat{\boldsymbol{u}}(\boldsymbol{k}), \hat{\boldsymbol{u}}(\boldsymbol{k}'), \hat{\boldsymbol{u}}(\boldsymbol{k}'')) \Big\rangle_z \\
&- 2\delta_{\boldsymbol{k},\boldsymbol{0}} \Big(\langle \hat{u}_x(\boldsymbol{0}) \rangle_z \Pi_x + \langle \hat{u}_y(\boldsymbol{0}) \rangle_z \Pi_y \Big) \\
&+ \frac{\delta_{\boldsymbol{k},\boldsymbol{0}}}{Re} \Big(\partial_z \hat{u}_x(\boldsymbol{k}, z = +1) + \partial_z \hat{u}_x(\boldsymbol{k}, z = -1) \Big) \\
&- \frac{2}{Re} \Big\langle (k^2 + l^2) |\hat{\boldsymbol{u}}(\boldsymbol{k})|^2 + |\partial_z \hat{\boldsymbol{u}}(\boldsymbol{k})|^2 \Big\rangle_z ,
\end{aligned} \tag{B.104}
$$

where the first term of the r.h.s. is the mean flow interaction term, the second one is the other nonlinear terms, the third one is the mean pressure gradient and volume flux term which is identically zero in this thesis, the forth one is the energy injection term from the walls, and the fifth one is the energy dissipation term.

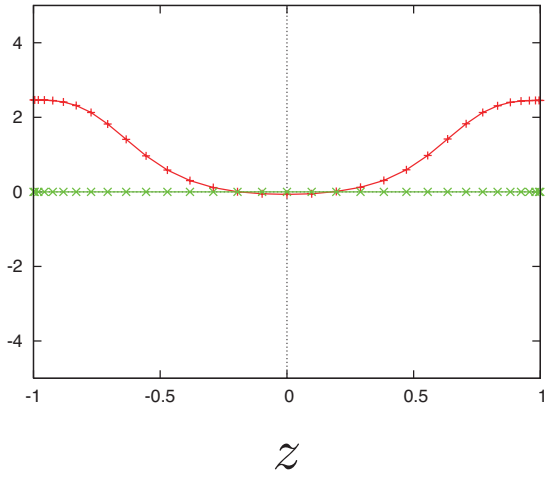

Fig. B.11: Comparison between the wall-nomal shear of the streamwise mean velocity ($\partial_z \hat{u_x}(\mathbf{0})$) and that of the spanwise mean velocity ($\partial_z \hat{u_y}(\mathbf{0})$) to check the assumption $\partial_z \hat{u_x}(\mathbf{0}) \gg \partial_z \hat{u_y}(\mathbf{0})$. The red line with + sign denotes $\partial_z \hat{u_x}(\mathbf{0})$ and the green line with $\times$ sign denote $\partial_z \hat{u_y}(\mathbf{0})$ at $t = 2730$. These profiles appear to be almost the same during the regeneration cycle.

B.5.2 Approximation of mean flow interaction term

Let us consider an assumption that the wall-nomal shear of the streamwise mean velocity is larger than that of the spanwise mean velocityas

$$\partial_z \hat{u_x}(\mathbf{0}) \gg \partial_z \hat{u_y}(\mathbf{0}), \tag{B.105}$$

which is found to be reasonable by checking numerical simulations (see Fig.B.11). Under this assumption, we have

$$-2Re[\hat{\boldsymbol{u}}^*(\boldsymbol{k}) \cdot \big(\hat{u}_z(\boldsymbol{k})\partial_z\big)\hat{\boldsymbol{u}}(\mathbf{0})] \simeq -2\ Re[\hat{u_x}^*(\boldsymbol{k})\hat{u}_z(\boldsymbol{k})]\ \partial_z \hat{u_x}(\mathbf{0}), \tag{B.106}$$

which indicates that the energy injection via nonlinear interaction from the mean flow to the $\boldsymbol{k}$ mode depends on the real part of the term $\hat{u_x}^*(\boldsymbol{k})\hat{u}_z(\boldsymbol{k})\partial_z \hat{u_x}(\mathbf{0})$.

B.5.3 Evolution equation of streak modal energy

Here we refer to the Fourier coefficient $\hat{\boldsymbol{u}}(\boldsymbol{k}_s)$ $\big(\boldsymbol{k}_s = (0,1)\big)$ as *streak mode* and $\hat{\boldsymbol{u}}(\boldsymbol{k}_m)$ $\big(\boldsymbol{k}_m = (1,0)\big)$ as *meandering mode*. From Eq.(B.85), the evolution

equation of the streak modal energy is

$$\begin{aligned}\frac{d}{dt}\left\langle|\hat{\boldsymbol{u}}(\boldsymbol{k}_s)|^2\right\rangle_z &= -\left\langle 2Re[\hat{\boldsymbol{u}}^*(\boldsymbol{k}_s)\cdot\big(\hat{u}_z(\boldsymbol{k}_s)\partial_z\big)\hat{\boldsymbol{u}}(\boldsymbol{0})]\right\rangle_z \\ &\quad -\left\langle \sum_{\substack{\boldsymbol{k}''+\boldsymbol{k}'=\boldsymbol{k}_s,\\ \boldsymbol{k}'\neq\boldsymbol{0},\boldsymbol{k}''\neq\boldsymbol{0}}} \mathcal{N}(\hat{\boldsymbol{u}}(\boldsymbol{k}_s),\hat{\boldsymbol{u}}(\boldsymbol{k}'),\hat{\boldsymbol{u}}(\boldsymbol{k}''))\right\rangle_z \\ &\quad -\frac{2}{Re}\left\langle \beta^2|\hat{\boldsymbol{u}}(\boldsymbol{k}_s)|^2+|\partial_z\hat{\boldsymbol{u}}(\boldsymbol{k}_s)|^2\right\rangle_z, \end{aligned} \tag{B.107}$$

where $\beta = 2\pi/L_y$. The first term of the r.h.s. of Eq.(B.107) is the nonlinear interaction term between the streak mode and the mean flows, the second one is the other nonlinear terms, and the third one is the energy dissipation term.

Interaction terms with the meandering mode

Next, we consider 'the other nonlinear terms' (the second term in the r.h.s. of Eq.(B.107) in more detail. Particularly, we focus our attention on the interaction terms with the meandering mode (i.e. $\hat{\boldsymbol{u}}(\boldsymbol{k}_m)$, $\hat{\boldsymbol{u}}(-\boldsymbol{k}_m)=\hat{\boldsymbol{u}}^*(\boldsymbol{k}_m)$) and pick up them so that the triad interaction $\boldsymbol{k}_s = \boldsymbol{k}' + \boldsymbol{k}''$ holds. Such possible interaction terms are as follows
(i) $\boldsymbol{k}' = \boldsymbol{k}_m = (1,0)$, $\boldsymbol{k}'' = \boldsymbol{k}_{ob-} = (-1,1)$,
(ii) $\boldsymbol{k}' = \boldsymbol{k}_{ob-} = (-1,1)$, $\boldsymbol{k}'' = \boldsymbol{k}_m = (1,0)$,
(iii) $\boldsymbol{k}' = -\boldsymbol{k}_m = (-1,0)$, $\boldsymbol{k}'' = \boldsymbol{k}_{ob+} = (1,1)$,
(iv) $\boldsymbol{k}' = \boldsymbol{k}_{ob+} = (1,1)$, $\boldsymbol{k}'' = -\boldsymbol{k}_m = (-1,0)$.
'The other nonlinear terms' are

$$-\sum_{\substack{\boldsymbol{k}''+\boldsymbol{k}'=\boldsymbol{k}_s,\\ \boldsymbol{k}'\neq\boldsymbol{0},\boldsymbol{k}''\neq\boldsymbol{0}}} \hat{\boldsymbol{u}}^*(\boldsymbol{k})\cdot\left(ik'\hat{u}_x(\boldsymbol{k}'')+il'\hat{u}_y(\boldsymbol{k}'')+\hat{u}_z(\boldsymbol{k}'')\partial_z\right)\hat{\boldsymbol{u}}(\boldsymbol{k}')+\text{c.}c. \tag{B.108}$$

and thus, we write the interaction terms in the order of the case (i), (ii), (iii),

(iv),

$$- \hat{\boldsymbol{u}}^*(\boldsymbol{k}_s) \cdot \Big(i\alpha \hat{u}_x(\boldsymbol{k}_{ob-}) + \hat{u}_z(\boldsymbol{k}_{ob-})\partial_z \Big) \hat{\boldsymbol{u}}(\boldsymbol{k}_m) + \text{c.}c. \tag{B.109}$$

$$- \hat{\boldsymbol{u}}^*(\boldsymbol{k}_s) \cdot \Big(- i\alpha \hat{u}_x(\boldsymbol{k}_m) + i\beta \hat{u}_y(\boldsymbol{k}_m) + \hat{u}_z(\boldsymbol{k}_m)\partial_z \Big) \hat{\boldsymbol{u}}(\boldsymbol{k}_{ob-}) + \text{c.}c. \tag{B.110}$$

$$- \hat{\boldsymbol{u}}^*(\boldsymbol{k}_s) \cdot \Big(- i\alpha \hat{u}_x(\boldsymbol{k}_{ob+}) + \hat{u}_z(\boldsymbol{k}_{ob+})\partial_z \Big) \hat{\boldsymbol{u}}^*(\boldsymbol{k}_m) + \text{c.}c. \tag{B.111}$$

$$- \hat{\boldsymbol{u}}^*(\boldsymbol{k}_s) \cdot \Big(i\alpha \hat{u}_x^*(\boldsymbol{k}_m) + i\beta \hat{u}_y^*(\boldsymbol{k}_m) + \hat{u}_z^*(\boldsymbol{k}_m)\partial_z \Big) \hat{\boldsymbol{u}}(\boldsymbol{k}_{ob+}) + \text{c.}c., \tag{B.112}$$

where $\alpha = 2\pi/L_x$.
Therefore, we obtain the streak modal energy equation as follows;

$$\begin{aligned}
\frac{d}{dt}\Big\langle |\hat{\boldsymbol{u}}(\boldsymbol{k}_s)|^2 \Big\rangle_z = &- \Big\langle 2Re\Big[\hat{\boldsymbol{u}}^*(\boldsymbol{k}_s) \cdot \big(\hat{u}_z(\boldsymbol{k}_s)\partial_z \big) \hat{\boldsymbol{u}}(\boldsymbol{0}) \Big] \Big\rangle_z \\
&- \Big\langle 2Re\Big[\hat{\boldsymbol{u}}^*(\boldsymbol{k}_s) \cdot (i\alpha \hat{u}_x(\boldsymbol{k}_{ob-}) + \hat{u}_z(\boldsymbol{k}_{ob-})\partial_z) \hat{\boldsymbol{u}}(\boldsymbol{k}_m) \Big] \Big\rangle_z \\
&- \Big\langle 2Re\Big[\hat{\boldsymbol{u}}^*(\boldsymbol{k}_s) \cdot \big(- i\alpha \hat{u}_x(\boldsymbol{k}_m) + i\beta \hat{u}_y(\boldsymbol{k}_m) + \hat{u}_z(\boldsymbol{k}_m)\partial_z \big) \hat{\boldsymbol{u}}(\boldsymbol{k}_{ob-}) \Big] \Big\rangle_z \\
&- \Big\langle 2Re\big[\hat{\boldsymbol{u}}^*(\boldsymbol{k}_s) \cdot \big(- i\alpha \hat{u}_x(\boldsymbol{k}_{ob+}) + \hat{u}_z(\boldsymbol{k}_{ob+})\partial_z \big) \hat{\boldsymbol{u}}^*(\boldsymbol{k}_m) \big] \Big\rangle_z \\
&- \Big\langle 2Re\big[\hat{\boldsymbol{u}}^*(\boldsymbol{k}_s) \cdot \big(i\alpha \hat{u}_x^*(\boldsymbol{k}_m) + i\beta \hat{u}_y^*(\boldsymbol{k}_m) + \hat{u}_z^*(\boldsymbol{k}_m)\partial_z \big) \hat{\boldsymbol{u}}(\boldsymbol{k}_{ob+}) \big] \Big\rangle_z \\
&- \Big\langle \sum_{\substack{\boldsymbol{k}''+\boldsymbol{k}'=\boldsymbol{k}_s, \\ \boldsymbol{k}'\neq\boldsymbol{0}, \boldsymbol{k}''\neq\boldsymbol{0} \\ \boldsymbol{k}'\neq\pm\boldsymbol{k}_m, \boldsymbol{k}''\neq\pm\boldsymbol{k}_m,}} \mathcal{N}'(\hat{\boldsymbol{u}}(\boldsymbol{k}_s), \hat{\boldsymbol{u}}(\boldsymbol{k}'), \hat{\boldsymbol{u}}(\boldsymbol{k}'')) \Big\rangle_z \\
&- \frac{2}{Re}\Big\langle \beta^2 |\hat{\boldsymbol{u}}(\boldsymbol{k}_s)|^2 + |\partial_z \hat{\boldsymbol{u}}(\boldsymbol{k}_s)|^2 \Big\rangle_z,
\end{aligned} \tag{B.113}$$

where the first term of the r.h.s. is the *mean flow-streak* interaction term, the second to the fifth terms are the *meandering-streak* interaction terms, the sixth terms are the other nonlinear terms, and the seventh term is the energy dissipation term.

B.6 Physical interpretation of streak reformation

In §3.5.2, we discussed the streak reformation mechanism and found that the *mean flow interaction* reforms the streaks, by using budget analysis of the modal energy equation Eq.(3.16);

$$\begin{aligned}\frac{d}{dt}\left\langle |\hat{\boldsymbol{u}}(\boldsymbol{k}_s)|^2 \right\rangle_z \simeq & -\left\langle 2Re[\hat{u}_x^*(\boldsymbol{k}_s)\cdot\big(\hat{u}_z(\boldsymbol{k}_s)\partial_z\big)\hat{u}_x(\boldsymbol{0})]\right\rangle_z \\ & -\left\langle \sum_{\substack{\boldsymbol{k}''+\boldsymbol{k}'=\boldsymbol{k}_s,\\ \boldsymbol{k}'\neq\boldsymbol{0},\boldsymbol{k}''\neq\boldsymbol{0}}} \mathcal{N}(\hat{\boldsymbol{u}}(\boldsymbol{k}_s),\hat{\boldsymbol{u}}(\boldsymbol{k}'),\hat{\boldsymbol{u}}(\boldsymbol{k}''))\right\rangle_z \\ & -\frac{2}{Re}\left\langle \beta^2|\hat{\boldsymbol{u}}(\boldsymbol{k}_s)|^2+|\partial_z\hat{\boldsymbol{u}}(\boldsymbol{k}_s)|^2\right\rangle_z \end{aligned} \tag{B.114}$$

where we used the approximation in §B.5.2. Considering the components of the above equation, the mean flow interaction term appears *only* in x-directional component $\hat{u}_x(\boldsymbol{k}_s)$:

$$\begin{aligned}\frac{d}{dt}\left\langle |\hat{u}_x(\boldsymbol{k}_s)|^2 \right\rangle_z = & -\left\langle 2Re[\hat{u}_x^*(\boldsymbol{k}_s)\cdot\big(\hat{u}_z(\boldsymbol{k}_s)\partial_z\big)\hat{u}_x(\boldsymbol{0})]\right\rangle_z \\ & -\left\langle \sum_{\substack{\boldsymbol{k}''+\boldsymbol{k}'=\boldsymbol{k}_s,\\ \boldsymbol{k}'\neq\boldsymbol{0},\boldsymbol{k}''\neq\boldsymbol{0}}} \mathcal{N}_x(\hat{\boldsymbol{u}}(\boldsymbol{k}_s),\hat{\boldsymbol{u}}(\boldsymbol{k}'),\hat{\boldsymbol{u}}(\boldsymbol{k}''))\right\rangle_z \\ & -\frac{2}{Re}\left\langle \beta^2|\hat{u}_x(\boldsymbol{k}_s)|^2+|\partial_z\hat{u}_x(\boldsymbol{k}_s)|^2\right\rangle_z . \end{aligned} \tag{B.115}$$

Therefore, the energy transfers from the mean flows not to the y, z-directional components $\hat{u}_y(\boldsymbol{k}_s), \hat{u}_z(\boldsymbol{k}_s)$ but to the x-directional component $\hat{u}_x(\boldsymbol{k}_s)$. Actually, during the reformation period of the streaks (the phase(ii)), $\langle|\hat{u}_x(\boldsymbol{k}_s)|^2\rangle_z$ increases while $\langle|\hat{u}_y(\boldsymbol{k}_s)|^2\rangle_z, \langle|\hat{u}_z(\boldsymbol{k}_s)|^2\rangle_z$ remain almost constant or decrease (see Fig.B.12).

Here, we consider the physical interpretation of the mean flow interaction term
$-\langle 2Re[\hat{u}_x^*(\boldsymbol{k}_s)\cdot\big(\hat{u}_z(\boldsymbol{k}_s)\partial_z\big)\hat{u}_x(\boldsymbol{0})]\rangle_z$. In the case of the streak mode, a relation $\langle|\hat{\omega}_z(\boldsymbol{k}_s)|^2\rangle_z = \beta\langle|\hat{u}_x(\boldsymbol{k}_s)|^2\rangle_z$ holds[6]. Hence, we here focus on the z-component

[6]Let us consider the velocity field consisting of the streak mode only $\boldsymbol{u}^s(\boldsymbol{x}) = 2Re[\hat{\boldsymbol{u}}(\boldsymbol{k}_s,z)e^{i\boldsymbol{k}_s\cdot\boldsymbol{x}}] = 2Re[\hat{\boldsymbol{u}}(\boldsymbol{k}_s,z)e^{i\beta y}]$ ($\beta = 2\pi/L_y$). Vorticity defined by the veloc-

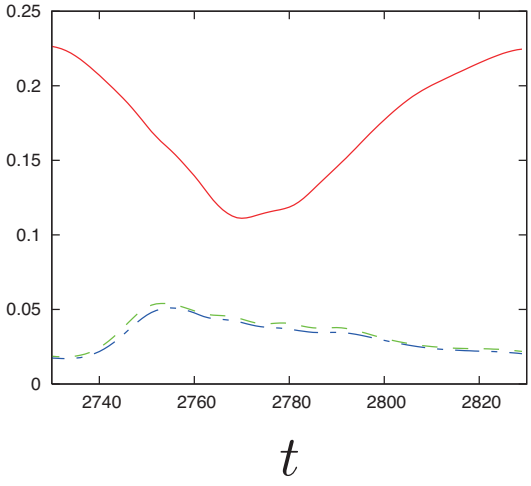

Fig. B.12: Modal energy of each directional components of the velocity consisting of the streak mode during a single regeneration cycle. The red solid line denotes x-directional component $\langle|\hat{u}_x(\boldsymbol{k}_s)|^2\rangle_z$, the green dash line denotes y-directional component $\langle|\hat{u}_y(\boldsymbol{k}_s)|^2\rangle_z$, and the blue dashed-dotted line denotes z-directional component $\langle|\hat{u}_z(\boldsymbol{k}_s)|^2\rangle_z$.

of the vorticity $\hat{\omega}_z(\boldsymbol{k}_s)$ instead of the x-component $\hat{u}_x(\boldsymbol{k}_s)$ of the streak mode. We can obtain the 'modal enstrophy' equation of the z-component of the

ity field ($\boldsymbol{\omega}^s = \boldsymbol{\nabla} \times \boldsymbol{u}^s$) is

$$\omega_x^s = \frac{\partial u_z^s}{\partial y} - \frac{\partial u_y^s}{\partial z}, \quad \omega_y^s = \frac{\partial u_x^s}{\partial z} - \frac{\partial u_z^s}{\partial x} = \frac{\partial u_x^s}{\partial z}, \tag{B.116}$$

$$\begin{aligned}\omega_z^s &= \frac{\partial u_y^s}{\partial x} - \frac{\partial u_x^s}{\partial y} \\ &= -\frac{\partial u_x^s}{\partial y} \\ &= -2Re[i\beta\hat{u}_x(\boldsymbol{k}_s, z)e^{i\beta y}] \\ &= -2\beta Re[\hat{u_x}(\boldsymbol{k}_s, z)e^{i(\beta y+\pi/2)}] \\ &= -\beta u_x^s\big(x, y + \frac{\pi}{2\beta}, z\big).\end{aligned} \tag{B.117}$$

Particularly, in the z-directional components, a simple relation between L^2-norms of the coefficients holds as $||\omega_z^s(x,y,z)||_{L_2} = ||\beta u_x^s\big(x, y + \frac{\pi}{2\beta}, z\big)||_{L_2} = \beta||u_x^s(x,y,z)||_{L_2}$.

vorticity $\hat{\omega}_z(\boldsymbol{k}_s)$ from the vorticity equation;

$$\begin{aligned}\frac{d}{dt}\left\langle |\hat{\omega}_z(\boldsymbol{k}_s)|^2 \right\rangle_z &= 2\left\langle Re\Big[\hat{\omega}_z^*(\boldsymbol{k}_s)\ \hat{\omega}_y(\boldsymbol{0})\Big(i\beta\hat{u}_z(\boldsymbol{k}_s)\Big)\Big]\right\rangle_z \\ &\quad -\left\langle \sum_{\substack{\boldsymbol{k}''+\boldsymbol{k}'=\boldsymbol{k}_s,\\ \boldsymbol{k}'\neq\boldsymbol{0},\boldsymbol{k}''\neq\boldsymbol{0}}} \mathcal{N}_\omega(\hat{\boldsymbol{\omega}}(\boldsymbol{k}_s),\hat{\boldsymbol{\omega}}(\boldsymbol{k}'),\hat{\boldsymbol{\omega}}(\boldsymbol{k}'')) \right\rangle_z \\ &\quad -\frac{2}{Re}\left\langle \beta^2|\hat{\omega}_z(\boldsymbol{k}_s)|^2 + |\partial_z\hat{\omega}_z(\boldsymbol{k}_s)|^2 \right\rangle_z \end{aligned} \tag{B.118}$$

(see §B.7). The mean flow interaction term of the above equation,

$$2\left\langle Re\Big[\hat{\omega}_z^*(\boldsymbol{k}_s)\ \hat{\omega}_y(\boldsymbol{0})\Big(i\beta\hat{u}_z(\boldsymbol{k}_s)\Big)\Big]\right\rangle_z, \tag{B.119}$$

originates from the *tilting term* in the vorticity equation: $\omega_y\partial_y u_z$, i.e. tilting of the y-directional component of the mean flow vorticity toward z-directional component of the vorticity through the nonlinear interaction.

Substituting the relation between the coefficients of the streak mode $\hat{\omega}_z(\boldsymbol{k}_s,z) = -i\beta\hat{u}_x(\boldsymbol{k}_s,z)$ into the above modal enstrophy equation;

$$\beta^2\frac{d}{dt}\left\langle |\hat{u}_x(\boldsymbol{k}_s)|^2 \right\rangle_z = 2\left\langle Re\Big[i\beta\hat{u}_x^*(\boldsymbol{k}_s)\Big(i\beta\partial_z\hat{u}_x(\boldsymbol{0})\Big)\hat{u}_z(\boldsymbol{k}_s)\Big]\right\rangle_z \tag{B.120}$$

$$-\left\langle \sum_{\substack{\boldsymbol{k}''+\boldsymbol{k}'=\boldsymbol{k}_s,\\ \boldsymbol{k}'\neq\boldsymbol{0},\boldsymbol{k}''\neq\boldsymbol{0}}} \mathcal{N}_\omega(\hat{\boldsymbol{\omega}}(\boldsymbol{k}_s),\hat{\boldsymbol{\omega}}(\boldsymbol{k}'),\hat{\boldsymbol{\omega}}(\boldsymbol{k}'')) \right\rangle_z \tag{B.121}$$

$$-\frac{2\beta^2}{Re}\left\langle \beta^2|\hat{u}_x(\boldsymbol{k}_s)|^2 + |\partial_z\hat{u}_x(\boldsymbol{k}_s)|^2 \right\rangle_z, \tag{B.122}$$

we have the modal energy equation Eq.(B.115) by multiplying $1/\beta^2$. Thus, the mean flow interaction term in the modal *energy* equation Eq.(B.115) corresponds to the vortex tilting term in the modal *enstrophy* equation Eq.(B.118). In other words, in the enstrophy equation, the vortex tilting plays an important role for growth of $\langle|\hat{\omega}_z(\boldsymbol{k}_s)|^2\rangle_z$, which implies the growth of the streak mode $\langle|\hat{u}_x(\boldsymbol{k}_s)|^2\rangle_z$ through the relation $\langle|\hat{\omega}_z(\boldsymbol{k}_s)|^2\rangle_z = \beta\langle|\hat{u}_x(\boldsymbol{k}_s)|^2\rangle_z$. To summarize, the physical interpretation of the mean flow interaction is the tilting of the mean flow vorticity.

B.6.1 Relation to lift-up mechanism

Here, we briefly discuss relation between the vortex tilting mechanism described above and so-called lift-up mechanism. Lift-up mechanism illustrates

the formation of the streaks by the streamwise vortex in a x-independent flow. The evolution equation of the streamwise velocity in the x-independent (i.e. $\partial_x = 0$) is as follows :

$$\partial_t u_x \sim -u_y \partial_y u_x - u_z \partial_z u_x = (\boldsymbol{u}_\perp \cdot \boldsymbol{\nabla}_\perp) u_x, \tag{B.123}$$

where we do not consider the viscous term and $\perp$ denotes a physical quantity in a cross-streamwise plane (a plane perpendicular to the streamwise direction, i.e. y-z plane). Thus, the streamwise velocity contour u_x can be a *passive scalar* advected by the streamwise vortex in the cross-streamwise plane.

In order to consider the relation between the two mechanisms, we use $\omega_y = \partial_z u_x$ and $\omega_z = -\partial_y u_x$ under the assumption that the flow is x-independent (i.e. $\partial_x = 0$). Spanwise derivative (∂_y) of the above equation (B.123) gives

$$\partial_t \omega_z = -\omega_z \partial_y u_y - u_y \partial_y \omega_z + \omega_y \partial_y u_z + u_z \partial_y \omega_y \tag{B.124}$$

Using incompressible conditions, we have simply a vorticity equation :

$$\partial_t \omega_z = -\boldsymbol{u}_\perp \cdot \boldsymbol{\nabla}_\perp \omega_z + \boldsymbol{\omega}_\perp \cdot \boldsymbol{\nabla}_\perp u_z. \tag{B.125}$$

In the tilting mechanism we described above, the vorticity tilting term $\omega_y \partial_y u_z$ is important (i.e. $\partial_t \omega_z \sim \omega_y \partial_y u_z$). More precisely, only the mean flow interaction of the vorticity tilting term $\omega_y \partial_y u_z$ is important. Therefore, the difference between the two mechanisms is, at least, the three terms $-\omega_z \partial_y u_y - u_y \partial_y \omega_z + u_z \partial_y \omega_y$. in Eq.(B.123).

B.7 Derivation of evolution equation of modal enstrophy

In this section, we derive evolution equation of 'modal enstrophy'[7] $\langle |\hat{\omega}_z(\boldsymbol{k})|^2 \rangle_z$, i.e. z-directional mean of square amplitude of wall-normal Fourier coefficient $\hat{\omega}_z(\boldsymbol{k})$ (hereafter we write $\hat{\boldsymbol{\omega}}(\boldsymbol{k})$ as $\hat{\boldsymbol{\omega}}(\boldsymbol{k}, z)$ for simplicity), which is as follows

[7] More precisely, it would be better to refer to it as 'twice of modal enstrophy'.

:

$$\frac{\partial}{\partial t}\left\langle |\hat{\omega}_z(\boldsymbol{k})|^2 \right\rangle_z = 2\left\langle Re\left[-ik\hat{\omega}_z^*(\boldsymbol{k})\frac{\partial \hat{u}_y}{\partial z}(\boldsymbol{0})\hat{u}_z(\boldsymbol{k}) + il\hat{\omega}_z^*(\boldsymbol{k})\frac{\partial \hat{u}_x}{\partial z}(\boldsymbol{0})\hat{u}_z(\boldsymbol{k})\right]\right\rangle_z + \left\langle \sum_{\substack{\boldsymbol{k''}+\boldsymbol{k'}=\boldsymbol{k},\\ \boldsymbol{k'}\neq\boldsymbol{0},\boldsymbol{k''}\neq\boldsymbol{0}}} \mathcal{N}(\hat{\boldsymbol{\omega}}(\boldsymbol{k}),\hat{\boldsymbol{\omega}}(\boldsymbol{k'}),\hat{\boldsymbol{\omega}}(\boldsymbol{k''}))\right\rangle_z - \frac{2}{Re}\left\langle (k^2+l^2)|\hat{\omega}_z(\boldsymbol{k})|^2 + |\partial_z\hat{\omega}_z(\boldsymbol{k})|^2 \right\rangle_z. \tag{B.126}$$

Wall-normal (z-directional) component of vorticity equation is

$$\frac{\partial \omega_z}{\partial t} = -\boldsymbol{u}\cdot\boldsymbol{\nabla}\omega_z + \boldsymbol{\omega}\cdot\boldsymbol{\nabla}u_z + \frac{1}{Re}\boldsymbol{\nabla}^2\omega_z. \tag{B.127}$$

Substituting the Fourier expansion of the wall-normal vorticity field

$$\omega_z(x,y,z) = \sum_{\boldsymbol{k}} \hat{\omega}_z(\boldsymbol{k},z)e^{i\boldsymbol{k}\cdot\boldsymbol{x}} \tag{B.128}$$

into the above equation and picking up $\boldsymbol{k}$ mode ($\langle\ \cdot\ e^{-i\boldsymbol{k}\cdot\boldsymbol{x}}\rangle_H$), we have

$$\begin{aligned}\partial_t\hat{\omega}_z(\boldsymbol{k}) = &-\sum_{\boldsymbol{k'}+\boldsymbol{k''}=\boldsymbol{k}}\Big(ik'\hat{u}_x(\boldsymbol{k''}) + il'\hat{u}_y(\boldsymbol{k''}) + \hat{u}_z(\boldsymbol{k''})\partial_z\Big)\hat{\omega}_z(\boldsymbol{k'})\\ &+\sum_{\boldsymbol{k'}+\boldsymbol{k''}=\boldsymbol{k}}\Big(ik'\hat{\omega}_x(\boldsymbol{k''}) + il'\hat{\omega}_y(\boldsymbol{k''}) + \hat{\omega}_z(\boldsymbol{k''})\partial_z\Big)\hat{u}_z(\boldsymbol{k'})\\ &+\frac{1}{Re}\Big(-(k^2+l^2)\hat{\omega}_z(\boldsymbol{k}) + \partial_z^2\hat{\omega}_z(\boldsymbol{k})\Big).\end{aligned} \tag{B.129}$$

Particularly, we focus our attention on the interaction terms with the mean flows, and therefore we pick up them so that the triad interaction $\boldsymbol{k} = \boldsymbol{k'} + \boldsymbol{k''}$ holds. Such possible interaction terms are as follows :
(i) $\boldsymbol{k'} = \boldsymbol{0},\ \boldsymbol{k''} = \boldsymbol{k}$
(ii) $\boldsymbol{k''} = \boldsymbol{0},\ \boldsymbol{k'} = \boldsymbol{k}$.
From the first term of the nonlinear terms, we have

$$\Big(ik\hat{u}_x(\boldsymbol{0}) + il\hat{u}_y(\boldsymbol{0})\Big)\hat{\omega}_z(\boldsymbol{k}), \tag{B.130}$$

and from the second term of the nonlinear terms, we have

$$\Big(ik\hat{\omega}_x(\boldsymbol{0}) + il\hat{\omega}_y(\boldsymbol{0})\Big)\hat{u}_z(\boldsymbol{k}), \tag{B.131}$$

where we use the fact that $\hat{u}_z(\boldsymbol{0}) \equiv 0$, $\hat{\omega}_z(\boldsymbol{0}) \equiv 0$.

Summarizing the above calculation, we obtain

$$\begin{aligned}
\partial_t \hat{\omega}_z(\boldsymbol{k}) = &- \Big(ik\hat{u}_x(\boldsymbol{0}) + il\hat{u}_y(\boldsymbol{0})\Big)\hat{\omega}_z(\boldsymbol{k}) \\
&+ \Big(ik\hat{\omega}_x(\boldsymbol{0}) + il\hat{\omega}_y(\boldsymbol{0})\Big)\hat{u}_z(\boldsymbol{k}) \\
&- \sum_{\substack{\boldsymbol{k}''+\boldsymbol{k}'=\boldsymbol{k}, \\ \boldsymbol{k}'\neq\boldsymbol{0},\boldsymbol{k}''\neq\boldsymbol{0}}} \Big(ik'\hat{u}_x(\boldsymbol{k}'') + il'\hat{u}_y(\boldsymbol{k}'') + \hat{u}_z(\boldsymbol{k}'')\partial_z\Big)\hat{\omega}_z(\boldsymbol{k}') \\
&+ \sum_{\substack{\boldsymbol{k}''+\boldsymbol{k}'=\boldsymbol{k}, \\ \boldsymbol{k}'\neq\boldsymbol{0},\boldsymbol{k}''\neq\boldsymbol{0}}} \Big(ik'\hat{\omega}_x(\boldsymbol{k}'') + il'\hat{\omega}_y(\boldsymbol{k}'') + \hat{\omega}_z(\boldsymbol{k}'')\partial_z\Big)\hat{u}_z(\boldsymbol{k}') \\
&+ \frac{1}{Re}\Big(- (k^2+l^2)\hat{\omega}_z(\boldsymbol{k}) + \partial_z^2\hat{\omega}_z(\boldsymbol{k})\Big),
\end{aligned} \tag{B.132}$$

which leads to the evolution equation of the 'modal enstrophy' as follows :

$$\begin{aligned}
\partial_t|\hat{\omega}_z(\boldsymbol{k})|^2 = &- \hat{\omega}_z^*(\boldsymbol{k})\Big(ik\hat{u}_x(\boldsymbol{0}) + il\hat{u}_y(\boldsymbol{0})\Big)\hat{\omega}_z(\boldsymbol{k}) + \text{c.}c. \\
&+ \hat{\omega}_z^*(\boldsymbol{k})\Big(ik\hat{\omega}_x(\boldsymbol{0}) + il\hat{\omega}_y(\boldsymbol{0})\Big)\hat{u}_z(\boldsymbol{k}) + \text{c.}c. \\
&- \sum_{\substack{\boldsymbol{k}''+\boldsymbol{k}'=\boldsymbol{k}, \\ \boldsymbol{k}'\neq\boldsymbol{0},\boldsymbol{k}''\neq\boldsymbol{0}}} \mathcal{N}_\omega(\hat{\boldsymbol{\omega}}(\boldsymbol{k}), \hat{\boldsymbol{\omega}}(\boldsymbol{k}'), \hat{\boldsymbol{\omega}}(\boldsymbol{k}'')) \\
&+ \frac{1}{Re}\Big(- (k^2+l^2)\hat{\omega}_z(\boldsymbol{k}) + \partial_z^2\hat{\omega}_z(\boldsymbol{k})\Big).
\end{aligned} \tag{B.133}$$

From $\hat{u}_x(\boldsymbol{0}), \hat{u}_y(\boldsymbol{0}) \in \mathbb{R}$, it follows that the first term of r.h.s. is canceled out with its complex conjugate term.

Finally, calculating z-directional mean, we have Eq.(B.126), where we used the facts that $\hat{\omega}_z(\boldsymbol{k}, z=\pm 1) \equiv 0$ and $\hat{\omega}_x(\boldsymbol{0}) = -\partial_z\hat{u}_y(\boldsymbol{0})$, $\hat{\omega}_y(\boldsymbol{0}) = \partial_z\hat{u}_x(\boldsymbol{0})$.

In the case of the streak mode $\boldsymbol{k} = \boldsymbol{k}_s = (0,1)$, the above equation become

$$\begin{aligned}
\frac{d}{dt}\Big\langle |\hat{\omega}_z(\boldsymbol{k}_s)|^2 \Big\rangle_z = &\, 2\Big\langle Re\Big[\hat{\omega}_z^*(\boldsymbol{k}_s)\Big(i\beta\partial_z\hat{u}_x(\boldsymbol{0})\Big)\hat{u}_z(\boldsymbol{k}_s)\Big]\Big\rangle_z \\
&- \Big\langle \sum_{\substack{\boldsymbol{k}''+\boldsymbol{k}'=\boldsymbol{k}_s, \\ \boldsymbol{k}'\neq\boldsymbol{0},\boldsymbol{k}''\neq\boldsymbol{0}}} \mathcal{N}_\omega(\hat{\boldsymbol{\omega}}(\boldsymbol{k}_s), \hat{\boldsymbol{\omega}}(\boldsymbol{k}'), \hat{\boldsymbol{\omega}}(\boldsymbol{k}'')) \Big\rangle_z \\
&- \frac{2}{Re}\Big\langle \beta^2|\hat{\omega}_z(\boldsymbol{k}_s)|^2 + |\partial_z\hat{\omega}_z(\boldsymbol{k}_s)|^2 \Big\rangle_z .
\end{aligned} \tag{B.134}$$

Derivation from the 'modal energy' equation (in the case of $\boldsymbol{k} = \boldsymbol{k}_s$)

As Eq.(B.104), z-directional mean of the modal energy equation of streamwise (x-directional) component is given by

$$\frac{d}{dt}\left\langle |\hat{u_x}(\boldsymbol{k})|^2 \right\rangle_z = -\left\langle 2Re\Big[\hat{u_x}^*(\boldsymbol{k}) \cdot \big(\hat{u}_z(\boldsymbol{k})\partial_z\big)\hat{u_x}(\boldsymbol{0})\Big] \right\rangle_z \tag{B.135}$$

$$-\left\langle \sum_{\substack{\boldsymbol{k''}+\boldsymbol{k'}=\boldsymbol{k},\\ \boldsymbol{k'}\neq\boldsymbol{0},\boldsymbol{k''}\neq\boldsymbol{0}}} \mathcal{N}(\hat{u_x}(\boldsymbol{k}), \hat{u_m}(\boldsymbol{k'}), \hat{u_n}(\boldsymbol{k''})) \right\rangle_z \tag{B.136}$$

$$-\left\langle 2Re\big[ik\hat{u}_x(\boldsymbol{k})\hat{p}(\boldsymbol{k})\big] \right\rangle_z - 2\delta_{\boldsymbol{k},\boldsymbol{0}}\langle \hat{u}_x(\boldsymbol{0})\rangle_z \Pi_x \tag{B.137}$$

$$+\frac{\delta_{\boldsymbol{k},\boldsymbol{0}}}{Re}\Big(\partial_z\hat{u}_x(\boldsymbol{k}, z=+1) + \partial_z\hat{u}_x(\boldsymbol{k}, z=-1)\Big) \tag{B.138}$$

$$-\frac{2}{Re}\left\langle (k^2+l^2)|\hat{u_x}(\boldsymbol{k})|^2 + |\partial_z\hat{u_x}(\boldsymbol{k})|^2 \right\rangle_z. \tag{B.139}$$

f Here, we consider the evolution of the streak mode ($\boldsymbol{k} = \boldsymbol{k}_s = (0,1)$). Previously, we derived the relation $\langle|\hat{u_x}(\boldsymbol{k})|^2\rangle_z = ||{u_x}^{\boldsymbol{k}}(\boldsymbol{x})||^2_{L_2}$ and $||\omega_z^s(\boldsymbol{x})||_{L_2} = \beta||u_x^s(\boldsymbol{x})||_{L_2}$ which holds only in the case of streak mode ($\boldsymbol{k} = \boldsymbol{k}_s = (0,1)$). There relation lean to

$$\langle|\hat{u_x}(\boldsymbol{k}_s)|^2\rangle_z = ||u_x^s(\boldsymbol{x})||^2_{L_2} = 1/\beta^2||\omega_z^s(\boldsymbol{x})||^2_{L_2}. \tag{B.140}$$

Therefore, we have

$$\frac{d}{dt}||\omega_z^s(\boldsymbol{x})||^2_{L_2} = -\beta^2\left\langle \hat{u_x}^*(\boldsymbol{k}_s)\big(\hat{u}_z(\boldsymbol{k}_s)\partial_z\big)\hat{u_x}(\boldsymbol{0}) + \hat{u_x}(\boldsymbol{k}_s)\big(\hat{u}_z^*(\boldsymbol{k}_s)\partial_z\big)\hat{u_x}^*(\boldsymbol{0}) \right\rangle_z$$

$$-\beta^2\left\langle \sum_{\substack{\boldsymbol{k''}+\boldsymbol{k'}=\boldsymbol{k}_s,\\ \boldsymbol{k'}\neq\boldsymbol{0},\boldsymbol{k''}\neq\boldsymbol{0}}} \mathcal{N}(\hat{u_x}(\boldsymbol{k}_s), \hat{u_m}(\boldsymbol{k'}), \hat{u_n}(\boldsymbol{k''})) \right\rangle_z$$

$$-\frac{2\beta^2}{Re}\left\langle \beta^2|\hat{u_x}(\boldsymbol{k}_s)|^2 + |\partial_z\hat{u_x}(\boldsymbol{k}_s)|^2 \right\rangle_z. \tag{B.141}$$

Using the facts that $\partial_z\hat{u_x}(\boldsymbol{0}) = \hat{\omega}_y(\boldsymbol{0}, z)$ and $\hat{\omega}_z(\boldsymbol{k}_s, z) = -i\beta\hat{u}_x(\boldsymbol{k}_s, z)$, the

r.h.s. of the above equation can be written by

$$
\begin{aligned}
&-\beta^2\Big\langle \hat{u_x}^*(\boldsymbol{k}_s)\big(\hat{u}_z(\boldsymbol{k}_s)\partial_z\big)\hat{u_x}(\boldsymbol{0}) + \hat{u_x}(\boldsymbol{k}_s)\big(\hat{u}_z^*(\boldsymbol{k}_s)\partial_z\big)\hat{u_x}^*(\boldsymbol{0})\Big\rangle_z \\
&= i\beta\Big\langle i\beta\hat{u_x}^*(\boldsymbol{k}_s)\hat{u}_z(\boldsymbol{k}_s)\hat{\omega}_y(\boldsymbol{0}) - (-i\beta\hat{u_x}(\boldsymbol{k}_s))\hat{u}_z^*(\boldsymbol{k}_s)\hat{\omega}_y(\boldsymbol{0})\Big\rangle_z \\
&= i\beta\Big\langle \hat{\omega}_z^*(\boldsymbol{k}_s)\hat{u}_z(\boldsymbol{k}_s)\hat{\omega}_y(\boldsymbol{0}) - \hat{\omega}_z(\boldsymbol{k}_s)\hat{u}_z^*(\boldsymbol{k}_s)\hat{\omega}_y(\boldsymbol{0})\Big\rangle_z \\
&= \Big\langle \hat{\omega}_z^*(\boldsymbol{k}_s)\big(i\beta\hat{u}_z(\boldsymbol{k}_s)\big)\hat{\omega}_y(\boldsymbol{0}) + \hat{\omega}_z(\boldsymbol{k}_s)\big(-i\beta\hat{u}_z^*(\boldsymbol{k}_s)\big)\hat{\omega}_y(\boldsymbol{0})\Big\rangle_z \\
&= 2\Big\langle Re\Big[\hat{\omega}_z^*(\boldsymbol{k}_s)\big(i\beta\hat{u}_z(\boldsymbol{k}_s)\big)\hat{\omega}_y(\boldsymbol{0})\Big]\Big\rangle_z . \qquad \text{(B.142)}
\end{aligned}
$$

This term originates from a tilting term $\omega_y\frac{\partial u_z}{\partial y}$ of the z-directional vorticity equation and represents the nonlinear interaction between the mean flows and the streak mode. Using the relation $|\hat{\omega}_z(\boldsymbol{k}_s,z)| = \beta|\hat{u}_x(\boldsymbol{k}_s,z)|$ and $|\partial_z\hat{\omega}_z(\boldsymbol{k}_s,z)| = \beta|\partial_z\hat{u}_x(\boldsymbol{k}_s,z)|$, we obtain

$$
\begin{aligned}
\frac{d}{dt}||\omega_z^s(\boldsymbol{x})||_{L_2}^2 =& 2\Big\langle Re\Big[\hat{\omega}_z^*(\boldsymbol{k}_s)\big(i\beta\hat{u}_z(\boldsymbol{k}_s)\big)\hat{\omega}_y(\boldsymbol{0})\Big]\Big\rangle_z \\
&-\beta^2\Big\langle \sum_{\substack{\boldsymbol{k''}+\boldsymbol{k'}=\boldsymbol{k}_s,\\ \boldsymbol{k'}\neq\boldsymbol{0},\boldsymbol{k''}\neq\boldsymbol{0}}} \mathcal{N}(\hat{u_x}(\boldsymbol{k}_s),\hat{u_m}(\boldsymbol{k'}),\hat{u_n}(\boldsymbol{k''}))\Big\rangle_z \\
&-\frac{2}{Re}\Big\langle \beta^2|\hat{\omega}_z(\boldsymbol{k}_s)|^2 + |\partial_z\hat{\omega}_z(\boldsymbol{k}_s)|^2\Big\rangle_z . \qquad \text{(B.143)}
\end{aligned}
$$

vi

Acknowledgements

I would like to express my appreciation to Prof. Michio Yamada for his great advice on the basis of comprehensive and deep knowledge of fluid mechanics as well as other fields of physics and mathematics. He has given me insightful comments and suggestions not only on specific problems of this study but also on my view of nonlinear science, in particular, turbulence and chaos from fairly broad perspectives.

I would also like to express my gratitude to Prof. Shin-ichi Takehiro, who has provided invaluable comments that made it possible to complete this study. He has offered thoughtful advice on my philosophy about study with warm words of encouragement.

Dr. Yoshitaka Saiki has introduced me to intriguing ideas and research topics of dynamical system theory before entering the graduate school and has provided many opportunities to have great scientific experience. Dr. Miki U. Kobayashi has offered great advice on both academic and personal matters and has given me useful technics of chaos theory, in particular covariant Lyapunov analysis. Fortunately, I have had many chances to have discussion with them, which has stimulated my motivation to study. Dr. Youhei Sasaki has listened well to my poor presentation at weekly seminars and has given helpful comments. Dr. Kiori Obuse has guided me attentively, and especially, she gave me many comments on the introduction of this thesis in constructive ways, which helped make it much easier to read. I am truly thankful for her comments.

I would also like to thank my colleagues at Research Institute for Mathematical Sciences (RIMS), Keiji Kimura, Eiichi Sasaki, and Kenta Ishimoto, for fruitful discussions. My special thanks go to my friends and families, who have always supported me during my university life.

Lastly, I am grateful to the RIMS for providing me a stimulating and brilliant research environment. I will always be proud of having been a member of the RIMS.

Some of the data analyses and the visualizations in this thesis were done

with the ISPACK [66], SPMODEL [67], and the software products of the GFD Dennou Ruby project [68]. The numerical calculations were performed by the computer systems of the Institute for Information Management and Communication (IIMC) of Kyoto University and of the Research Institute for Mathematical Sciences, Kyoto University.

Finally, I would like to thank The Japan Society for the Promotion of Science for a grant (Grant-in-Aid for JSPS Fellows Grant Number 24-3995) which supported the study.

References

[1] Uriel Frisch, “Turbulence: The Legacy of A. N. Kolmogorov”, *Cambridge University Press*, (1996).

[2] 木田 重雄, 柳瀬 真一郎, “乱流力学”, 朝倉書店 (1999).

[3] M. W. Hirsch, S. Smale, and R. L. Devaney, “Differential Equations, Dynamical Systems, and an Introduction to Chaos”, *Academic Press*, (2003).

[4] 国府 寛司, “力学系の基礎 (カオス全書)”, 朝倉書店, (2000).

[5] D. Ruelle, “Chaotic evolution and strange attractors”, *Cambridge University Press*, (1989).

[6] D. Ruelle and F. Takens, “On the nature of turbulence”, *Comm. Math. Phys.*, vol.20, pp.167–192, (1971).

[7] J. P. Eckmann, “Roads to turbulence in dissipative dynamical systems”, *Rev. Modern Phys.*, vol. 53, no. 4, pp. 643–654, (1981).

[8] E. Ott, “Chaos in Dynamical Systems”, *Cambridge University Press*, (2002).

[9] M. Inubushi, M. U. Kobayashi, S. Takehiro, and M. Yamada, “Covariant Lyapunov Analysis of Chaotic Kolmogorov Flows and Time-correlation Function,” *Procedia IUTAM*, vol. 5, pp. 244–248, (2012).

[10] L, D. Landau and E. M. Lifshitz, “Fluid Mechanics”, Pergamon, London, England, (1959).

[11] D. Ruelle, “Chance and Chaos”, *Princeton University Press*, (1993).

[12] J. P. Gollub and H. L. Swinney, “Onset of turbulence in a rotating fluid”, *Phys. Rev. Lett.*, vol.35, No.14, (1975).

[13] T. Bohr, M. H. Jensen, G. Paladin, A. Vulpiani, "Dynamical Systems Approach to Turbulence (Cambridge Nonlinear Science Series)" *Cambridge University Press*, (1998).

[14] Robert L. Devaney "An Introduction to Chaotic Dynamical Systems" *Westview Press; Second Edition edition*, (2003).

[15] J. Banks, J. Brooks, G. Cairns, G. Davis, and P. Stacey, "On Devaney′ s definition of chaos," *Amer. Math. Monthly*, vol. 99, no. 4, pp. 332–334, (1992).

[16] 大野 克嗣, "非線形な世界", 東京大学出版会, (2009).

[17] H. Okamoto, "A study of bifurcation of Kolmogorov flows with an emphasis on the singular limit", *Proc. Int Congress Math.*, III, pp. 523–532, (1998).

[18] 岡本 久, " ナヴィエ- ストークス方程式の数理", 東京大学出版会, (2009).

[19] T. M. Schneider, J. F. Gibson, and J. Burke, "Snakes and Ladders: Localized Solutions of Plane Couette Flow," *Phys. Rev. Lett.*, vol. 104, no. 10, 104501, (2010).

[20] F. Waleffe, "Exact Coherent Structures in Turbulent Shear Flows", Turbulence and Interactions Notes on Numerical Fluid Mechanics and Multidisciplinary Design Volume 105, pp.139–158, (2009).

[21] T. Itano and S. Toh, "The Dynamics of Bursting Process in Wall Turbulence," *Journal of the Physical Society of Japan*, Vol. 70, No. 3, pp. 703–716, (2001).

[22] G. Kawahara, "Laminarization of minimal plane Couette flow: Going beyond the basin of attraction of turbulence, *Phys. Fluids* 17, 041702 (2005).

[23] J. Halcrow, J. F. Gibson, P. Cvitanovic, and D. Viswanath, "Heteroclinic connections in plane Couette flow," *J. Fluid Mech.*, vol. 621, pp. 365–376, (2009).

[24] P. Cvitanović, R. Artuso, R. Mainieri, G. Tanner, and G. Vattay, "Classical and quantum chaos," *Niels Bohr Institute*, Copenhagen, (2001).

[25] G. Kawahara and G. Kida, "Periodic motion embedded in plane Couette turbulence: regeneration cycle and burst", *J. Fluid. Mech.*, vol. 449, pp.291–300, (2001).

[26] L. van Veen and G. Kawahara, "Homoclinic Tangle on the Edge of Shear Turbulence," *Phys. Rev. Lett.*, vol. 107, no. 11, 114501, (2011).

[27] S. Kato and M. Yamada, "Unstable periodic solutions embedded in a shell model turbulence", *Phys. Rev. E*, vol. 68, no. 2, 025302(4), (2003).

[28] Y. Saiki and M. Yamada, "Time-averaged properties of unstable periodic orbits and chaotic orbits in ordinary differential equation systems", *Phys. Rev. E* 79, 015201(4), (2009).

[29] G. Kawahara, "The Significance of Simple Invariant Solutions in Turbulent Flows", *Annu. Rev. Fluid Mech.*, 44, pp.203–225, (2012).

[30] I. Shimada and T. Nagashima, "A Numerical Approach to Ergodic Problem of Dissipative Dynamical Systems", *Prog. Theor. Phys.* Vol. 61 No. 6, pp. 1605–1616, (1979).

[31] W. Ott and J. Yorke, "When Lyapunov exponents fail to exist", *Phys. Rev. E*, 78, 5, 056203, (2008).

[32] M. Yamada and K. Ohkitani, "Asymptotic formulas for the Lyapunov spectrum of fully developed shell model turbulence", *Phys. Rev. E* 57, 6257 (1998).

[33] A. Karimi and M. R. Paul, "Quantifying spatiotemporal chaos in Rayleigh-Bénard convection," *Phys. Rev. E*, vol. 85, no. 4, 046201, (2012).

[34] L. Keefe, P. Moin, and J. Kim, "The dimension of attractors underlying periodic turbulent Poiseuille flow", *J . Fluid Mech.*, vol. 242, pp. 1–29 (1992).

[35] N. V. Nikitin, "Disturbance Growth Rate in Turbulent Wall Flows", *Fluid Dynamics*, Vol. 44, No. 5, pp.652–657, (2009).

[36] F. Ginelli, P. Poggi, A. Turchi, H. Chaté, R. Livi, and A. Politi, "Characterizing Dynamics with Covariant Lyapunov Vectors", *Phys. Rev. Lett.* 99, 130601(4) (2007).

[37] C. L. Wolfe and R. M. Samelson, "An efficient method for recovering Lyapunov vectors from singular vectors" *Tellus*, 59A, pp. 355–366, (2007).

[38] I. G. Szendro, D. Paźo, M. A. Rodriguez, and J. M. López, "Spatiotemporal structure of Lyapunov vectors in chaotic coupled-map lattices" *Phys. Rev. E*, 76, 025202(R) (2007).

[39] P. V. Kuptsov, U. Parlitz, "Theory and Computation of Covariant Lyapunov Vectors", *Journal of Nonlinear Science*, Vol. 22, Issue 5, pp 727–762 (2012).

[40] H-L Yang and G. Radons, "Lyapunov modes in extended systems", *Phil. Trans. R. Soc. A*, 367, pp.3197–3212 (2009).

[41] D. Pazó, I. G. Szendro, J. M. López, and M. A. Rodriguez "Structure of characteristic Lyapunov vectors in spatiotemporal chaos" *Phys. Rev. E*, 78, 016209 (2008).

[42] H-L Yang, K. A. Takeuchi, F. Ginelli, H. Chaté, and G. Radons, "Hyperbolicity and the Effective Dimension of Spatially Extended Dissipative Systems" *Phys. Rev. Lett.* 102, 074102 (2009).

[43] J. C. Robinson, "Infinite-Dimensional Dynamical Systems: An Introduction to Dissipative Parabolic PDEs and the Theory of Global Attractors", *Cambridge University Press* (2001).

[44] H-L Yang and G. Radons, "Geometry of Inertial Manifolds Probed via a Lyapunov Projection Method" *Phys. Rev. Lett.* 108, 154101 (2012).

[45] C. Robinson, "Dynamical Systems: Stability, Symbolic Dynamics, and Chaos, 2nd ed.", *CRC Press* (1998).

[46] B. Krauskopf, H. M. Osinga, E. J. Doedel, M. E. Henderson, J. Guckenheimer, M. Dellnitz, and O. Junge, "A Survey of Methods for Computing (Un)stable Manifolds of Vector Fields" *Int. J. Bifurc. Chaos*,15, 763 (2005).

[47] L. van Veen, G. Kawahara, and A. Matsumura, "On Matrix-Free Computation of 2D Unstable Manifolds", *SIAM Journal on Scientific Computing* 33, 25 (2011).

[48] Y. Saiki and M. U. Kobayashi, "Numerical identification of nonhyperbolicity of the Lorenz system through Lyapunov vectors", *JSIAM Letters*, 2, pp.107–110 (2010).

[49] Y. Saiki and M. U. Kobayashi, "Manifold Structures of Unstable Periodic Orbits and the Appearance of Periodic Windows in the Lorenz system"

[50] P. Kuptsov and S. Kuznetsov, "Violation of hyperbolicity in a diffusive medium with local hyperbolic attractor" *Phys. Rev. E* 80, 016205 (2009).

[51] R. Artuso and C. Manchein, "Instability statistics and mixing rates", *Phys. Rev. E* 80, 036210 (2009).

[52] M. Inubushi, M. U. Kobayashi, S. Takehiro, and M. Yamada "Covariant Lyapunov analysis of chaotic Kolmogorov flows" *Phys. Rev. E* 85, 016331 (2012).

[53] Z. Arai, "On Hyperbolic Plateaus of the Hénon Map", *Experimental Mathematics*, Vol. 16, Issue 2, (2007).

[54] N. Platt, L. Sirovich, and N. Fitzmaurice, "An investigation of chaotic Kolmogorov flows", *Phys. Fluids A* 3, 681 (1990).

[55] V. I. Iudovich, "Example of the generation of a secondary stationary or periodic flow when there is loss of stability of the laminar flow of a viscous incompressible fluid", *J. Appl. Math. Mech.* 29, pp.527–544, (1965).

[56] D. A. Egolf, I. V. Melnikov, W. Pesch, and R. E. Ecke, "Mechanisms of extensive spatiotemporal chaos in Rayleigh-Bénard convection", *Nature*, vol. 404, no. 6779, pp. 733–736, (2000).

[57] M.U.Kobayashi and M. Yamada, "Temporal intermittency in a shell model turbulence in terms of covariant Lyapunov vectors", *Journal of Physics A: Mathematical and Theoretical* (submitted).

[58] J. Jimenez and P. Moin, "The minimal flow unit in near-wall turbulence.," *J. Fluid Mech.*, vol. 225, no. 213, (1991).

[59] J. M. Hamilton, J. Kim, and F. Waleffe, "Regeneration mechanisms of near-wall turbulence structures", *J. Fluid Mech.*, vol. 287, pp. 317–348 (1995).

[60] R. L. Panton, "Overview of the self-sustaining mechanisms of wall turbulence," *Progress in Aerospace Sciences*, vol. 37, no. 4, pp. 341–383 (2001).

[61] T. Duriez, J.-L. Aider, and J. Wesfreid, "Self-Sustaining Process through Streak Generation in a Flat-Plate Boundary Layer," *Phys. Rev. Lett.*, vol. 103, no. 14, 44502, (2009).

[62] F. Waleffe, "On a self-sustaining process in shear flows", *Phys. Fluids* 9, 883 (1997).

[63] L. Kim and J. Moehlis, "Characterizing the edge of chaos for a shear flow model," *Phys. Rev. E*, vol. 78, no. 3, 036315 (2008).

[64] R. M. Clever and F. H. Busse, " Three-dimensional convection in a horizontal fluid layer subjected to a constant shear" , *J. Fluid Mech.*, vol. 234, pp. 511–527, (1992).

[65] J. Philip and P. Manneville, "From temporal to spatiotemporal dynamics in transitional plane Couette flow", *Phys. Rev. E*, 83, 036308 (2011).

[66] K. Ishioka, ispack-0.95, http://www.gfd-dennou.org/arch/ispack/, GFD Dennou Club.

[67] S. Takehiro, M. Odaka, K. Ishioka, M. Ishiwatari, and Y. Hayashi, SPMODEL : A series of Hierarchical Spectral Models for Geophysical Fluid Dynamics, Nagare Multimedia, (2006). Available on-line at : http://www.nagare.or.jp/mm/2006/spmodel/

[68] http://www.gfd-dennou.org/library/ruby/

[69] G. Kawahara, "Theoretical interpretation of coherent structures in near-wall turbulence", *Fluid Dyn. Res.* 41, 064001 (2009).

[70] D. Viswanath, "Recurrent motions within plane Couette turbulence", *J. Fluid Mech.*, vol.580, pp.339–358 (2007).

[71] W. Schoppa and F. Hussain, "Coherent structure generation in near-wall turbulence", *J. Fluid Mech.*. vol.453, pp.57–108 (2002).

[72] G. Kawahara, J. Jimenez, M. Uhlmann, and A. Pinelli, "Linear instability of a corrugated vortex sheet - a model for streak instability" *J. Fluid Mech.*, vol.483, pp.315–342 (2003).

[73] J. F. Gibson, J. Halcrow, and P. Cvitanovic: Visualizing the geometry of state space in plane Couette flow, *J. Fluid Mech.* vol. 611, pp.107–130 (2008).

[74] Y. Saiki and M. Yamada, "On the relations between statistical values along unstable periodic orbits in differential equation systems", *RIMS Kokyuroku*, 1768, pp.143–149 (2011).

[75] J. Kim, P. Moin, and R. Moser: Turbulence statistics in fully developed channel flow at low Reynolds number, J. Fluid Mech., vol. 177, pp.133–166 (1987).

[76] 石岡圭一, "スペクトル法による数値計算入門", 東京大学出版 (2004).

[77] J. Jiménez, G. Kawahara, M. P. Simens, M. Nagata, and M. Shiba, "Characterization of near-wall turbulence in terms of equilibrium and ' bursting ' solutions", *Phys. Fluids*, vol. 17, no. 1, 015105, (2005).